Numerical Simulations of Strongly Correlated Electron Systems on Bipartite and on Frustrated Lattices

Inauguraldissertation
der Philosophisch-naturwissenschaftlichen Fakultät
der Universität Bern

vorgelegt von

Matthias Nyfeler

von Gondiswil BE

Leiter der Arbeit: Prof. Dr. U.-J. Wiese
Institut für theoretische Physik
Universität Bern

Numerical Simulations of Strongly Correlated Electron Systems on Bipartite and on Frustrated Lattices

Inauguraldissertation
der Philosophisch-naturwissenschaftlichen Fakultät
der Universität Bern

vorgelegt von

Matthias Nyfeler

von Gondiswil BE

Leiter der Arbeit: Prof. Dr. U.-J. Wiese
Institut für theoretische Physik
Universität Bern

Von der Philosophisch-naturwissenschaftlichen Fakultät angenommen.

Der Dekan:

Bern, den 6. Oktober 2009

Prof. Dr. U. Feller

Abstract

In this thesis, the antiferromagnetic Heisenberg model and some of its extensions are studied. We are interested in the spontaneous symmetry breaking of the $SU(2)$ spin symmetry and its physical consequences. In our numerical work we calculate the low-energy effective field theory parameters and compare them to other numerical and analytical work. In the extended models we are interested in the breakdown of antiferromagnetism, i.e. where the $SU(2)$ spin symmetry is restored, and its implications. We investigate the nature of these phase transitions and also other types of order such as the valence bond solid (VBS) order.

In the second part of this thesis we address the sign problem of frustrated antiferromagnets and present a new method which substantially improves the efficiency of these calculations. We can perform simulations on lattices with more than 1000 spins at moderate temperature, which is something previously impossible on systems with a sign problem. Also we extend this method to the calculation of the real-time evolution of quantum spin systems.

In the last part we measure the two-point correlation function of a single hole doped into an antiferromagnet and calculate its dispersion relation for different lattice geometries. Depending on the chosen couplings, different dispersion relations emerge for the same model which can be described with different low-energy effective field theories.

Truth is ever to be found in simplicity, and not in the multiplicity and confusion of things.

Isaac Newton

I took physics because it was interesting, and it excited me — not to buy me a job

---

MacGyver

Contents

Introduction **1**

1 The Quantum Heisenberg Model **5**
- 1.1 Bipartite Lattice Geometries . . . 5
- 1.2 The $SU(2)_s$ Spin Symmetry . . . 6
- 1.3 Observables . . . 7
- 1.4 Spontaneous Symmetry Breaking . . . 7

2 Cluster Algorithms for the Heisenberg Model **9**
- 2.1 Discrete-time Cluster Algorithm . . . 9
  - 2.1.1 The Monte Carlo Method . . . 11
  - 2.1.2 Cluster Updates . . . 13
  - 2.1.3 Detailed Balance, Ergodicity, and the Reference Configuration . . . 14
  - 2.1.4 Efficiency . . . 14
  - 2.1.5 Measuring Susceptibilities . . . 14
  - 2.1.6 Continuous-time Limit . . . 15
- 2.2 Continuous-time Cluster Algorithm . . . 15
  - 2.2.1 Measuring Susceptibilities . . . 16
- 2.3 Stochastic Series Expansion . . . 17
  - 2.3.1 Measuring Susceptibilities . . . 18

3 Low-Energy Magnon Effective Field Theory **21**
- 3.1 Leading Order Action . . . 21
- 3.2 Calculations at Finite Volume and Temperature . . . 22
- 3.3 Low-Energy Constants for the Square Lattice . . . 24

4 Effective Field Theory and Simulation of Heisenberg Model on the Honeycomb Lattice **25**
- 4.1 Simulation Set-up on a Honeycomb Lattice . . . 25
- 4.2 Magnon Effective Theory . . . 25
- 4.3 Determination of the Low-Energy Parameters of the Magnon Effective Theory 27
  - 4.3.1 Effective Theory Predictions in the Cylindrical Regime . . . 28
  - 4.3.2 Outlook on the t-J Model for Fermion Doping . . . 29

5 The Heisenberg Model on a Square Lattice with Spatially Anisotropic Couplings 31
5.1 Spatially Anisotropic Heisenberg Model 31
5.2 Low-Energy Effective Theory for Magnons 32
5.3 Determination of the Low-Energy Parameters 32
5.4 Restoration of the $SU(2)_s$ Spin Symmetry 35
5.5 Usage of the ALPS Library 36

6 The Heisenberg Antiferromagnet with Additional Four-spin Interaction 37
6.1 Extended Heisenberg Model 37
6.2 Deconfined Quantum Criticality 38
6.3 Weakening of Antiferromagnetism 38
6.3.1 Determination of the Low-Energy Parameters 38
6.4 Phase Transition between Antiferromagnetism and VBS order 42
6.4.1 Finite-Size Effects of $\langle W_i^2 \rangle$ near the Transition 42
6.4.2 Application of the Flowgram Method 44
6.5 The Valence Bond Solid Phase 48
6.6 Probability Distribution of the VBS Order Parameter 49
6.7 Antiferromagnetic Correlations in the VBS phase 50

I Numerical Simulations of the Quantum Heisenberg Model on Frustrated Lattices 51

7 Candidate Ground States on Frustrated Lattices 53
7.1 Antiferromagnet on a Square Lattice 53
7.2 Candidate Ground State on a Triangular Lattice 53
7.2.1 Coplanar Order Parameter 54
7.3 Frustrated Square Lattice 55
7.4 Candidate Ground State on a Kagomé Lattice 55

8 Nested Cluster Algorithm 59
8.1 The Sign Problem 59
8.1.1 NP-Completeness 60
8.2 Meron-Cluster Algorithm 61
8.2.1 Fermionic Sign Problem 62
8.2.2 Sign Problem for Frustrated Lattice Geometries 62
8.3 Nested Cluster Algorithm 63
8.3.1 Making the Cluster Algorithm Ergodic 64
8.3.2 Factorisation of the Sign 65
8.3.3 Improved Measurement of the Sign and the Staggered Susceptibility 66
8.3.4 Nested Cluster Algorithm in the SSE Representation 67
8.3.5 Additional Energy Shift 67

8.4 Results 68
8.5 Fine-Tuning of the Nested Cluster-Algorithm 70

9 Nested Cluster Algorithm for Real-Time Evolution of a Quantum Spin System 75
9.1 Factorisation of the Phase 76
9.2 Internal Cluster Updates 77
9.3 Results for Real-Time Evolution with a Fixed Initial State 77
9.4 Results for the Real-Time Evolution Coupled to a Heat-Bath 79

II Simulations of Single Electrons and Holes in the t-J Model 83

10 The t-t'-J Model on the Square Lattice and its Low-Energy Effective Field Theories 85
10.1 Microscopic Formulation 85
10.2 The Location of the Pockets in the t-t'-J Model 86
10.3 Magnon Field Transformation Rules 87
10.4 Low-Energy Fermion Field Transformation Rules 88
    10.4.1 Fermion Fields for Hole-doped Systems 88
    10.4.2 Low-Energy Fermion Fields for Electron-Doped Systems 89
    10.4.3 Transformation Rules for Fermion Fields Located at $(0,0)$ and $(\frac{\pi}{a},\frac{\pi}{a})$ 90
10.5 Low-Energy Effective Lagrangian 91
    10.5.1 Hole-Doped Antiferromagnet 91
    10.5.2 Electron-Doped Antiferromagnet 92
    10.5.3 Charge Carriers at $(0,0)$ and $(\frac{\pi}{a},\frac{\pi}{a})$ 92
10.6 The Two-Point Correlation Function 92
10.7 Fitting Energies in Momentum-Space 93
10.8 Fitting Mass Parameters 93

11 The t-J Model on the Honeycomb Lattice and its Low-Energy Effective Field Theory 97
11.1 Brillouin Zone of a Honeycomb Lattice 97
11.2 Fermion Dispersion Relation for the t-J Model on the Honeycomb Lattice . 97
11.3 Effective Field Theory for Holes and Magnons 100
    11.3.1 Magnon- and Hole-Field Symmetry-Transformations on a Honeycomb Lattice 100
    11.3.2 Effective Lagrangian 102

Conclusion and Outlook 107

Acknowledgement 111

A Loop-Cluster Algorithm for the J-Q-Model 113
A.1 12-Step Suzuki-Trotter Decomposition 113
A.2 4-Step Suzuki-Trotter Decomposition 114

B Antiferromagnet on a Triangular Lattice in the Classical Ground State Basis 117
B.1 Quantisation in a Coplanar Basis 117
B.2 How to Deal with the Sign Problem 118
B.3 Cluster Algorithm with the Spins Integrating out 120

Bibliography 121

Curriculum vitæ 129

Introduction

High-Temperature Superconductivity

Since the discovery of high-temperature superconductivity (high T_c) in 1986 by G. Bednorz and K. Müller [1], there has been a lot of research in the condensed matter physics of high T_c materials. Ceramic materials which are electric insulators turn upon doping of a few percent of rare earth materials into conductors and even become superconducting at much higher temperature than ordinary superconductors whose phase transitions are around 4-16K. As of 2006, the highest-temperature superconductor at normal pressure is $\mathrm{Hg_{12}Tl_3Ba_{30}Ca_{30}Cu_{45}O_{125}}$ with T_c=138 K [2].

Despite extensive research, no fundamental theory has yet been found which accurately describes the mechanism that causes superconductivity in such materials. For ordinary low-temperature superconductors the Barden-Cooper-Schrieffer (BCS) theory describes superconductivity very accurately by the Cooper-pair formation of two electrons bound by phonon exchange [3]. However, this theory cannot explain high T_c phenomena. Hence, this is an active topic of current research which probably will continue to puzzle and fascinate researchers in the future.

There are now many known high T_c materials with various geometrical lattice structures. Many of them are quasi-two-dimensional, i.e. the couplings in a plane are much stronger than the coupling between different planes. For the investigation of the low-energy physics of these materials it is thus sufficient to consider two-dimensional models. There are many different quasi two-dimensional high T_c materials. Well-known materials with a square lattice structure are the cuprates such as $\mathrm{La_{2-x}Sr_xCuO_4}$ and $\mathrm{YBa_2Cu_3O_{7-x}}$ (YBCO).

Another superconducting material is $\mathrm{Na_xCoO_2{\cdot}yH_2O}$ with the underlying spin $\frac{1}{2}$ cobalt sites that are on a triangular lattice. The spin- and charge-ordering tendencies observed in [4–6] may suggest that the unhydrated parent compound $\mathrm{Na_xCoO_2}$ can be described by the t-J model on a half-filled honeycomb lattice. Hence, the physics of these material depends on the geometrical lattice structure and it is interesting to investigate models such as the spin $\frac{1}{2}$ Heisenberg antiferromagnet or the t-J model on these different geometries [7, 8].

The undoped precursors of high T_c materials are antiferromagnetically ordered. Because first principles calculations of doped materials are extremely hard, it is interesting to first investigate these precursors and the breakdown of the antiferromagnetism. Also in the superconducting phase, antiferromagnetism is ultimately destroyed via doping [8, 9].

These precursors can be described by a low-energy effective field theory in analogy to chiral perturbation theory for the pseudo-Goldstone pions in Quantum Chromodynamics (QCD) [10–15]. Such effective field theories for the undoped precursors of high T_c materials, two-dimensional antiferromagnets, have been developed on the different lattices both for hole- and for electron-doped cases [16–26]. In QCD, the physics at low energies is dominated by the spontaneously broken $SU(2)_L \otimes SU(2)_R$ chiral flavour symmetry for massless up and down quarks, which breaks to the unbroken subgroup $SU(2)_{L=R}$. As a result, QCD displays three Goldstone bosons π^+, π^-, and π^0. In an antiferromagnet on the square or honeycomb lattice at zero temperature, the global $SU(2)_s$ spin rotation symmetry spontaneously breaks down to the unbroken subgroup $U(1)_s$. This is because the expectation value of the staggered magnetisation becomes non-zero and spontaneously chooses a direction. As a result, two massless Goldstone bosons, the spinwaves or magnons emerge. The parameters of the low-energy effective field theory describing the magnon physics and the propagation of doped holes and electrons are not determined by the effective theory itself, but have to be determined externally. This can be done by performing first principles microscopic calculations, such as Monte Carlo simulations, which will be presented in this thesis to high accuracy.

As discussed further below, we cannot arbitrarily dope fermions in computer simulations due to the sign problem. However, we can simulate the propagation of a single fermion in an antiferromagnet. By calculating the correlation function of a single fermion we can extract the single-fermion dispersion relation. Interestingly, depending on the choice of the coupling and hopping constants in the microscopic model, three qualitatively distinct dispersion relations were measured. Due to the different locations of the minima, the low-energy physics governed by excitations around these minima is also distinctively different which leads to different low-energy effective field theories.

Many-Body Problems

By investigating microscopic models of condensed matter systems, we deal with a many-body problem. Even the very simplest of such models can produce rich macroscopic phenomena, once a large number of particles is involved. This is a huge theoretical challenge, because macroscopic materials always contain a gigantic number of particles and reliable first-principles microscopic calculations should at least involve a sufficiently large number of particles in order to extract the long-range physics [27].

A method that has proved very successful to solve many-body problems is the Monte Carlo method. Using Monte Carlo simulations, thermal averages of bosonic systems can be computed with a numerical effort that scales polynomially with the number of particles involved. Thus it is possible to directly compute macroscopic observables in microscopic models.

Still the efficiency of concrete Monte Carlo algorithms is an important subject, because only by using specific methods one can go to sufficiently large lattices and extrapolate reliably to infinite size boxes. This can be seen in the example of the Ising model, where today's most efficient algorithms implemented on computers thirty years ago would be faster than the algorithms of thirty years ago implemented on today's computers. This is quite remarkable, noting that the performance speed of computers has grown exponentially over time. According to Moore's law the number of transistors that can be placed inexpensively on an integrated circuit has increased exponentially, doubling approximately every two years [28]. The exponential growth of computer capacity is thus by far outgrown by the improvement gained by new algorithms. Hence, it is important research to find better algorithms which provide tools to investigate the physics of strongly correlated materials.

Monte Carlo simulations are based on the idea of importance sampling where a partition function is not analytically calculated, but rather configurations are generated with a probability proportional to their Boltzmann weight. Thus the important configurations are sampled more often. Using that idea, a set of configurations is sampled where every new configuration is generated out of the previous one leading to a so-called Markov chain.

Early simulations were performed with Metropolis-type algorithms which suffer from critical slowing down [29]. Metropolis algorithms usually perform only local updates and thus the autocorrelation times tend to be very large. Improved Metropolis algorithms such as hybrid Monte Carlo are still widely used in the particle physics community where for most problems no cluster-type algorithms could be constructed yet. A major breakthrough was achieved by Swendsen and Wang in 1987 with the first cluster algorithm for the Ising and Potts model which performs non-local updates [30]. This method was generalised by Wolff to classical $O(N)$ models [31]. Cluster algorithms for quantum systems were first developed in [32] using a block-spin scheme efficient only in one dimension and then for vertex models using the loop-algorithm in [33]. The first application to quantum spins was reported in [34].

As mentioned above, Monte Carlo simulations can be used to perform simulations of antiferromagnets in order to calculate the low-energy effective parameters. Also it is very interesting to use these methods to study phase transitions. In this thesis we investigate a Heisenberg antiferromagnet with spatially anisotropic couplings that lead to dimensional crossover from a two-dimensional Heisenberg antiferromagnet to decoupled spin chains. Such phenomena are very interesting because the restoration of the spin symmetry and the dimensional crossover happen at the same point. Also we consider a Heisenberg antiferromagnet with an additional four-spin interaction, the J-Q model first proposed in [35], where for sufficiently large Q the spin symmetry is restored. However, the lattice symmetry is spontaneously broken and a valence bond solid (VBS) phase emerges. In contradiction to the Ginzburg-Landau-Wilson paradigm some experts expect an exotic second order phase transition, a deconfined quantum critical point, as described in [36]. We thus investigate this transition using quantum Monte Carlo and come to the conclusion that it is weakly first order.

The above discussed simulations were all done on bipartite lattices. On lattice geometries such as the square and the honeycomb lattice, the ground state of the classical Heisenberg antiferromagnet is the classical Néel state. In the quantum case the spins also show long-range antiferromagnetism. However, on non-bipartite lattices the advantage of Monte Carlo is lost because a sign problem arises. The sign problem is a computational problem arising in a path integral formulation of quantum systems. Caused by geometrical frustration of the antiferromagnetism or the interchange of fermions, contributions to the path integral can be negative and can thus no longer be interpreted as probabilities, which is the principle Monte Carlo is based upon. This can be dealt with by treating the sign as part of the observables. However, the statistical errors then grow exponentially with the number of particles and thus the advantage of Monte Carlo is lost.

On lattices such as the triangular or the kagomé lattice, antiferromagnets are geometrically frustrated. For a classical Heisenberg antiferromagnet on the triangular lattice, the ground state has coplanar order. However, this is not clear yet for the quantum Heisenberg antiferromagnet, although coplanar order is also expected. On the kagomé lattice the case is more difficult. The classical ground state is highly degenerate and for the quantum case some experts expect a quantum spin liquid [37, 38]. A spin liquid is a state where there is no symmetry breaking and thus no ordering even at zero temperature.

For certain models the sign problem could be solved by cancelling all negative with certain positive contributions to the partition function using the meron-cluster algorithm [39]. However, this cannot be achieved in general. Since many of the interesting problems in condensed matter physics, e.g. systems with fermions, suffer from the sign problem, progress in that direction is indeed needed if one wants to perform first principles microscopic calculations in order to get further fundamental insight into the models used to describe these condensed matter systems.

In this work we show how to improve the measurement of the sign for frustrated quantum antiferromagnets. With the nested cluster algorithm we have performed calculations of very large systems which were previously impossible. However, the method is restricted to moderate temperatures [40]. Improving such methods in order to reach low temperatures is the subject of on-going research.

Interestingly enough that method can also be used to simulate the real-time evolution of a quantum spin system, but unfortunately it has not been very efficient.

Thesis Layout

This thesis is organised as follows. In part I we investigate certain variants of the Heisenberg model on bipartite lattices, calculate their low-energy effective parameters and study restoration of the spin symmetry for some cases.

In part II we present our new method to deal with frustrated antiferromagnets and the results we could achieve as well as the extension of this method to the real-time evolution of quantum systems.

Finally, in part III we discuss the calculation of the single-hole dispersion relation of antiferromagnets on the square and on the honeycomb lattice.

Chapter 1

The Quantum Heisenberg Model

The quantum Heisenberg model is a microscopic model for magnetism in spin systems. It describes particles of a certain spin localised on a lattice. The model is defined by the Hamiltonian

$$H = J \sum_{\langle xy \rangle} \vec{S}_x \cdot \vec{S}_y, \tag{1.1}$$

where J is the exchange coupling constant and $\langle xy \rangle$ are neighbouring lattice sites. The resulting partition function takes the form

$$Z = \mathrm{Tr} \exp(-\beta H), \tag{1.2}$$

where β denotes the inverse temperature. Depending on the sign of J the model is either ferromagnetic when $J < 0$ or antiferromagnetic when $J > 0$. In the following we will only consider the antiferromagnetic spin $\frac{1}{2}$ Heisenberg model in two dimensions, and in part I of this thesis only on bipartite lattice geometries.

1.1 Bipartite Lattice Geometries

On a bipartite lattice every site can be attributed to one of two sublattices A and B, where every site on A has only neighbours on B and vice versa, as shown in figure 1.1. Interesting examples are the spin chain, the square lattice, or the honeycomb lattice. On some of these lattices we will investigate the physics of the Heisenberg model in the following chapters.

The classical ground state of an antiferromagnet on a bipartite lattice is the classical Néel state. The classical Néel state is realised when all spins on sublattice A point in one direction and all spins on sublattice B point exactly in the opposite direction. For example on the antiferromagnetic Ising model all spins on sublattice A take the value $+1$ and all spins on the sublattice B take the value -1 or vice versa. In the case of the classical Heisenberg antiferromagnet the spins on the sublattice A point in the direction $\vec{e}$ and all spins on the sublattice B point in the direction $-\vec{e}$.

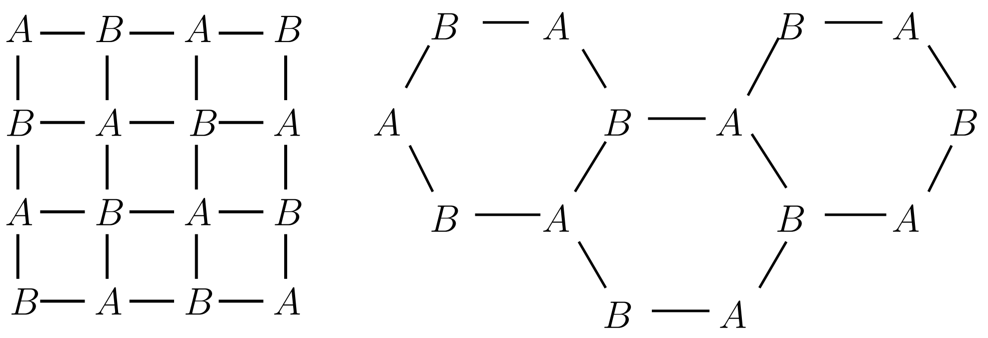

Figure 1.1: *Two examples of two-dimensional bipartite lattices with sublattices A and B: a) the square lattice and b) the honeycomb lattice.*

1.2 The $SU(2)_s$ Spin Symmetry

The spin operators

$$\vec{S}_x = \frac{1}{2}\left(\sigma_x^1, \sigma_x^2, \sigma_x^3\right), \tag{1.3}$$

where σ_x^i are the Pauli matrices, obey the standard commutation relations

$$[S_x^i, S_y^j] = i\delta_{xy}\varepsilon_{ijk}S_x^k. \tag{1.4}$$

It is interesting to note that the Hamiltonian is invariant under global $SU(2)_s$ spin rotations, because the scalar product $\vec{S}_x \cdot \vec{S}_y$ does not change under $SU(2)_s$ rotations. Introducing the operator of the total spin

$$\vec{S} = \sum_x \vec{S}_x, \tag{1.5}$$

this symmetry follows from

$$[H, \vec{S}] = 0. \tag{1.6}$$

In two dimensions at zero temperature, this global symmetry is spontaneously broken on the square and the honeycomb lattice. This cannot be seen directly by inspecting the Hamiltonian, because spontaneous symmetry breaking is a complicated dynamical effect. The relevant order parameter is the staggered magnetisation

$$\vec{M}_s = \sum_x \vec{S}_x(-1)^x, \quad (-1)^x = 1 \text{ for } x \in A, \quad (-1)^x = -1 \text{ for } x \in B, \tag{1.7}$$

which in the infinite volume limit takes a non-zero expectation value. In a finite volume V and at finite inverse temperature β, spontaneous symmetry breaking manifests itself by the staggered susceptibility χ_s, which grows linearly with βV.

1.3 Observables

Thermal expectation values of observables are formally computed as

$$\langle \mathcal{O} \rangle = \frac{1}{Z} \mathrm{Tr} \left[\mathcal{O} \exp(-\beta H) \right]. \tag{1.8}$$

As we are going to investigate the quantum Heisenberg antiferromagnet on bipartite lattices, relevant observables are the staggered magnetisation as defined in eq. (1.7), and the staggered susceptibility

$$\chi_s = \frac{1}{V} \int_0^\beta dt \; \langle M_s^3(0) M_s^3(t) \rangle = \frac{1}{V} \int_0^\beta dt \; \frac{1}{Z} \mathrm{Tr}[M_s^3(0) M_s^3(t) \exp(-\beta H)] \tag{1.9}$$

with V being the spatial volume. Another relevant quantity is the uniform susceptibility

$$\chi_u = \frac{1}{V} \int_0^\beta dt \; \langle M^3(0) M^3(t) \rangle = \frac{1}{V} \int_0^\beta dt \; \frac{1}{Z} \mathrm{Tr}[M^3(0) M^3(t) \exp(-\beta H)]. \tag{1.10}$$

Here $M^3 = \sum_x S_x^3$ is the uniform magnetisation. Both χ_s and χ_u can be efficiently measured using the algorithms introduced in the next chapter.

1.4 Spontaneous Symmetry Breaking

The two-dimensional quantum Heisenberg antiferromagnet on the square or honeycomb lattice undergoes a second order phase transition at zero temperature in the infinite volume limit. This can be observed by the order parameter, the staggered magnetisation $\vec{M}_s$, which takes non-zero expectation value. This is a consequence of the Merwin-Wagner theorem, stating that there is no spontaneous symmetry breaking of continuous symmetries at finite temperature in systems with sufficiently short-range interactions in two dimensions [41]. However, in a finite volume at non-zero temperature, which is the standard situation in a computer simulation, the $SU(2)_s$ spin symmetry is not broken. This can be observed by at the staggered magnetisation taking an expectation value equals to zero.

However, at low temperature one already observes very long (but not infinite) antiferromagnetic order. The range of the correlations is measured by the correlation function

$$\langle S_x^3 S_y^3 \rangle \propto \exp\left(-\frac{|x-y|}{\xi} \right), \tag{1.11}$$

whose exponential decay is characterised by the correlation length ξ. The correlation length

$$\xi = \exp(2\pi\beta\rho_s) \tag{1.12}$$

diverges in the $\beta \to \infty$ limit. The correlation length ξ is not to be confused with the length scale ξ in the low-energy effective field theory introduced in chapter 3.

The consequence of the spontaneous symmetry breaking of the $SU(2)_s$ spin symmetry to its subgroup $U(1)_s$, at zero temperature in the infinite volume limit, are two massless Goldstone modes known as spinwaves or magnons. This leads to interesting low-energy physics which will be discussed in more detail in chapter 3.

Chapter 2

Cluster Algorithms for the Heisenberg Model

In this chapters we will introduce the main numerical methods we will be using in the first part of this thesis. Namely the loop-cluster algorithm to simulate microscopic quantum spin models, i.e. in particular the spin $\frac{1}{2}$ Heisenberg antiferromagnet. For further reading we refer to [42, 43].

2.1 Discrete-time Cluster Algorithm

In order to simulate the quantum Heisenberg model one can rewrite the partition function as a sum over all states $|n\rangle$ in a chosen basis, usually in the basis of spins quantised in the z-direction.

Following Suzuki-Trotter, in discrete time one decomposes the Hamiltonian H into different parts $H_1, \ldots, H_N$ where the terms contributing to of H_i commute with each other [44]. In one dimension this implies the following splitting into two parts,

$$H = H_1 + H_2, \qquad H_1 = J \sum_{x\in(2m)} \vec{S}_x \cdot \vec{S}_{x+\hat{1}}, \qquad H_2 = J \sum_{x\in(2m+1)} \vec{S}_x \cdot \vec{S}_{x+\hat{1}}, \tag{2.1}$$

while in two dimensions on a square lattice four parts are needed, e.g.

$$\begin{aligned} H_1 &= \sum_{x\in(2m,n)} h_{x,1}, & H_2 &= \sum_{x\in(m,2n)} h_{x,2}, \\ H_3 &= \sum_{x\in(2m+1,n)} h_{x,1}, & H_4 &= \sum_{x\in(m,2n+1)} h_{x,2}, \end{aligned} \tag{2.2}$$

where $m,\ n \in \mathbb{N}$ and $h_{x,\mu} = J\vec{S}_x \cdot \vec{S}_{x+\hat{\mu}}$. For other lattice geometries, other similar decompositions can be chosen.

Using a decomposition $H = \sum_k H_k$, the partition function then takes the form

$$Z = \mathrm{Tr}\exp(-\beta \sum_k H_k) = \sum_n \langle n| \exp(-\beta \sum_k H_k) |n\rangle. \tag{2.3}$$

We rewrite the partition function, by introducing complete sets of states $\sum_n |n\rangle\langle n| = \mathbb{1}$ and obtain a path integral

$$Z = \sum_{n_1,\ldots,n_{kM}} \langle n_1| \exp(-\varepsilon H_1)|n_2\rangle \ldots \langle n_k| \exp(-\varepsilon H_k)|n_{k+1}\rangle\langle n_{k+1}| \ldots \\ \ldots |n_{kM-1}\rangle\langle n_{kM}| \exp(-\varepsilon H_k)|n_1\rangle + \mathcal{O}(\varepsilon^2), \qquad (2.4)$$

where $\varepsilon = \beta/M$. The inverse temperature β can be interpreted as the extent of an additional Euclidean time dimension. We thus obtain a $d+1$ dimensional space-time lattice. The Euclidean time direction consists of kM discrete steps. Using this technique one should keep in mind, that one has to perform the following calculations at different ε in order to take the $\varepsilon \to 0$ limit. The spin chain with the decomposition described in eq. (2.1), is shown in figure 2.1, where the interaction is located on the shaded plaquettes.

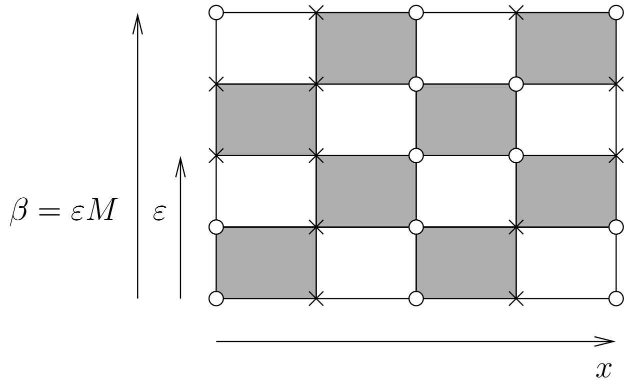

Figure 2.1: *Suzuki-Trotter decomposition in one dimension with a spin-configuration: crosses and circles represent the two spin states. Here the interaction resides on the shaded plaquettes.*

Because in each time-step each spin interacts with only one neighbour, it is sufficient to consider a two-spin Hamiltonian which for the quantum Heisenberg antiferromagnet takes the form

$$h = \frac{J}{4}\begin{pmatrix} 1 & 0 & 0 & 0 \\ 0 & -1 & 2 & 0 \\ 0 & 2 & -1 & 0 \\ 0 & 0 & 0 & 1 \end{pmatrix} \qquad (2.5)$$

with the resulting transfer matrix

$$T = \exp(-\varepsilon h) = e^{-\varepsilon J/4}\begin{pmatrix} e^{-\varepsilon J/2} & 0 & 0 & 0 \\ 0 & \cosh(\varepsilon J/2) & -\sinh(\varepsilon J/2) & 0 \\ 0 & -\sinh(\varepsilon J/2) & \cosh(\varepsilon J/2) & 0 \\ 0 & 0 & 0 & e^{-\varepsilon J/4} \end{pmatrix}, \qquad (2.6)$$

defining the transition amplitudes in the basis $\{|\uparrow\uparrow\rangle, |\uparrow\downarrow\rangle, |\downarrow\uparrow\rangle, |\downarrow\downarrow\rangle\}$. The off-diagonal negative elements generally lead to a sign problem. However, since on a bipartite lattice there is always an even number of such transitions, the resulting weight is always positive.

Starting from a configuration as shown in figure 2.1, one proposes plaquette break-ups, which represent constraints that bind certain spins together, making sure that only non-zero matrix elements are generated. As there is spin conservation in the basis chosen here, only the break-ups presented in figure 2.2 are allowed. These break-ups decompose the transfer matrix as

$$T = A\begin{pmatrix} 1 & 0 & 0 & 0 \\ 0 & 1 & 0 & 0 \\ 0 & 0 & 1 & 0 \\ 0 & 0 & 0 & 1 \end{pmatrix} + B\begin{pmatrix} 0 & 0 & 0 & 0 \\ 0 & 1 & -1 & 0 \\ 0 & -1 & 1 & 0 \\ 0 & 0 & 0 & 0 \end{pmatrix} + C\begin{pmatrix} 1 & 0 & 0 & 0 \\ 0 & 0 & -1 & 0 \\ 0 & -1 & 0 & 0 \\ 0 & 0 & 0 & 1 \end{pmatrix}. \tag{2.7}$$

For a Heisenberg antiferromagnet one obtains $A = \cosh(\varepsilon J/2)$, $B = \sinh(\varepsilon J/2)$, and $C = 0$.

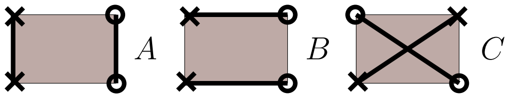

Figure 2.2: *Plaquette break-ups in the Quantum Heisenberg Model.*

The partition function can thus be written in terms of the break-ups

$$Z = \sum_{[s]} A^{N_A} B^{N_B}, \tag{2.8}$$

where N_A (N_B) is the number of A-type (B-type) break-ups.

2.1.1 The Monte Carlo Method

Quantum many-body problems are among the hardest problems in theoretical physics, because the configuration-space grows exponentially with the number of particles N involved. Consequently, it is extremely hard to perform first principles calculations of such systems [27].

That is where the Monte Carlo method enters the stage, with the idea of importance sampling. The partition function described as the sum of configurations in the path integral in eq. (2.3) which can be expressed in terms of the break-ups in eq. (2.8) can now be sampled with the Monte Carlo method. In other words, one generates configurations $[s]$ in the partition function

$$Z = \sum_{[s]} \exp(-S[s]), \tag{2.9}$$

with their Boltzmann weight $\exp(-S[s])$, where $S[s]$ is the Euclidean action of the configuration in the path integral representation. The configurations $[s]$ are generated according to their Boltzmann weight with the probability

$$p[s] = \frac{1}{Z}\exp(-S[s]). \tag{2.10}$$

One generates a set of configurations, a so-called Markov chain

$$[s^{(1)}] \;\rightarrow\; [s^{(2)}] \;\rightarrow\; \cdots \;\rightarrow\; [s^{(n)}], \tag{2.11}$$

where the configuration $[s^{(i+1)}]$ is generated out of $[s^{(i)}$. In this chain one should find $[s]$ in the $n \rightarrow \infty$ limit with probability $p[s]$. Observables can be measured by averaging over the set of configurations generated in the Markow chain

$$\langle \mathcal{O} \rangle = \lim_{n\rightarrow\infty} \frac{1}{n}\sum_{i=1}^{n} \mathcal{O}[s^{(i)}]. \tag{2.12}$$

Due to importance sampling one can perform phase space integrals for many-particle problems, that scale only polynomially with the number of particles N, although the configuration space grows exponentially with N. In order to generate configurations with the correct probability, one has to ensure that the matrix of the transition probabilites $w([s] \rightarrow [s'])$ has eigenvalue 1 for a stationary probability distribution with the eigenvector p in equilibrium, i.e.

$$\sum_{[s]} w([s] \rightarrow [s'])p[s] = p[s']. \tag{2.13}$$

A sufficient but not necessary condition to achieve this is the detailed balance condition

$$\frac{p_{[s]}}{p_{[s']}} = \frac{w([s] \rightarrow [s'])}{w([s] \rightarrow [s'])}. \tag{2.14}$$

Here $w([s] \rightarrow [s'])$ denotes the probability to go from $[s]$ to $[s']$, which, of course, has to be properly normalised, i.e. $\sum_{[s']} w([s] \rightarrow [s']) = 1$.

There are different ways to construct algorithms that obey detailed balance. One simple method is the Metropolis algorithm [29], where a new configuration $[s']$ is proposed and accepted with the probability

$$w([s] \rightarrow [s']) = \min\left[1, \exp\left(-(S[s] - S[s'])\right]. \tag{2.15}$$

And other very simple, but less efficient method, because configurations are more often rejected, is the heat-bath algorithm where new configurations are accepted with the probability

$$w([s] \rightarrow [s']) = \frac{\exp(-S[s'])}{\exp(-S[s]) + \exp(-S[s'])}. \tag{2.16}$$

Furthermore, to achieve an algorithm that correctly samples the whole partition function, we demand ergodicity, i.e.

$$w^n([s] \to [s']) > 0, \text{ for all } [s], \ [s'], \text{ with } n < \infty, \tag{2.17}$$

which is the condition, that every configuration in the partition function must be possible to be generated by the algorithm with non-zero probability.

Monte Carlo algorithms, such as the Metropolis algorithm, generate configurations out of each other. Thus the configurations in the Markov chain are usually not statistically independent. The time it takes to reach a statistically independent configuration is the autocorrelation time τ:

$$\langle \mathcal{O}(t)\mathcal{O}(t+\Delta t)\rangle - \langle \mathcal{O}(t)\rangle^2 \propto \exp(-\Delta t/\tau). \tag{2.18}$$

Simple Metropolis-type algorithms suffer from critical slowing down, i.e. with increasing correlation length ξ at a second order phase transition, the autocorrelation time grows with the power of a factor z

$$\tau \propto \xi^z, \tag{2.19}$$

where z is typically around 2. Thus, in practice such calculations are often still limited to a small number of particles.

With the invention of cluster algorithms for classical and quantum spin systems, the factor z has been reduced to $z < 1$ and in some cases even to $z \approx 0$ [30,31,33].

The calculations performed in this thesis are all performed at a finite volume V and at finite inverse temperature β from which one extrapolates to infinity in both space and time. This is the usual case in a computer simulation. Also one usually imposes periodic boundary conditions on finite-size boxes, e.g. on a two-dimensional square lattice of spatial size $V = L^2$. There exists an infinite volume algorithm, which works at $L = \infty$ and (or) $\beta = \infty$ when the correlation length is finite [45] (which is obviously not the case for the Heisenberg antiferromagnet at $\beta = \infty$). Also there exists a ground state projector Monte Carlo algorithm where one approaches the ground state instead of sampling a thermal bath by acting with the Hamiltonian a trial initial state [46].

2.1.2 Cluster Updates

The procedure is thus to completely fill the system with the break-ups described above. Because on the plaquettes each site is connected with another one via the chosen break-ups, the bonds form closed loops also known as clusters. Now one collectively changes up- to down-spins and vice versa on each cluster. This collective change of a whole cluster is denoted as cluster-flip. Each cluster is flipped with probability $p = \frac{1}{2}$.

This procedure is known as the multi-cluster algorithm. There also exists a single-cluster variant of this procedure, where one randomly starts at a site on the space-time lattice and only builds the cluster attached to that site. When the loop is closed, the cluster is flipped with probability $p = 1$.

2.1.3 Detailed Balance, Ergodicity, and the Reference Configuration

Detailed balance is easy to show on a single plaquette $S[s(x,t), s(x+\hat{\mu},t), s(x,t+1), s(x+\hat{\mu},t+1)]$, where $s(x,t)$ is a spin at the space-time point (x,t) (this is not to be confused with the Euclidean action $S[s]$ of a configuration $[s]$). Only in the configurations $S[\uparrow,\downarrow,\uparrow,\downarrow]$ or $S[\downarrow,\uparrow,\downarrow,\uparrow]$ one can choose between the A and B break-up. In the multi-cluster mode the fraction of transition probabilities for the transition from $S[\uparrow,\downarrow,\uparrow,\downarrow]$ to $S[\uparrow,\uparrow,\uparrow,\uparrow]$ is

$$\frac{w(S[\uparrow\downarrow\uparrow\downarrow] \rightarrow S[\uparrow\uparrow\uparrow\uparrow])}{w(S[\uparrow\uparrow\uparrow\uparrow] \rightarrow S[\uparrow\downarrow\uparrow\downarrow])} = \frac{\frac{1}{2}\frac{1}{2}\frac{c-s}{c}}{\frac{1}{2}\frac{1}{2}} = \frac{c-s}{c} = \frac{p_{\uparrow\uparrow\uparrow\uparrow}}{p_{\uparrow\downarrow\uparrow\downarrow}}. \tag{2.20}$$

Thus detailed balance is satisfied for the transitions between $S[\uparrow\downarrow\uparrow\downarrow]$ and $S[\uparrow\uparrow\uparrow\uparrow]$. For the other cases this can be shown in the same way.

The concept of a reference configuration will help us to show ergodicity. For an antiferromagnet, there is the classical Néel state. Now because the cluster algorithm connects neighbouring spins only when they are antiparallel, on a bipartite lattice it is always possible to get to the classical Néel state from any chosen configuration within one multi-cluster update. Thus we call this classical ground state a reference configuration. Within one multi-cluster update one can get from any configuration to the reference configuration. Hence, by going through the reference configuration with two such updates any allowed configuration can be reached from any other configuration with non-zero probability. Thus ergodicity is shown. When the rules of a cluster algorithm are based on a reference configuration, the cluster size will not grow larger than the physical correlation length, because the clusters can only grow within ordered regions. This prevents the clusters from becoming inefficient due to too large clusters.

2.1.4 Efficiency

The above procedure performs non-local updates. The autocorrelation time is very small, as it has been tested in simulations. Usually very few updates suffice for completely uncorrelated measurements [47].

2.1.5 Measuring Susceptibilities

Both the staggered and the uniform susceptibilities can be efficiently measured by constructing improved estimators using features of the clusters. In discrete time eq. (1.9) takes the form

$$\begin{aligned} \chi_s &= \frac{1}{V}\frac{\beta}{kM}\left\langle \sum_{i=0}^{kM} M_s^3(0) M_s^3(i) \right\rangle = \frac{1}{V}(\frac{\beta}{kM})^2 \frac{1}{\beta}\left\langle \sum_{i=0}^{kM}\sum_{j=0}^{kM} M_s^3(i) M_s^3(j) \right\rangle \\ &= \frac{\beta}{V(kM)^2}\left\langle \left(\sum_{i=0}^{kM} M_s^3 \right)^2 \right\rangle = \frac{\beta}{V(kM)^2}\left\langle (M_s)^2 \right\rangle . \end{aligned} \tag{2.21}$$

While $M_s^3(i)$ is the staggered magnetisation operator at a certain time-slice, $M_s = \sum_{i=0}^{kM} M_s^3(i)$ is the staggered magnetisation summed over Euclidean time The staggered magnetisation can now be written in terms of the cluster decomposition $M_s = \sum_i M_s^{\mathcal{C}_i}$, where each cluster $\mathcal{C}_i$ carries a staggered magnetisation $M_s^{\mathcal{C}_i} = \pm|\mathcal{C}_i|$ which is a multiple of the cluster size $|\mathcal{C}_i|$. The staggered susceptibility then takes the form

$$\chi_s = \frac{\beta}{V(kM)^2}\left\langle \sum_i M_s^{\mathcal{C}_i}\right\rangle^2 = \frac{\beta}{V(kM)^2}\sum_i \langle (M_s^{\mathcal{C}_i})^2\rangle = \frac{\beta}{V(kM)^2}\sum_i \langle |\mathcal{C}_i|^2\rangle, \tag{2.22}$$

because by multiplying out the sum, all mixed terms $M_s^{\mathcal{C}_i} M_s^{\mathcal{C}_j}$ with $i \neq j$ cancel.

In the single-cluster mode a similar formula can be derived. Because clusters are then selected in proportion to their size with probability $p_i = |\mathcal{C}_i|/VkM$, the improved estimator for the staggered susceptibility now takes the form

$$\chi_s = \frac{\beta}{kM}\left\langle \sum_i |\mathcal{C}_i| \frac{|\mathcal{C}_i|}{VkM}\right\rangle = \frac{\beta}{kM}\left\langle |\mathcal{C}|\right\rangle. \tag{2.23}$$

Similarly, in the multi-cluster mode the uniform susceptibility

$$\chi_u = \frac{\beta}{V}\langle W_t^2\rangle = \frac{\beta}{V}\left\langle \sum_i W_t(\mathcal{C}_i)^2\right\rangle \tag{2.24}$$

is given in terms of the temporal winding number $W_t = \sum_{\mathcal{C}} W_i(\mathcal{C})$, which is the sum of winding numbers $W_t(\mathcal{C})$ of the loop-cluster $\mathcal{C}$ around the Euclidean time direction. In the same way spatial winding numbers are defined as $W_i = \sum_{\mathcal{C}} W_i(\mathcal{C})$.

Again, in the single-cluster mode the uniform susceptibility is given by

$$\chi_u = \frac{\beta}{V}\left\langle \sum_i W_t(\mathcal{C}_i)^2 \frac{|\mathcal{C}_i|}{VkM}\frac{VkM}{|\mathcal{C}_i|}\right\rangle = \beta kM \left\langle \frac{W_t(\mathcal{C})^2}{|\mathcal{C}|}\right\rangle. \tag{2.25}$$

2.1.6 Continuous-time Limit

The continuous-time limit can be taken by performing at least three simulations for the same space-time volume at different small ε and fit the calculated averages of an observable $\langle \mathcal{O}\rangle$ to

$$\langle \mathcal{O}(\varepsilon)\rangle = \langle \mathcal{O}\rangle + a\varepsilon^2, \tag{2.26}$$

using $\langle \mathcal{O}\rangle$ and a as fit parameters. The chosen ε have to be already sufficiently small in order to justify neglecting higher order terms. We usually choose $\varepsilon \leq 0.1$.

2.2 Continuous-time Cluster Algorithm

The above procedure has the disadvantage that in order to perform the continuous-time limit several simulations at different ε are needed because the brute-force limit, i.e. $\varepsilon \to 0$, is not possible due to a diverging number of time-slices kM.

The solution is thus not to consider infinitesimal transition probabilities, but to store sporadic transition times in continuous time and update those directly [48]. In the discrete time formulation, for two antiparallel spins, constantly propagating over the time interval $\Delta\tau$, the probability to introduce the transition-type break-up is

$$p = \frac{\Delta\tau}{\varepsilon} \tanh\left(\frac{\varepsilon J}{2}\right). \tag{2.27}$$

Now taking the limit $\varepsilon \to 0$, we get

$$p = \lim_{\varepsilon\to 0} \frac{\Delta\tau}{\varepsilon} \tanh\left(\frac{\varepsilon J}{2}\right) = \frac{\Delta\tau J}{2}. \tag{2.28}$$

The advantage is, that there is no continuous-time limit to be performed. Also memory space is saved, as the spin configuration only has to be recorded once in the path integral. In addition one stores the position of the transitions-type break-ups and whether they keep or change the the orientation of the spins.

The rest of the algorithm, i.e. the loop update, works exactly as in the discrete-time algorithm.

We can interpret the hopping of a spin as a decay process in imaginary Euclidean time, as a sampling of a time-ordered perturbation expansion. One splits the Hamiltonian into a diagonal part H_0 and an off-diagonal part V [42, 49]. The off-diagonal part V is treated as a perturbation. In the interaction representation the time-dependent perturbation is $V(\tau) = \exp(\tau H_0) V \exp(-\tau H_0)$ and can be written as

$$Z = \mathrm{Tr}\left[\exp(-\beta H_0)\mathcal{T}\exp\left(-\int_0^\beta d\tau V(\tau)\right)\right]. \tag{2.29}$$

By expanding the exponential we get

$$Z = \mathrm{Tr}\left[\exp(-\beta H_0)\left(1 - \int_0^\beta d\tau V(\tau) + \frac{1}{2}\int_0^\beta d\tau_1 \int_{\tau_1}^\beta d\tau_2 V(\tau_1)V(\tau_2) + \ldots\right)\right]. \tag{2.30}$$

By viewing the partition function in this way one can already see a connection to the stochastic series expansion (SSE) discussed in section 2.3 which is also a perturbation expansion. Where the continuous-time path-integral is a perturbation expansion in the off-diagonal terms, SSE is a perturbation expansion in all terms of the Hamiltonian.

2.2.1 Measuring Susceptibilities

Again the staggered and the uniform susceptibilities can be efficiently measured by using improved estimators. In the multi-cluster version of the algorithm the staggered susceptibility is given in terms of the space-time cluster size $|\mathcal{C}|$, i.e.

$$\chi_s = \frac{1}{\beta V}\left\langle \sum_{\mathcal{C}} |\mathcal{C}|^2 \right\rangle, \tag{2.31}$$

and the uniform susceptibility is given by

$$\chi_u = \frac{\beta}{V}\langle W_t^2\rangle = \frac{\beta}{V}\left\langle \sum_{\mathcal{C}} W_t(\mathcal{C})^2 \right\rangle . \tag{2.32}$$

2.3 Stochastic Series Expansion

Stochastic series expansion (SSE) is a similar method based on a high temperature expansion [50]. The partition function Z is then rewritten as

$$\begin{aligned} Z &= \operatorname{Tr}\exp(-\beta H) = \sum_{n=0}^{\infty} \frac{(-\beta)^n}{n!}\operatorname{Tr}(H^n) \\ &= \sum_{n=0}^{\infty} \frac{\beta^n}{n!} \sum_{|\alpha\rangle} \sum_{(b_1 \ldots b_n)} \langle\alpha| \prod_{i=1}^{n} (-H_{b_i})|\alpha\rangle, \end{aligned} \tag{2.33}$$

where b_i denotes all possible bonds, i.e. all pairs $\langle xy\rangle$ of neighbouring spins.

In order to get positive weights, all H_{b_i} should be negative. For the diagonal entries in the Hamiltonian this can easily be achieved by an energy-shift E_s

$$H_{b_i} = \begin{pmatrix} \frac{J}{4} - E_s & 0 & 0 & 0 \\ 0 & -\frac{J}{4} - E_s & \frac{J}{2} & 0 \\ 0 & \frac{J}{2} & -\frac{J}{4} - E_s & 0 \\ 0 & 0 & 0 & \frac{J}{4} - E_s \end{pmatrix} . \tag{2.34}$$

A good choice of E_s is $E_s = \frac{J}{4}$. The off-diagonal matrix elements are potentially dangerous and will cause a sign problem on frustrated lattices. On bipartite lattices there is always an even number of such matrix elements and there is no sign problem.

In SSE one samples an operator string of variable length n. For convenience one can replace this with an operator string of fixed length Λ, by adding extra identity operators

$$Z = \sum_{n=0}^{\infty} \sum_{|\alpha\rangle} \sum_{(b_1 \ldots b_n)} \frac{(\Lambda - n)!\beta^n}{\Lambda!} \langle\alpha| \prod_{i=1}^{n} (-H_{b_i})|\alpha\rangle . \tag{2.35}$$

This is usually easier to realise in a computer, because one does not have to update the length of the operator string. Furthermore, showing ergodicity is not as straightforward to show as in the case of the fixed length operator string as long as Λ is bigger than the number of non-unit-matrix operators, this cut-off does not alter any results and if n approaches Λ one can always increase Λ, which is a procedure usually performed during the thermalisation of the simulation.

The update of the system works in two steps:

1. insert and remove operators. As a replacement of a unit operator we propose with probability
$$P_{1\to H^d_{b_i}} = \min\left(1, \frac{\beta N_b \langle\alpha|H^d_{b_i}|\alpha\rangle}{\Lambda - n}\right) \tag{2.36}$$
a diagonal operator, where N_b is the number of bonds. In place of a diagonal operator we propose a unit operator with probability
$$P_{H^d_{b_i}\to 1} = \min\left(1, \frac{\Lambda - n + 1}{\beta N_b \langle\alpha|H^d_{b_i}|\alpha\rangle}\right). \tag{2.37}$$
2. Perform a loop update as above.

It is striking how similar the continuous time path integral formulation and SSE are. That is no coincidence. There exists an exact mapping between one and the other by integrating out the transition times while keeping the time ordering of the transitions fixed.

2.3.1 Measuring Susceptibilities

Again the uniform susceptibility can be measured using the temporal winding numbers of the individual loops [51]:
$$\chi_u = \frac{\beta}{V}\langle W_t^2\rangle = \frac{\beta}{V}\left\langle \sum_{\mathcal{C}} W_t(\mathcal{C})^2 \right\rangle. \tag{2.38}$$

The staggered susceptibility
$$\chi_s = \frac{1}{V}\int_0^\beta dt' \langle M_s^3(0) M_s^3(t')\rangle, \tag{2.39}$$

which is an integral over imaginary time, can be calculated in the following way
$$\begin{aligned}
\chi_s &= \frac{1}{Z}\frac{1}{V}\int_0^\beta dt' \mathrm{Tr}\left[M_s^3 \exp(-(\beta - t')H) M_s^3 \exp(-t'H)\right] \\
&= \frac{1}{Z}\frac{1}{V}\int_0^\beta \sum_{m=0}^\infty \sum_{k=0}^\infty \frac{(t'-\beta)^m}{m!}\frac{(-t')^k}{k!} \mathrm{Tr}\left[M_s^3 H^m M_s^3 H^k\right] \\
&= \frac{1}{Z}\frac{1}{V}\frac{\beta}{m+k+1}\sum_{m=0}^\infty \sum_{k=0}^\infty \frac{(-\beta)^{m+k}}{(m+k)!} \mathrm{Tr}\left[M_s^3 H^m M_s^3 H^k\right].
\end{aligned} \tag{2.40}$$

Now we use $n = m + k$ and thus obtain

$$\begin{aligned}
\chi_s &= \frac{1}{Z}\frac{\beta}{V}\frac{1}{n+1}\sum_{n=0}^{\infty}\sum_{k=0}^{n}\frac{(-\beta)^n}{n!}\mathrm{Tr}[M_s^3 H^{n-k} M_s^3 H^k] \\
&= \frac{1}{Z}\frac{\beta}{V}\frac{1}{n+1}\sum_{n=0}^{\infty}\frac{(-\beta)^n}{n!}\left\{\sum_{k=1}^{n}\mathrm{Tr}[M_s^3 H^{n-k} M_s^3 H^k] + \mathrm{Tr}[M_s^3 M_s^3 H^n]\right\} \\
&= \frac{\beta}{V}\frac{1}{n+1}\left[\left\langle\sum_i M_{s0}^3 M_{si}^3\right\rangle + \langle M_{s0}^3 M_{s0}^3\rangle\right] \\
&= \frac{\beta}{V}\frac{1}{(n+1)}\left[\frac{1}{n}\left\langle\sum_{i,j} M_{si}^3 M_{sj}^3\right\rangle + \frac{1}{n}\left\langle\sum_i M_{si}^3 M_{si}^3\right\rangle\right] \\
&= \frac{\beta}{V}\frac{1}{(n+1)n}\left[\left\langle(\sum_{i=1}^{n} M_{si})^2\right\rangle + \left\langle\sum_{i=1}^{n} M_{si}^2\right\rangle\right], \qquad (2.41)
\end{aligned}$$

where M_{si}^3 and M_{sj}^3 are the staggered magnetisations at the operators i and j with an operator string of length n.

Chapter 3

Low-Energy Magnon Effective Field Theory

As an underlying microscopic system we consider the quantum Heisenberg model

$$H = J \sum_{\langle xy \rangle} \vec{S}_x \cdot \vec{S}_y - \sum_x \vec{M}_s \cdot \vec{B}_s \tag{3.1}$$

with an external staggered magnetic field $\vec{B}_s$. In the infinite volume limit at zero temperature and with $\vec{B}_s = 0$, $\vec{M}_s$ develops a non-zero vacuum expectation value signalling the spontaneous breakdown of the $SU(2)_s$ spin symmetry to its $U(1)_s$ subgroup.

The low-energy physics of two-dimensional antiferromagnets on bipartite lattices is governed by the spontaneous symmetry breaking of the global $SU(2)_s$ spin symmetry to $U(1)_s$ at zero temperature. This means that the staggered magnetisation

$$\vec{M}_s = \sum_x \vec{S}_x (-1)^x, \quad (-1)^x = 1 \text{ for all } x \in A, \quad (-1)^x = -1 \text{ for all } x \in B \tag{3.2}$$

spontaneously chooses a direction with non-zero expectation value of $\vec{M}_s$. What remains of the $SU(2)_s$ spin rotation symmetry is $U(1)_s$ which are rotations around the direction of $\vec{M}_s$. As a result there are two massless Goldstone bosons — the antiferromagnetic spinwaves or magnons — described by fields in the coset space $SU(2)_s/U(1)_s$. The low-energy magnon physics is described by an effective field theory, the $(2+1)$-d $O(3)$-invariant non-linear σ-model.

3.1 Leading Order Action

In analogy to chiral perturbation theory for the pseudo-Goldstone bosons in QCD — the pions — a systematic low-energy effective field theory for magnons was developed in [17–21]. The local staggered magnetisation of an antiferromagnet is described as a unit-vector field

$$\vec{e}(x) = (\vec{e_1}(x), \vec{e_2}(x), \vec{e_3}(x)), \qquad \vec{e}(x)^2 = 1. \tag{3.3}$$

Here, $x = (x_1, x_2, t)$ denotes a point in $(2+1)$-d space-time.

The effective action is constructed by writing down all possible terms consisting of the field $\vec{e}$ and its derivatives up to a certain order that are invariant under the symmetries of the system (the $SU(2)_s$ spin symmetry, time reversal T and discrete lattice symmetries). Because the magnons have a relativistic spectrum, spatial and temporal derivatives are counted in the same way and thus no term with only one derivative is allowed.

To leading order, the Euclidean magnon effective action takes the form

$$S[\vec{e}] = \int d^2x \ dt \ \frac{\rho_s}{2} \left[\left(\partial_i \vec{e} \cdot \partial_i \vec{e} + \frac{1}{c^2} \partial_t \vec{e} \cdot \partial_t \vec{e} \right) - \mathcal{M}_s \vec{e} \cdot \vec{B}_s \right]. \tag{3.4}$$

The low-energy constants ρ_s, c, and $\mathcal{M}_s$ are not determined by the effective field theory, but have to be determined externally. In our case we will determine them by performing Monte Carlo simulations of the underlying microscopic system. The low-energy constant $\mathcal{M}_s$ in the term of the external staggered magnetic field is the same as in the definition of the staggered susceptibility in eq. (3.7). In the further discussion we will remove the term $\mathcal{M}_s \vec{e} \cdot \vec{B}_s$ from the action, because we will work without an external staggered magnetic field, still keeping in mind that $\mathcal{M}_s$ takes non-zero value due to spontaneous symmetry breaking which is the reason why it appears in the definition of the staggered susceptibility in eq. (3.7).

The spatial directions are labeled with $i \in \{1, 2\}$ and the index t denotes the Euclidean time-direction. This Lagrangian is the same to leading order irrespective of the underlying lattice structure for two-dimensional bipartite lattices, provided that there are appropriate discrete lattice symmetries and $SU(2)_s$ breaks to $U(1)_s$. The low-energy parameter ρ_s is the spin-stiffness whereas c is the spinwave velocity. At low energies the antiferromagnet has a relativistic spectrum. Hence, by introducing $x_0 = ct$ the action takes the manifestly Lorentz-invariant form

$$S[\vec{e}] = \int d^2x \ dx_0 \ \left[\frac{\rho_s}{2c} \partial_\mu \vec{e} \cdot \partial_\mu \vec{e} \right]. \tag{3.5}$$

The ratio $\xi = c/(2\pi\rho_s)$ defines a characteristic length scale which diverges when antiferromagnetism disappears at a second order phase transition at zero temperature. This not to be confused with the physical correlation length ξ introduced in chapter 1.

3.2 Calculations at Finite Volume and Temperature

Hasenfratz and Niedermayer have performed very detailed calculations of a variety of physical quantities including the next-to-next-to-leading order (NNLO) of the systematic low-energy expansion [19–21]. In particular, the results from computer simulations to the finite volume and non-zero temperature can be fitted to their calculations at finite volume and non-zero temperature. Thus we have a way to extract the infinite volume low-energy effective field theory constants from finite-size simulations. Depending on the size of the spatial extension L of a quadratic periodic spatial volume and the inverse temperature β, different space-time geometries can be distinguished. A cubical space-time volume where

$L \approx \beta c$, a cylindrical volume where $L \ll \beta c$ and a slab geometry where $L \gg \beta c$. The aspect ratio of the space-time box is characterised by

$$l = \left(\frac{\beta c}{L}\right)^{1/3}. \tag{3.6}$$

In the cubical regime the volume- and temperature-dependence of the staggered magnetisation is given by

$$\chi_s = \frac{\mathcal{M}_s^2 L^2 \beta}{3} \left\{ 1 + 2\frac{c}{\rho_s L l}\beta_1(l) + \left(\frac{c}{\rho_s L l}\right)^2 \left[\beta_1(l)^2 + 3\beta_2(l)\right] + ... \right\}, \tag{3.7}$$

where $\mathcal{M}_s$ is the staggered magnetisation density. The uniform susceptibility takes the form

$$\chi_u = \frac{2\rho_s}{3c^2} \left\{ 1 + \frac{1}{3}\frac{c}{\rho_s L l}\widetilde{\beta}_1(l) + \frac{1}{3}\left(\frac{c}{\rho_s L l}\right)^2 \left[\widetilde{\beta}_2(l) - \frac{1}{3}\widetilde{\beta}_1(l)^2 - 6\psi(l)\right] + ... \right\}. \tag{3.8}$$

The functions $\beta_i(l)$, $\widetilde{\beta}_i(l)$, and $\psi(l)$ are shape coefficients of the space-time box defined in [21].

In order to extract the low-energy constants ρ_s, c, and the staggered magnetisation $\mathcal{M}_s$, one can perform a series of simulations with increasing L and β and simultaneously fit the obtained data to eqs. (3.7) and (3.8), using ρ_s, c, and $\mathcal{M}_s$ as fit parameters. In the cubical regime l is tuned to $l \approx 1$. In order to find the cubical regime on can measure winding numbers. If the expectation values of the square of the spatial and of the temporal winding numbers are approximately equal, i.e. $\langle W_i^2 \rangle \approx \langle W_t^2 \rangle$, then $L \approx \beta c$ and thus we are in the cubical regime.

If L is large, it is sufficient to fit to eqs. (3.7) and (3.8) because the neglected subleading corrections are of the order $\mathcal{O}(Ll)^{-3}$ and can thus be neglected.

In the very low temperature limit, one enters the cylindrical regime of space-time volumes with $\beta c \gg L$. In this case, the staggered magnetisation vector $\vec{M}_s$ acts as a quantum rotor and, correspondingly, the low-energy end of the spectrum takes the form

$$E_S = \frac{S(S+1)}{2\Theta}. \tag{3.9}$$

Here $S \in \{0, 1, 2, ...\}$ is the spin and Θ is the moment of inertia of the quantum rotor which is given by [21]

$$\Theta = \frac{\rho_s L^2}{c^2}\left[1 + \frac{3.900265 c}{4\pi\rho_s L} + O\left(\frac{1}{L^2}\right)\right]. \tag{3.10}$$

The partition function of the $(2S{+}1)$-fold degenerate rotor spectrum is given by

$$Z = \sum_{S=0}^{\infty} (2S+1)\exp\left(-\beta E_S\right). \tag{3.11}$$

The probability distribution of the uniform magnetisation $M^3 = S^3$ is then given by

$$p(M^3) = \frac{1}{Z} \sum_{S \geq |M^3|} \exp\left(-\beta E_S\right). \tag{3.12}$$

3.3 Low-Energy Constants for the Square Lattice

The parameters ρ_s, $\mathcal{M}_s$, and c of a spin $\frac{1}{2}$ Heisenberg antiferromagnet on a square lattice have been extracted in [46–48, 52]. In a recent study [53] , these low-energy parameters are discussed in more detail and are further determined to higher precision with the resulting low-energy constants

$$\mathcal{M}_s = 0.30743(1)/a^2, \quad \rho_s = 0.1808(4)J, \quad c = 1.6585(10)Ja. \tag{3.13}$$

Chapter 4

Effective Field Theory and Simulation of the Spin $\frac{1}{2}$ Heisenberg Model on the Honeycomb Lattice

Like the square lattice, the honeycomb lattice is a two-dimensional bipartite lattice with appropriate discrete lattice symmetries such that at zero temperature $SU(2)_s$ breaks down to $U(1)_s$. Thus we expect similar low-energy physics although the symmetries are not exactly the same. The work presented in this chapter has been published in [7].

4.1 Simulation Set-up on a Honeycomb Lattice

In order to simulate the Heisenberg antiferromagnet on a honeycomb lattice, we put it into a rectangular box with periodic boundary conditions. The honeycomb lattice shown in figure 4.1a contains 3 × 3 elementary cells shown in 4.1b. The lattice spacing a is the distance between two neighbouring sites.

If one simulates using the discrete time algorithm, three Suzuki-Trotter decomposition steps are required, i.e. $H = H_1 + H_2 + H_3$. Here H_1 contains all bonds in the $(1, 0)$ direction, H_2 contains the interactions on the bonds in the $(\frac{1}{2}, \frac{\sqrt{3}}{2})$ direction, and H_3 contains the bonds in the $(-\frac{1}{2}, \frac{\sqrt{3}}{2})$ direction on a lattice as shown in figure 4.1.

4.2 Magnon Effective Theory

As on the square lattice, on the honeycomb lattice there is spontaneous symmetry breaking at zero temperature, where the staggered magnetisation spontaneously chooses a direction and takes a non-zero expectation value. Thus the same methods as described in chapter 3 can be applied here. The discrete lattice symmetries are not the same, but to leading

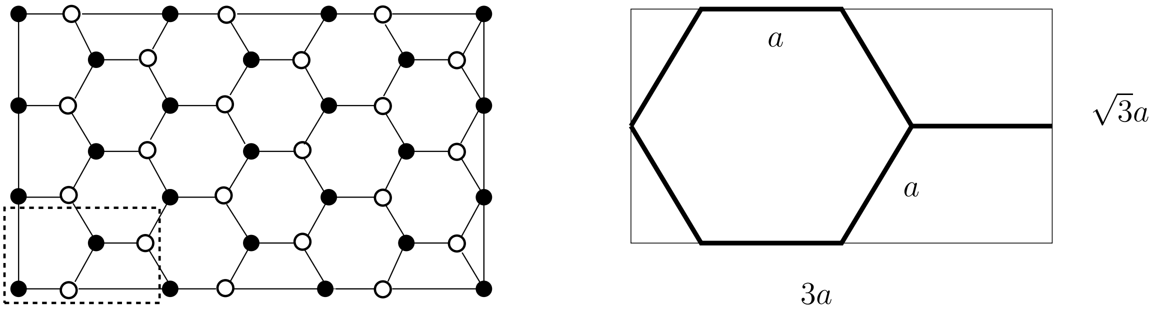

Figure 4.1: *a) The periodic honeycomb lattice consisting of two triangular sublattices A and B, which are depicted by solid and open circles, respectively. The dashed rectangle is an elementary cell for building a periodic honeycomb lattice covering a rectangular area. b) Elementary cell of a honeycomb lattice which has the size* $3a \times \sqrt{3}a$.

order the Euclidean magnon low-energy effective action takes the same form

$$S[\vec{e}] = \int d^2x \ dt \ \frac{\rho_s}{2} \left(\partial_i \vec{e} \cdot \partial_i \vec{e} + \frac{1}{c^2} \partial_t \vec{e} \cdot \partial_t \vec{e} \right) . \tag{4.1}$$

This effective action has been derived in the same way as described in chapter 3. Again all terms with up to two derivatives were constructed and checked whether they are invariant under the symmetries of the quantum Heisenberg antiferromagnet on the honeycomb lattice. Although the lowest-order action is the same as on the square lattice, higher-order terms are affected by the lattice symmetries. The symmetries of the honeycomb lattice are discussed in chapter 11.

We again perform simulations of a finite-size space-time box and fit our data to eqs. (3.7) and (3.8), derived in the cubical regime. The aspect ratio of the spatially quadratic space-time box is characterised by $l = (\beta c/L)^{1/3}$, with which one distinguishes cubical space-time volumes with $L \approx \beta c$ from cylindrical ones with $\beta c \gg L$ and slab geometries with $\beta c \ll L$.

Because we work in the cubical regime we have to make sure that $L_x \approx L_y \approx \beta c$. This can be determined by the condition that the spatial and temporal winding numbers should be approximately equal $\langle W_1^2 \rangle \approx \langle W_2^2 \rangle \approx \langle W_t^2 \rangle$ (which implies $\beta c \approx L$). Because the effective field theory calculations were done on a spatially exactly quadratic lattice we tried to approach this as closely as possible. However, it is obviously not possible to construct an exact square, because it is built out of $3a \times \sqrt{3}a$ size unit cells shown in figure 4.1b. Hence, we simulated different lattices close to a square and then performed a linear interpolation to a perfect square shape. For example, we simulated an 11×19 elementary cell ($= 33a \times 32.91a$) and a 11×20 elementary cell lattice ($= 33a \times 34.64a$) and performed a linear interpolation to an exact $33a \times 33a$ lattice (which would correspond to 11×19.05 unit cells).

Instead of considering the staggered magnetisation density $\mathcal{M}_s$ of eqs. (3.7) and (3.8),

βJ	N_1	N_2	N_{Spin}	$\chi_s Ja$	$\langle W_t^2 \rangle$
24	11	19	836	575.14(82)	7.828(15)
25	11	19	836	597.58(85)	7.494(15)
26	11	19	836	620.91(85)	7.177(15)
34	15	26	1560	1450(3)	10.113(20)
35	15	26	1560	1496(3)	9.797(21)
36	15	26	1560	1532(3)	9.491(22)
44	19	33	2508	2936(5)	12.411(25)
45	19	33	2508	3001(5)	12.145(25)
46	19	33	2508	3061(5)	11.848(26)
48	22	38	3344	4220(6)	15.137(28)
49	22	38	3344	4308(7)	14.796(26)
50	22	38	3344	4392(7)	14.495(28)
59	26	45	4680	7151(11)	17.123(29)
60	26	45	4680	7286(11)	16.838(29)
61	26	45	4680	7401(12)	16.557(31)

Table 4.1: *Some numerical data for the staggered susceptibility* χ_s *and the temporal winding number squared* $\langle W_t^2 \rangle$ *obtained with the loop-cluster algorithm.* N_1 *and* N_2 *count the number of copies of elementary rectangles in the* 1- *and* 2-*direction and* $N_{Spin} = 4N_1N_2$ *is the corresponding number of spins.*

we choose to quote the staggered magnetisation per spin $\widetilde{\mathcal{M}_s}$, which is related to $\mathcal{M}_s$ by

$$\widetilde{\mathcal{M}_s} = \frac{3\sqrt{3}}{4}\mathcal{M}_s a^2. \tag{4.2}$$

The reason is that we want to be able to compare the results to the calculations done on the square lattice. Thus it is better to compare the staggered magnetisation per spin, than the staggered magnetisation density, because on the honeycomb lattice there are less spins per volume than on the square lattice.

4.3 Determination of the Low-Energy Parameters of the Magnon Effective Theory

Some numerical data from our simulations are listed in table 4.3. By fitting χ_s and χ_u simultaneously to eq. (3.7) and eq. (3.8), we find

$$\widetilde{\mathcal{M}_s} = 0.2688(3),\ \rho_s = 0.102(2)J,\ c = 1.297(16)Ja \tag{4.3}$$

with χ^2/d.o.f. $\approx$ 1.05 as shown in figures 4.2a and 4.2b. The low-energy constants ρ_s and c are determined with high accuracy (at the percent level) and the error of $\widetilde{\mathcal{M}_s}$ is

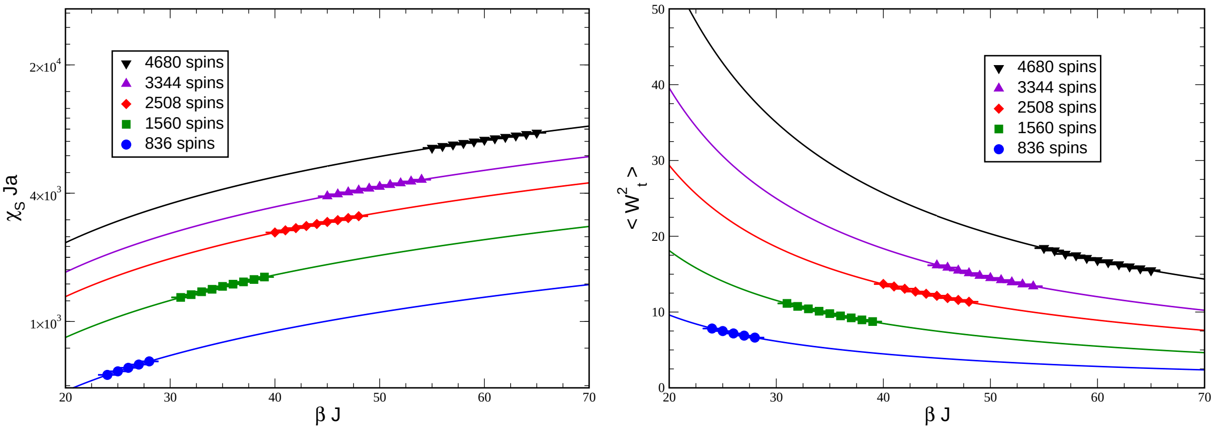

Figure 4.2: *a) Fit of the finite-size and finite-temperature effects of the staggered susceptibility χ_s to results of the effective theory in the cubical regime. b) Fit of the finite-size and finite-temperature effects of the temporal winding number squared $\langle W_t^2 \rangle$ to the results of the effective theory in the cubical regime.*

even at the permille level. The value of c obtained here is consistent with the one of a spinwave expansion study [54]. The above value of $\widetilde{\mathcal{M}}_s$ is larger than the one of a previous spinwave expansion [55] but consistent with that of a series expansion study [56] (within the comparably large 4 percent error of that study). It is only slightly larger than the value obtained in a previous Monte Carlo calculation $\widetilde{\mathcal{M}}_s = 0.2677(6)$ [57]. We want to point out that our results are obtained by fitting more than 80 numerical data points to two analytic predictions with only 3 unknown parameters. If $\widetilde{\mathcal{M}}_s$ is fixed to 0.2677, the quality of our fit downgrades to $\chi^2/\text{d.o.f.} \approx 3.0$. The reduction of $\widetilde{\mathcal{M}}_s = 0.2688(3)$ and $\rho_s = 0.102(2)J$ on the honeycomb lattice compared to those on the square lattice ($\widetilde{\mathcal{M}}_s = 0.3074(4)$, $\rho_s = 0.186(4)J$ [47, 48]) indicates larger quantum fluctuations on the honeycomb lattice. This is expected since the coordination number of the honeycomb lattice is smaller than the one of the square lattice.

4.3.1 Effective Theory Predictions in the Cylindrical Regime

Having determined the values of the low-energy parameters $\widetilde{\mathcal{M}}_s$, ρ_s, and c from the cubical space-time volume regime, we can test the effective theory in the cylindrical regime. Figure 4.3 shows a comparison of the effective theory prediction for the probability distribution $p(M^3)$ of eq. (3.12) with Monte Carlo data. The observed excellent agreement — which does not involve any adjustable parameters — confirms the quantitative correctness of the effective theory.

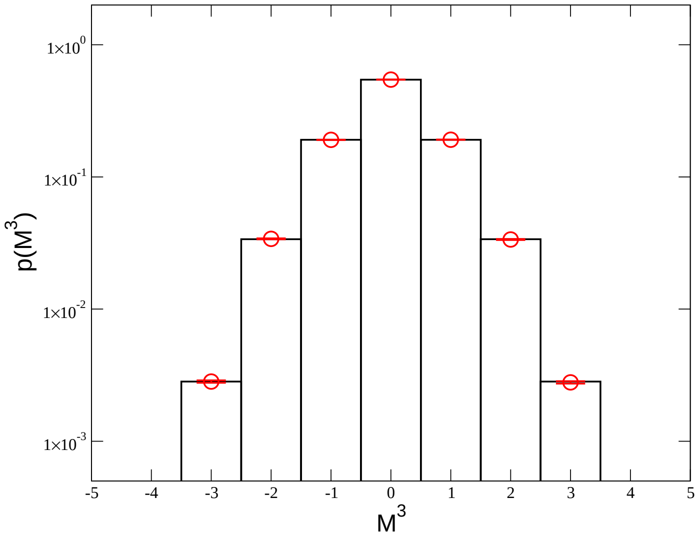

Figure 4.3: *Comparison of the effective theory prediction for the probability distribution* $p(M^3)$ *of eq. (3.12) with Monte Carlo data on an* $N_1 \times N_2 = 11 \times 19$ *honeycomb lattice with* $N_{Spin} = 836$ *at* $\beta J = 60$*. The open circles are the Monte Carlo data while the histogram is the effective theory prediction.*

4.3.2 Outlook on the t-J Model for Fermion Doping

Because the t-J model at half-filling is equivalent to the Heisenberg model one can ask what happens when one moves away from half-filling by doping the system with holes. This can be done to some extent numerically and there is also an effective field theory that describes this system. This question plays a major role in part III of this thesis and is discussed, in particular, for the honeycomb lattice in chapter 11.

Chapter 5

The Heisenberg Model on a Square Lattice with Spatially Anisotropic Couplings

Heisenberg models with spatially anisotropic couplings have been intensively studied [58–62]. Recently, these models have drawn a lot of theoretical attention, because numerical evidence indicates that the anisotropic Heisenberg model with staggered anisotropic arrangement of the antiferromagnetic couplings may belong to a new universality class, in contradiction to the $O(3)$ universality predictions.

Since the anisotropy of the spin stiffness ρ_s in the spin $\frac{1}{2}$ Heisenberg model with spatially anisotropic couplings J_1 and J_2 has not been studied in detail before from first principles Monte Carlo calculations, we perform such simulations to extract the low-energy effective theory parameters ρ_{s1} and ρ_{s2}, the staggered magnetisation density $\mathcal{M}_s$, the spinwave velocity c and the ground state energy density e_0.

The work presented in this chapter has been published in [8].

5.1 Spatially Anisotropic Heisenberg Model

The Hamiltonian of the two-dimensional spatially anisotropic spin $\frac{1}{2}$ Heisenberg model, as depicted in figure 5.1 is defined as

$$H = \sum_x \left[J_1 \vec{S}_x \cdot \vec{S}_{x+\hat{1}} + J_2 \vec{S}_x \cdot \vec{S}_{x+\hat{2}} \right], \tag{5.1}$$

where $\hat{1}$ and $\hat{2}$ are the two unit-vectors in the x- and y-direction. By setting $J_1 > 0$ and $J_2 > 0$, the system is antiferromagnetic.

In order to perform Monte Carlo simulations, we put the system in a space-time box of size $L_1 \times L_2 \times \beta$. Observables of interest are the staggered and the uniform susceptibilities introduced in chapter 2.

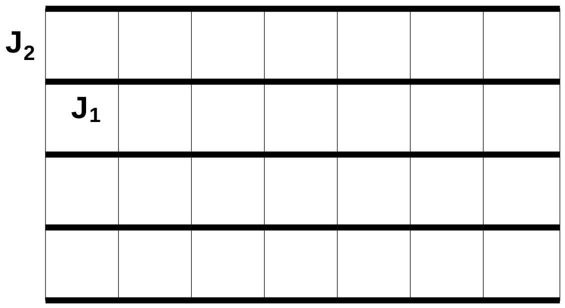

Figure 5.1: *The anisotropic Heisenberg model investigated in this study.* J_1 *and* J_2 *are the antiferromagnetic couplings in the* 1- *and* 2-*directions, respectively.*

5.2 Low-Energy Effective Theory for Magnons

Again as discussed in chapter 3, due to the spontaneous symmetry breaking of the $SU(2)_s$ spin symmetry to a $U(1)_s$ subgroup, the low-energy physics is governed by two massless Goldstone bosons, the magnons. To leading order the effective action takes the form

$$S[\vec{e}] = \int_0^{L_1} dx_1 \int_0^{L_2} dx_2 \int_0^{\beta} dt \left(\frac{\rho_{s1}}{2}\, \partial_1 \vec{e} \cdot \partial_1 \vec{e} + \frac{\rho_{s2}}{2}\, \partial_2 \vec{e} \cdot \partial_2 \vec{e} + \frac{\rho_s}{2c^2}\, \partial_t \vec{e} \cdot \partial_t \vec{e} \right), \tag{5.2}$$

where the index i labels the spatial directions and t refers to the Euclidean time-direction. The parameters $\rho_s = \sqrt{\rho_{s1}\rho_{s2}}$, ρ_{s1} and ρ_{s2} are the spin stiffnesses in the temporal and spatial directions and c is the spinwave velocity. Because we want to fit our Monte Carlo data to the predictions of eqs. (3.7) and (3.8) as well as to the calculation of the internal energy density [21]

$$e = e_0 - \frac{1}{3\beta L^2} \left\{ 1 + l \frac{d}{dl} \beta_0(l) \frac{c}{\rho_s L l} \left[\beta_1(l) - l \frac{d}{dl} \beta_1(l) \right] + O\left(\frac{1}{L^2}\right) \right\}, \tag{5.3}$$

— all derived in the cubical regime characterised by the condition $\beta c \approx L$ — we have to rescale our anisotropic lattice to a square lattice (the parameter e_0 is the ground state energy density). We thus rescale $x_1' = (\rho_{s2}/\rho_{s1})^{1/4} x_1$ and $x_2' = (\rho_{s1}/\rho_{s2})^{1/4} x_2$ and the action then takes the form

$$S[\vec{e}] = \int_0^{L_1'} dx_1' \int_0^{L_2'} dx_2' \int_0^{\beta} dt\, \frac{\rho_s}{2} \Big(\partial_i' \vec{e} \cdot \partial_i' \vec{e} + \frac{1}{c^2} \partial_t \vec{e} \cdot \partial_t \vec{e} \Big). \tag{5.4}$$

Additionally requiring $L_1' = L_2' = L$, it obeys the condition of a square shape, with $L_1' = (\rho_{s2}/\rho_{s1})^{1/4} L_1$ and $L_2' = (\rho_{s1}/\rho_{s2})^{1/4} L_2$.

5.3 Determination of the Low-Energy Parameters

In order to determine the low-energy constants of the anisotropic Heisenberg model given in eq. (5.2), we have performed simulations within the range $0.05 \leq J_2/J_1 \leq 1.0$. The cubical

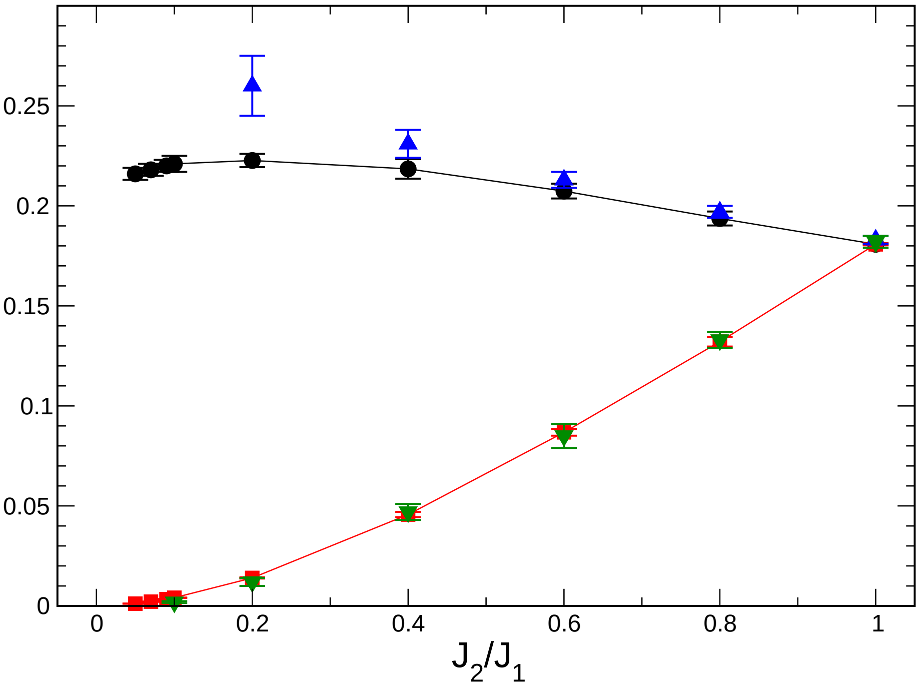

Figure 5.2: *The J_2/J_1-dependence of the spin stiffnesses ρ_{s1} and ρ_{s2} in units of J_1 of the anisotropic Heisenberg model. While the solid circles and squares are the Monte Carlo results of ρ_{s1} and ρ_{s2}, respectively, the up and down triangles are the series expansion results of [63] for ρ_{s1} and ρ_{s2}, respectively. The solid lines are added to guide the eye.*

regime is determined by the condition that the spatial and temporal winding numbers have to be approximately equal $\langle W_1^2 \rangle \approx \langle W_2^2 \rangle \approx \langle W_t^2 \rangle$ (which implies $\beta c \approx L$). Notice that since $J_2 \leq J_1$ in our simulations, one must increase the lattice size L_1 in order to fulfil the condition $\langle W_1^2 \rangle = \langle W_2^2 \rangle$ because eqs. (5.3), (3.7), and (3.8) are obtained for a (2 + 1)-dimensional box with equal extent in the two spatial directions. Therefore, an interpolation of the data points is required in order to be able to use eqs. (5.3), (3.7), and (3.8). The low-energy parameters are extracted by fitting the Monte Carlo data to the effective field theory predictions. Figure 5.2 shows ρ_{s1} and ρ_{s2}, obtained from the fits, as functions of the ratio of the antiferromagnetic couplings, J_2/J_1. The values of ρ_{s1} (ρ_{s2}) obtained here agree quantitatively with those obtained using the series expansion in [63] at $J_2/J_1 = 0.8$ and 0.6 (0.8, 0.6, 0.4, and 0.2). At $J_2/J_1 = 0.4$, the value we obtained for ρ_{s1} is only slightly below the corresponding series expansion result in [63]. However, sizeable deviations begin to show up for stronger anisotropies. Further, we have not observed the saturation of ρ_{s1} to a one-dimensional limit, namely $0.25J_1$ as suggested in [63], even at J_2/J_1 as small as 0.05. In particular, ρ_{s1} decreases slightly as one moves from $J_2/J_1 = 0.1$

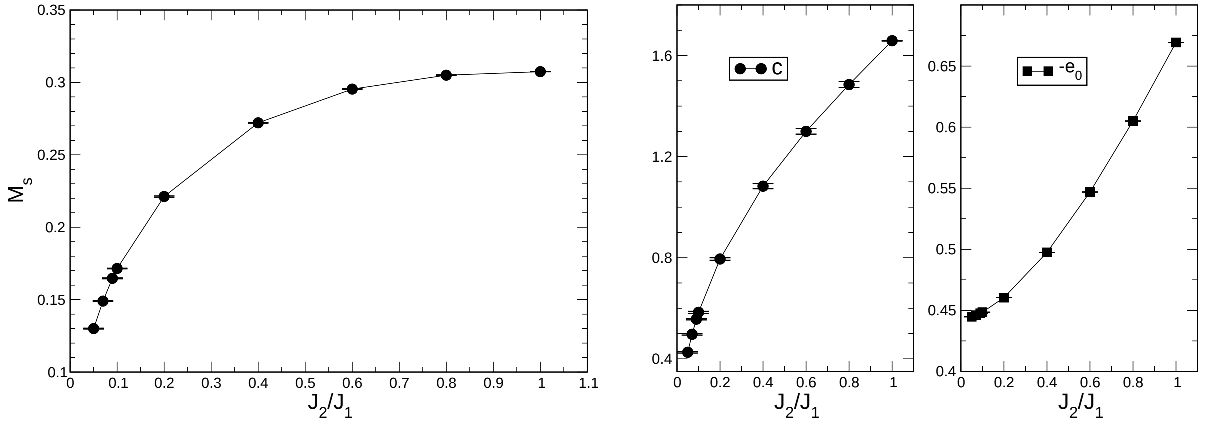

Figure 5.3: *a) The* J_2/J_1*-dependence of the staggered magnetisation density* $\mathcal{M}_s$ $[1/a^2]$ *of the anisotropic Heisenberg model. b) The* J_2/J_1*-dependence of the spinwave velocity* c $[J_1 a]$ *and c) minus the ground state energy density* e_0 $[J_1/a^2]$ *(right) of the anisotropic Heisenberg model. The solid lines are added to guide the eye.*

to $J_2/J_1 = 0.05$, although they still agree within statistical errors. Of course, one cannot rule out that the anisotropies in J_2/J_1 considered here are still too far away from the regime where this particular Heisenberg model can be effectively described by its one-dimensional limit.

On the other hand, the Heisenberg model considered here and its one-dimensional limit are two rather different systems as there is spontaneous symmetry breaking in two-dimensional, but not in one-dimensional systems. We can only approach the limit from one side, i.e. from the two-dimensional Heisenberg antiferromagnet with spatially anisotropic couplings, where there is spontaneous symmetry breaking at zero temperature.

Once J_2/J_1 is truly zero, the system is no longer two-dimensional, but consists of decoupled Haldane spin chains. In one dimension there is no symmetry breaking even though the correlation length diverges.

Thus, the low-temperature behaviour of χ_u in the one-dimensional system is known to be completely different from that of the two-dimensional system [21, 64].

Although intuitively one might expect a continuous transition of ρ_{s1}, one cannot rule out an unexpected behaviour of ρ_{s1} as one moves from this Heisenberg model toward its limit in one dimension. In particular, since earlier studies indicate that long-range order already sets in even for infinitesimally small values of J_2/J_1 [59, 60, 65–67], it would be interesting to consider even stronger anisotropies J_2/J_1 than those used in this study to see how ρ_{s1} approaches its one-dimensional limit.

In addition to the J_2/J_1-dependence of the spin stiffnesses ρ_{s1} and ρ_{s2}, we have calculated the staggered magnetisation density $\mathcal{M}_s$, the spinwave velocity c, as well as the ground state energy density e_0 as functions of J_2/J_1 (figure 5.3a, 5.3b, and 5.3c). The ground state energy density e_0 smoothly approaches the value of $1/4 - \log(2)$ in one dimension known from the Bethe ansatz. The values we obtained for $\mathcal{M}_s$ agree with earlier results in [60], but have much smaller errors at strong anisotropies. Further, one also clearly observes a decrease of $\mathcal{M}_s$ toward stronger anisotropy in J_2/J_1 which in turn is an indication of the weakening of antiferromagnetism.

5.4 Restoration of the $SU(2)_s$ Spin Symmetry

In the limit $J_2/J_1 \rightarrow 0$, the anisotropic Heisenberg antiferromagnet turns into decoupled spin chains, thus a set of one-dimensional Heisenberg antiferromagnets or Haldane spin chains. In one dimension there is no spontaneous symmetry breaking, thus the $SU(2)_s$ spin symmetry is restored. One could expected this transition to be in the $O(3)$ universality class, because it is a transition between a broken $SU(2)_s$ spin symmetry and the restored full $SU(2)_s$ spin symmetry. However, because there is not just a phase transition, but also a dimensional cross-over this not clear at all.

In the vicinity of the phase transition the low-energy parameters are expected to scale as

$$\frac{\rho_s}{c} \propto \left(\frac{J_2}{J_1}\right)^{\nu}, \quad \mathcal{M}_s \propto \left(\frac{J_2}{J_1}\right)^{\beta}, \tag{5.5}$$

with the universal critical exponents ν and β (β is not to be confused with the inverse temperature). For the 3-d $O(3)$ universality class we know the values

$$\nu = 0.7112(5), \; \beta = 0.3691(3) \tag{5.6}$$

from [68].

In order to perform a good fit one has to be sufficiently close to the transition. Usually for a parameter k with a critical value of k_c one requires

$$\frac{|k - k_c|}{k_c} \ll k_c. \tag{5.7}$$

In our case, the dimensional cross-over respectively the phase transition happens exactly at $J_2/J_1 = 0$. Already for infinitesimal J_2/J_1 the system is two-dimensional with a spontaneous symmetry breaking at zero temperature. Thus a condition such as eq. (5.7) cannot be met and it is not clear how to judge whether one is sufficiently close to the transition.

We think that the data presented above is not sufficiently close to perform a completely reliable fit of ν and β. In order to go to smaller J_2/J_1 one would have to work on much larger lattices, in order to still match the condition of a cubical space-time box. Nevertheless we perform a fit with the available data, for all $J_2/J_1 \leq 0.2$ shown in figure 5.4, and with a conservative error estimate we obtain

$$\nu = 0.47(2), \; \beta = 0.40(2). \tag{5.8}$$

A possible systematic deviation due to not being sufficiently close to $J_2/J_1 = 0$ is not included, because that is very hard to estimate. Interestingly enough, the fitted values

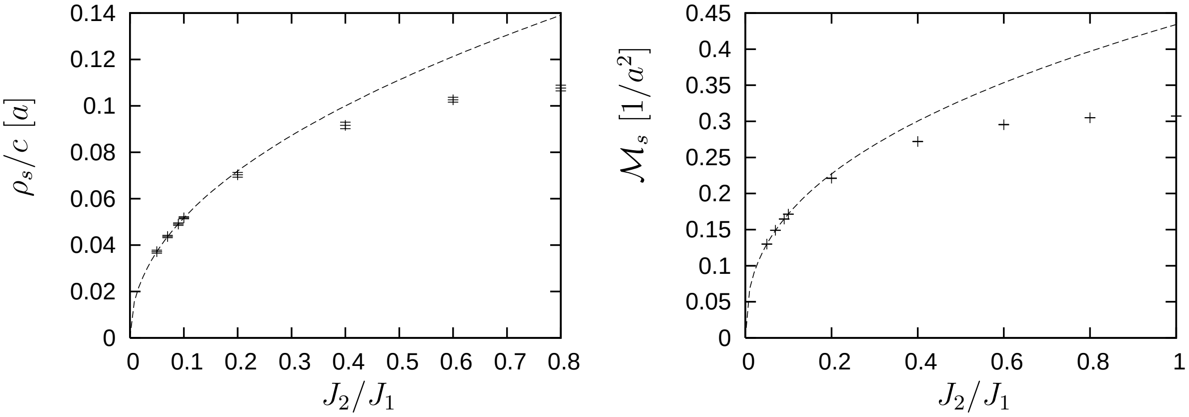

Figure 5.4: *Fits of the scaling parameters ν and β to the low-energy constants ρ_s and $\mathcal{M}_s$.*

deviate significantly from the values of the $O(3)$ universality class. The fit is good with χ^2/d.o.f. < 1.0.

The transition described here could belong to a new universality class. However, in order to make such a statement with certainty one should generate data at much smaller values of J_2/J_1. Such dimensional crossover phenomena seem to be much harder to investigate numerically than one may naively expect.

5.5 Usage of the ALPS Library

While all other codes of the simulations performed in this thesis were written by the author, the simulations in this chapter were performed with the ALPS project (Algorithms and Libraries for Physics Simulations) codes. The ALPS project is an open source effort aiming at providing high-end simulation codes for strongly correlated quantum mechanical systems as well as C++ libraries for simplifying the development of such code [69].

This was very convenient, because it is very easy to simulate a variety spin models on various lattice geometries just by editing some configuration files without any further programming. The codes are open source and can be used by any physicists who do not want to develop and debug their own code and just want to generate physical data.

Codes and tutorials can all be freely downloaded at `http://alps.comp-phys.org`.

Chapter 6

The Heisenberg Antiferromagnet with Additional Four-spin Interaction

It is interesting to consider extensions of the Heisenberg model and observe how the physics changes. One such extension we will consider here. The work presented in this chapter has been published in [9].

6.1 Extended Heisenberg Model

The Heisenberg model can be modified by adding terms to the Hamiltonian. As originally proposed in [35], we consider the Heisenberg Hamiltonian with an additional four-spin coupling Q

$$\begin{aligned} H = J \sum_{x,i} \vec{S}_x \cdot \vec{S}_{x+\hat{i}} - Q \sum_{x} \Big[& (\vec{S}_x \cdot \vec{S}_{x+\hat{1}} - \frac{1}{4})(\vec{S}_{x+\hat{2}} \cdot \vec{S}_{x+\hat{1}+\hat{2}} - \frac{1}{4}) \\ & + (\vec{S}_x \cdot \vec{S}_{x+\hat{2}} - \frac{1}{4})(\vec{S}_{x+\hat{1}} \cdot \vec{S}_{x+\hat{1}+\hat{2}} - \frac{1}{4}) \Big] , \end{aligned} \tag{6.1}$$

thus leading to the so-called J-Q-model.

If Q is large, the antiferromagnetic order will be destroyed which is particularly interesting, because by doping holes into a t-J model (which corresponds to the Heisenberg model at half-filling), antiferromagnetism is also destroyed. Hence, we will investigate the weakening of the antiferromagnet, again using chiral perturbation theory [20, 21].

Furthermore, we will have a close look at the phase transition to the valence bond solid (VBS) phase, which was the reason to propose this model in the first place. It has been claimed that the phase transition is second order, concluding that the transition belongs to a new universality class that is inconsistent with the Ginzburg-Landau-Wilson paradigm. As argued below, we find that the phase transition is weakly first order.

Finally, we will investigate some of the properties of the VBS phase.

The details of the implementation of the loop-cluster algorithm used in this study are explained in appendix A.

6.2 Deconfined Quantum Criticality

A quantum critical point is a phase transition due to quantum fluctuations at zero temperature, separating two competing types of order. A deconfined quantum critical point is a continuous transition from one type of order to an other, i.e. an exotic second order phase transition as argued in [36]. In our special case it is the transition from the antiferromagnetic order that breaks the spin symmetry, to the VBS order that breaks the lattice symmetry. Usually, one would expect a discontinuous jump from one type of order to the other which is thus a first order phase transition. Deconfined quantum criticality is in contradiction to the Ginzburg-Landau-Wilson paradigm, and if it exists, it would open the door to a new class of phase transitions previously unknown.

It has been argued that the discussed transition is related to the deconfinement of spinons, — quasi-particles caused by topological defects — thus the term deconfined quantum criticality.

In the quest for systems where deconfined quantum criticality occurs, the model we study here is one proposition. Although the conclusion of the original work on the J-Q model in [35] is a second order phase transition that confirms deconfined quantum criticality, other work confirms our conclusion of a weak first-order phase transition [70]. Hence, finding deconfined quantum criticality an actual physical system is rather non-trivial. For example, numerical simulations of microscopic models separating a valence bond soldid (VBS) order and a superfluid phase found a weak first order phase transition [71, 72]. In an other a detailed study of an other transition between VBS order and superfluidity has been shown to be first order in [73]. Also a study of a Higgs transition in several three-dimensional lattice realizations of the noncompact $\mathbf{CP}^1$ model claim to show a generic line of second-order Higgs transitions, thus a deconfined quantum critical point [74]. This was also shown to be first order in [75] using the flowgram method [73].

There is newer work that extends the J-Q model with six-spin interactions and extends the symmetry from $SU(2)$ to $SU(N)$, i.e. in particular $SU(3)$ and $SU(4)$ [76]. Their works claims to confirm the observation of deconfined quantum criticality.

6.3 Weakening of Antiferromagnetism

As the additional four-spin interaction Q is increased, antiferromagnetism is weakened. In the antiferromagnetic region of the J-Q-model, low-energy effective field theory can be applied as described in chapter 3. In order to observe the weakening of antiferromagnetism we extract the low-energy parameters as described in section 3.2.

6.3.1 Determination of the Low-Energy Parameters

In practice we have performed simulations for a variety of lattice sizes L/a ranging from 24 to 112 at inverse temperatures between $\beta J = 10$ and 20. Just as the ordinary two-spin coupling J, the four-spin coupling Q can also be treated with an efficient loop-cluster

Q/J	βJ	L/a	$\chi_s Ja$	$\langle W_t^2 \rangle$
0.1	20	34	743.0(1.8)	8.285(26)
0.1	20	36	829(2)	9.312(25)
0.5	16	42	625.1(1.6)	7.561(20)
0.5	16	44	683(2)	8.310(20)
1	12	42	333.7(1.3)	5.361(20)
1	12	46	396.3(1.5)	6.434(22)
2	12	66	470.8(1.6)	5.598(20)
2	12	68	497.7(1.6)	5.960(22)
3	10	78	383.8(1.2)	5.310(21)
3	10	82	420.8(1.2)	5.914(22)
4	10	94	415.9(1.5)	5.011(23)
4	10	96	431.4(1.5)	5.229(26)

Table 6.1: *Some numerical data for the staggered susceptibility and the temporal winding number squared* $\langle W_t^2 \rangle$ *obtained with the loop-cluster algorithm.*

algorithm. All simulations described in this section have been performed with a discrete-time loop algorithm at three different lattice spacings in time, which allows a reliable extrapolation to the continuum limit. Details concerning the algorithm can be found in Appendix A. Some numerical data (extrapolated to the time-continuum limit) are listed in table 6.1. The simultaneous fits to eqs. (3.7) and (3.8), for fixed J and Q, are very good with χ^2/d.o.f ranging from 0.5 to 2.0. Typical fits are shown in figures 6.1. The corresponding results are summarized in table 6.3.1 and illustrated in figures 6.2 and 6.3. A substantial weakening of antiferromagnetism can be observed. In particular, going from $Q = 0$ to $Q = 4J$, the staggered magnetisation $\mathcal{M}_s$ decreases by a factor of about 3, while the correlation length $\xi = c/(2\pi\rho_s)$ increases by a factor of about 5. Interestingly, in units

Q/J	$\mathcal{M}_s a^2$	ρ_s/J	$c/(Ja^2)$	ξ/a
0	0.3074(4)	0.186(4)	1.68(1)	1.44(3)
0.1	0.2909(6)	0.183(6)	1.88(3)	1.64(3)
0.5	0.2383(7)	0.182(6)	2.73(4)	2.39(4)
1	0.1965(7)	0.194(7)	3.90(6)	3.19(5)
2	0.149(1)	0.194(9)	5.98(14)	4.91(12)
3	0.122(1)	0.192(8)	7.97(16)	6.60(14)
4	0.106(1)	0.218(13)	10.50(31)	7.67(26)

Table 6.2: *Results for the low-energy parameters* $\mathcal{M}_s$*,* ρ_s*, and* c *as well as the length scale* $\xi = c/(2\pi\rho_s)$ *obtained from fitting* χ_s *and* χ_u *to the analytic expressions of eqs. (3.7) and (3.8) from the magnon effective theory.*

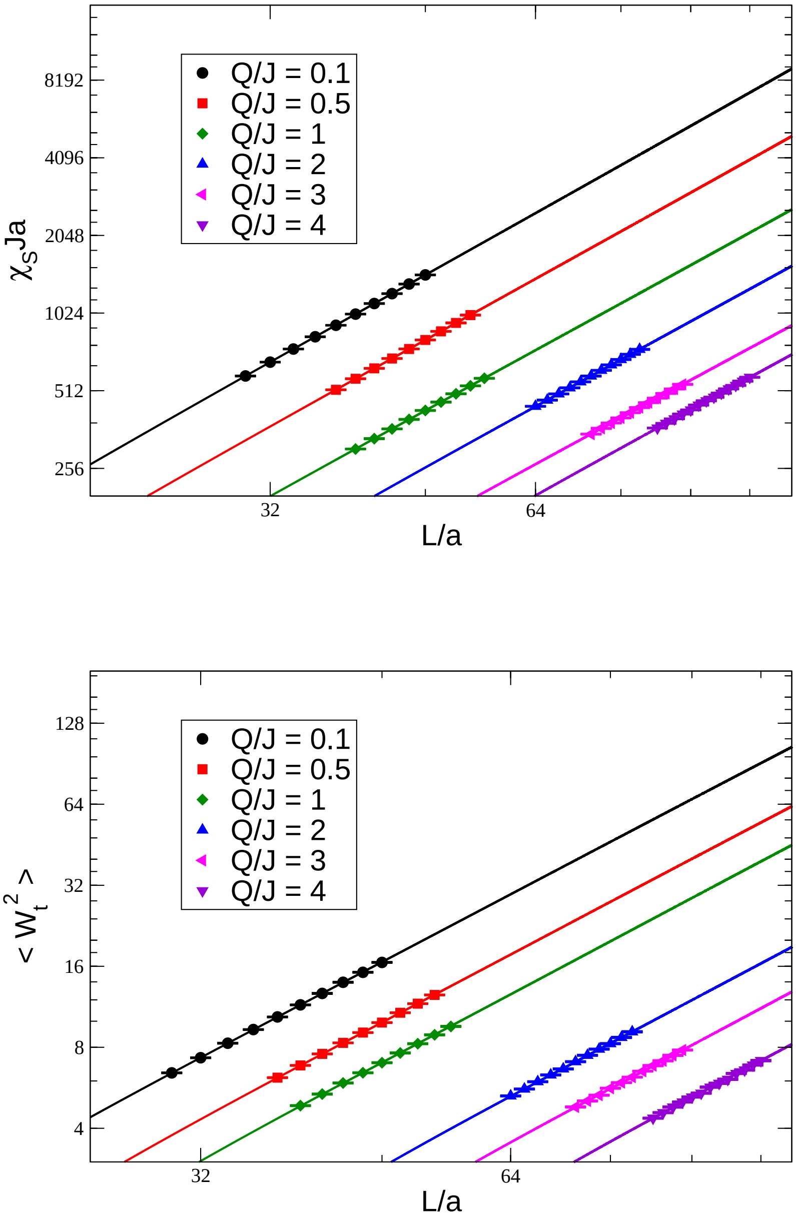

Figure 6.1: *a) Fit of the finite-size and finite-temperature effects of the staggered susceptibility* χ_s *and b) the temporal winding number squared* $\langle W_t^2 \rangle$ *to results of the effective theory in the cubical regime for various values of* Q/J*.*

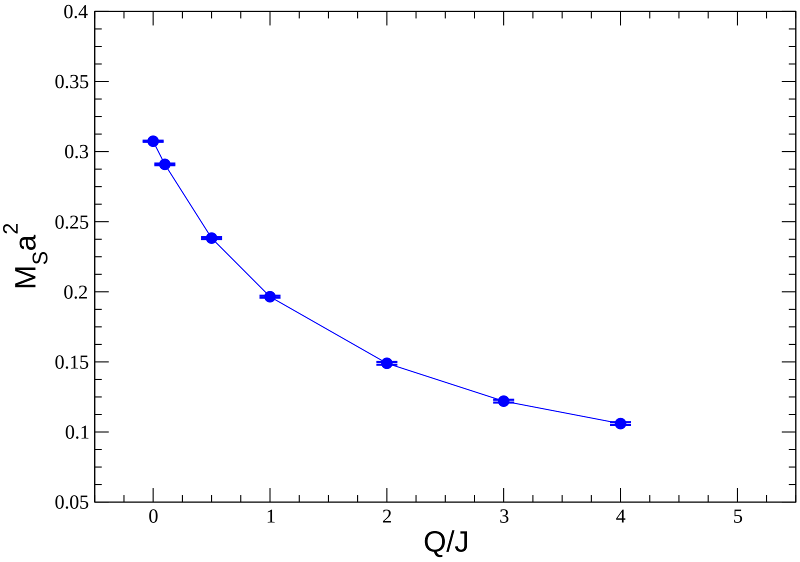

Figure 6.2: *The staggered magnetisation* $\mathcal{M}_s$ *as a function of* Q/J*, obtained from the fits to the magnon effective theory results for* χ_s *and* χ_u*.*

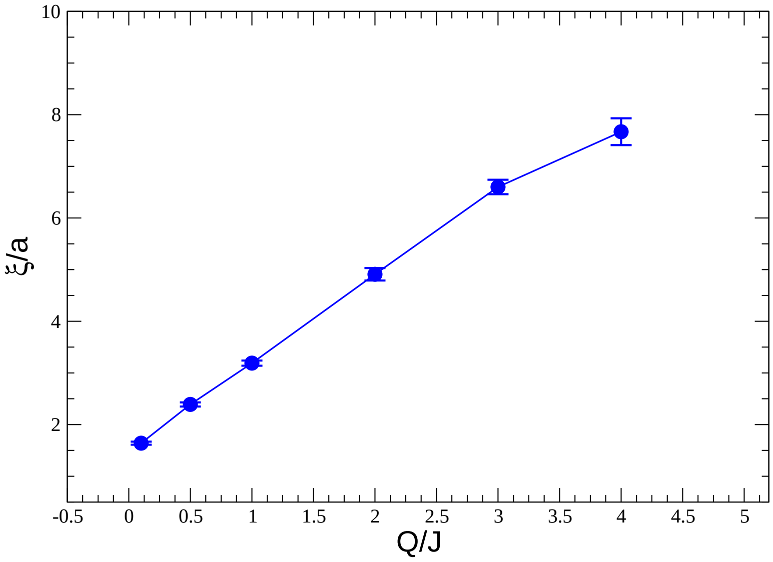

Figure 6.3: *The length scale* $\xi = c/(2\pi\rho_s)$ *as a function of* Q/J*, obtained from the fits to the magnon effective theory results for* χ_s *and* χ_u*.*

of J, the spin stiffness ρ_s is more or less constant. The increase of ξ with Q is thus due to an increase of the spinwave velocity c (in units of Ja). When antiferromagnetism disappears at a second order phase transition, the correlation length ξ diverges. This is possible only if ρ_s goes to zero at the transition. Since the system interacts locally, any excitation travels with a finite speed and hence c cannot go to infinity. If ρ_s stays finite, then this points to a first order phase transition. Further evidence for this type of transition will be presented in the next section.

6.4 Phase Transition between Antiferromagnetism and VBS order

As seen in the previous section, the antiferromagnet is substantially weakened by the four-spin coupling Q. This manifests itself in the decrease of the staggered magnetisation $\mathcal{M}_s$ and the increase of the length scale ξ. The low-energy effective theory is valid as long as the higher order terms are suppressed, which is the case as long as $L \gg \xi$. Because we cannot simulate arbitrarily large lattices, in practice this limits us to $\xi \approx 10a$ which corresponds to $Q/J \approx 5$. The length scale ξ diverges when one approaches a second order phase transition, thus the systematic low-energy effective theory is no longer applicable at such a transition. Different methods are thus needed to investigate the phase transition. In this section we will use both finite-size scaling and the so-called flowgram method [73].

6.4.1 Finite-Size Effects of $\langle W_i^2 \rangle$ near the Transition

In order to find the location of the phase transition, a natural approach is to investigate the J/Q-dependence of the spatial winding number squared $\langle W_i^2 \rangle$. It should also reveal something about the nature of the phase transition, because for sufficiently large volumes the different curves should all intersect at the critical coupling. Such an analysis has been performed in [77] and our Monte Carlo data is consistent with their study. We show a fit to their data for moderate volumes $L/a = 32, 40$, and 48 near the transition using the finite-size scaling ansatz

$$\langle W_i^2 \rangle = f\left(\frac{J - J_c}{J_c} L^{1/\nu}\right) = A + B\frac{J - J_c}{J_c} L^{1/\nu} + \mathcal{O}\left(\left(\frac{J - J_c}{J_c}\right)^2\right) \tag{6.2}$$

in figure 6.4a. It is a good fit with $\chi^2/\text{d.o.f.} \approx 2$ under the assumption that the transition is second order. The three finite volume curves indeed intersect in one point at $J_c/Q = 0.0375(5)$, and no additive sub-leading correction $CL^{-\omega}$ to eq. (6.2) is needed. This is in agreement with the result in [35], which is obtained on smaller volumes $L/a = 16, ..., 32$, which do require the inclusion of a sub-leading term. The fit in that study led to $\omega \approx 2$, implying that the corrections are suppressed for larger volumes.

However, by including the above data at $L/a = 64$ in the fit of eq. (6.2), the quality of fit is worse with $\chi^2/\text{d.o.f.} \approx 8$ as one sees in figure 6.4b. The $L/a = 64$ curve does not pass

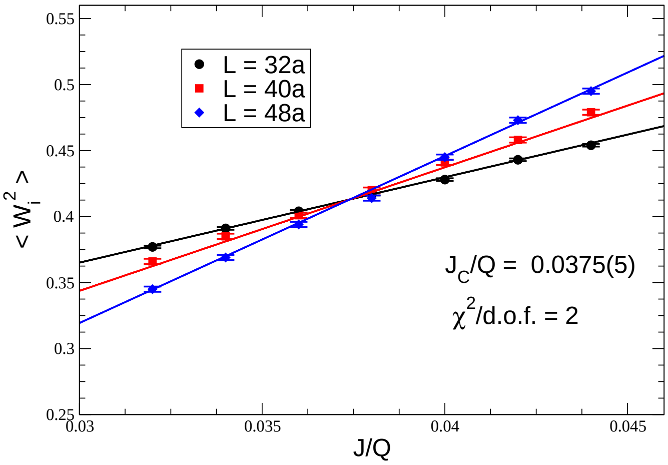

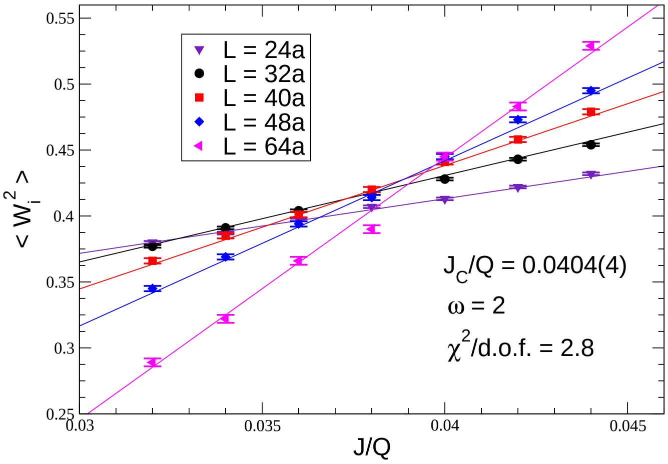

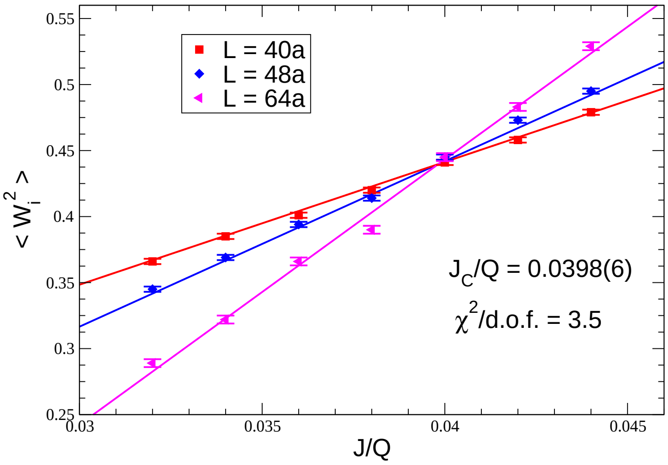

Figure 6.4: *Three different fits of the spatial winding number squared* $\langle W_i^2 \rangle$ *as a function of the coupling* J/Q *in the transition region.*

through the same point as the smaller volume curves. The conclusion of that study is that this should be attributed to sub-leading terms and that there is a quantum critical point somewhere in the interval $0.038 < J/Q < 0.040$. A fit with the inclusion of an additional sub-leading term $CL^{-\omega}$ is possible, but the exponent is not well determined by the data. In order to get a stable fit we fixed ω to various values in the range of $0.01 \leq \omega \leq 2.5$ and got more or less the same quality of fit. However, the value of the critical coupling J_c differs. As an example we fixed $\omega = 2$ as suggested in [35], and as a result we obtain $J_c/Q = 0.0404(4)$ and $\nu = 0.62(2)$, which is illustrated in figure 6.4b. However, by fixing $\omega = 0.01$ we obtain $J_c/Q = 0.0438(7)$ and $\nu = 0.62(2)$.

At last, we consider only the large volumes $L/a = 40, 48$, and 64. Then it is possible again to perform a four-parameter fit, displayed in figure 6.4c. The quality of this fit — with χ^2/d.o.f. ≈ 3.5 is not as good as before and yields $J_c/Q = 0.0398(6)$. In particular, it is inconsistent with the moderate volume data fit. Even larger volume data would be necessary to find out whether the curves will continue to intersect in the same point.

In a nutshell, the data at the moderate volumes $L/a = 32, 40$, and 48 can be fit to eq. (6.2) with a good quality. But once we include $L/a = 64$ a good fit with four parameters can no longer be done. This data can be fit with six parameters using sub-leading corrections. However, since sub-leading terms were not needed to fit the moderate volume data, it is very strange that corrections are needed at larger volumes. We interpret this unusual behaviour as an indication that the phase transition is weakly first order.

A further observation that casts to doubt on the second order nature of the transition is a non-monotonic behaviour of the spatial winding numbers $\langle W_i^2 \rangle$ near the transition, which is shown in figure 6.5. This kind of behaviour is usually seen at a first order phase transition. As an example, in the VBS phase near the transition, antiferromagnetic domains can still exist. For small volumes, domains of the antiferromagnetic phase lead to an increase of $\langle W_i^2 \rangle$ with L, whereas for larger volumes, $\langle W_i^2 \rangle$ will decrease with L because the VBS phase begins to dominate. Such a competition can lead to non-monotonic behaviour. Thus we think that the data in [35] and [77] do not contain sufficient evidence for a second order phase transition and thus for a deconfined quantum critical point. Due to our limited computational power, we could not perform an analysis at substantially larger volumes.

6.4.2 Application of the Flowgram Method

In order to be able to discuss the nature of the phase transition more profoundly, we turn to an alternative method of analysing phase transitions.

The flogram method is useful for distinguishing weakly first order from second order phase transitions [73]. Its idea is to define a volume-dependent pseudo-critical point which ultimately leads to the correct infinite-size critical point. By following observables on the trajectory of the pseudo-critical point, one can make a prediction about the order of the phase transition.

For our system, the flowgram method can be implemented in the following way. We work on lattices of increasing size L at the inverse temperature given by $\beta Q = L/a$. First each individual spin configuration in the path integral is associated with either the anti-

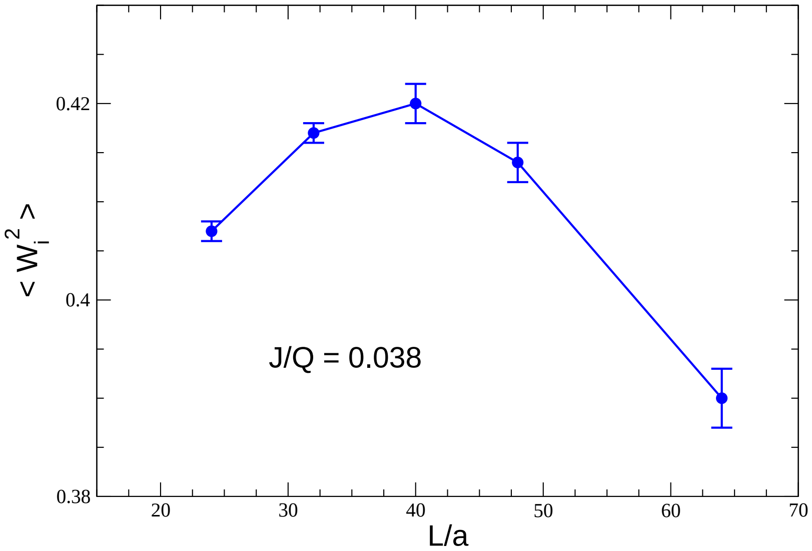

Figure 6.5: *Non-monotonic volume-dependence of* $\langle W_i^2 \rangle$ *at* $J/Q = 0.038$ *near the critical coupling that may indicate a weak first order phase transition.*

ferromagnetic or the VBS phase according to the following criterion. If all three winding numbers W_1, W_2, and W_t are equal to zero, the configuration is associated with the VBS phase and otherwise with the antiferromagnetic phase. This criterion is natural, because in the infinite volume limit there is no winding in the VBS phase, whereas in an antiferromagnet there is always some winding. The volume-dependent pseudo-critical coupling $J_c(L)$ is then defined where both phases have equal weight. In the infinite-volume limit, this pseudo-critical coupling indeed leads to the true location of the phase transition J_c. The large volume limit is now approached by simulating systems at the pseudo-critical coupling $J_c(L)$ for increasing values of L. Using the sum of the spatial and temporal winding numbers squared $W^2 = W_1^2 + W_2^2 + W_t^2$, the quantity $\langle W^2 \rangle (J_c(L))$ is then evaluated at the pseudo-critical coupling $J_c(L)$. If the phase-transition is second order, $\langle W^2 \rangle (J_c(L))$ will approach a constant for large L since ρ_s then vanishes, i.e. $\xi = c/(2\pi\rho_s)$ diverges at the phase transition. On the other hand, if the phase-transition is first order, with 50 percent probability, the system will show the characteristics of the antiferromagnet. Thus, for $L \gg \xi$ the quantity $\langle W^2 \rangle (J_c(L))$ grows linearly with L. As will be shown below, for $48a \leq L$ we indeed observe this behaviour.

We have implemented the Ferrenberg-Swendsen re-weighting method [78] in order to accurately locate the pseudo-critical coupling. Unlike in the rest of this thesis, the simulations in this subsection have only been performed at two (instead of three) lattice spacings in discrete time. Both lattice spacings are close to the continuum limit and give consistent results. Instead of extrapolating to the continuum limit (which is less reliable with two

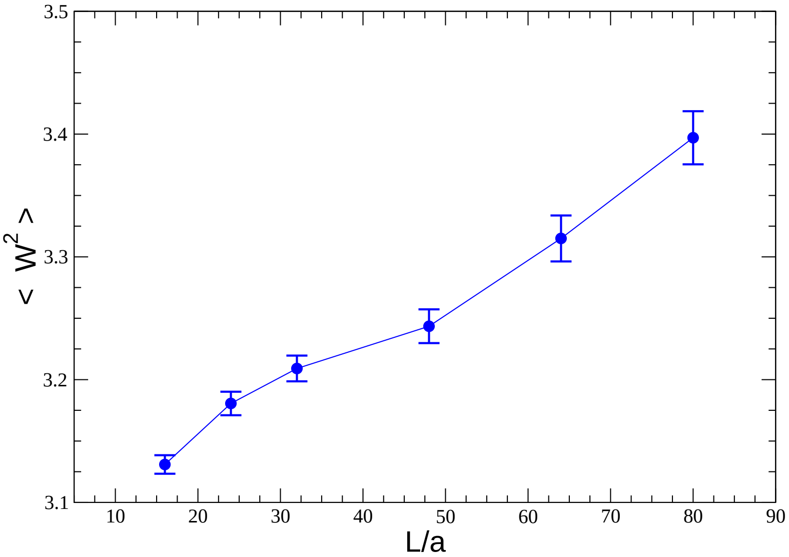

Figure 6.6: *The sum of spatial and temporal winding numbers squared* $\langle W^2 \rangle (J_c(L))$ *evaluated at the pseudo-critical coupling* $J_c(L)$ *for increasing lattice size* L.

than with three lattice spacings), in this subsection we quote our results at the smaller lattice spacing $\varepsilon Q = 0.05$. A calculation using the continuous-time algorithm should not deviate from our results.

The values of $\langle W^2 \rangle$ at the pseudo-critical coupling $J_c(L)$, which we use to determine the order of the phase transition, are shown in figure 6.6. For moderate volumes up to $L = 48a$ the curve seems to level off, which is the characteristic of a second order phase transition. As we have seen before, the moderate volume date for the spatial susceptibility are consistent with the finite-size scaling behaviour of a second order phase transition. However, for larger volumes the curve rises linearly, thus indicating a weak first order phase transition. Of course, still at finite volume, one can never completely rule out that the curve might flatten off at even larger volumes. However, this is rather unlikely and leads to the conclusion that our results cast serious doubt on the picture of deconfined quantum criticality painted in earlier studies of this model.

Based on the conclusion above, we want to determine the value of the critical coupling J_c. The values of the pseudo-critical coupling $J_c(L)$ are shown in table 6.3. It is non-trivial to extract the infinite volume critical coupling $J_c = J_c(\to \infty)$ with the data for $J_c(L)$ alone. For this reason we define another pseudo-critical coupling $J_c'(L)$, which also extrapolates to the correct limit, i.e. $J_c'(L \to \infty) = J_c$. In this case we work at the inverse temperature given by $\beta Q = L/4a$, i.e. in a slab geometry. Irrespective of the spatial winding numbers, if the temporal winding number W_t is zero, the configuration is now associated with the VBS phase and otherwise with the antiferromagnet. As before we again define the volume-

L/a	24	32	48	64	80	96
$J_c(L)/Q$	0.0311(4)	0.0316(3)	0.0337(4)	0.0364(3)	0.0384(3)	—
$J'_c(L)/Q$	0.115(2)	0.0871(4)	0.0632(4)	0.0544(5)	0.0477(4)	0.0445(4)

Table 6.3: *Values of the volume-dependent pseudo-critical couplings $J_c(L)$ and $J'_c(L)$ obtained with the Ferrenberg-Swendsen re-weighting method.*

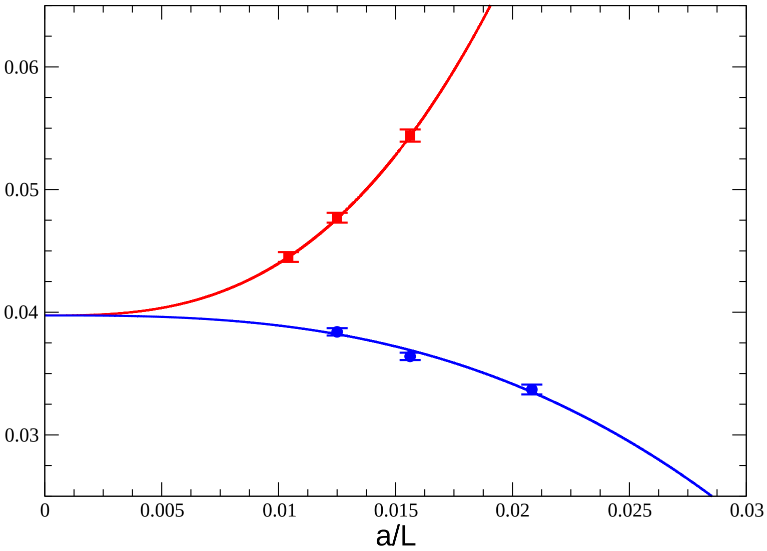

Figure 6.7: *Fit of the pseudo-critical couplings $J_c(L)$ (lower curve) and $J'_c(L)$ (upper curve) shown as functions of a/L.*

dependent pseudo-critical coupling $J'_c(L)$ where both phases have equal weight. The values of $J'_c(L)$ (again quoted at $\varepsilon Q = 0.05$) are also listed in table 6.3. Following finite-size scaling theory for first order phase transitions, using $\beta L^2 \propto L^3$, both finite-volume pseudo-critical couplings should approach their common infinite volume limit J_c as

$$J_c(L) = J_c + C\frac{\log L/a}{L^3}, \ J'_c(L) = J_c + C'\frac{\log L/a}{L^3}. \qquad (6.3)$$

The two pseudo-critical couplings indeed converge to the same limit. The fit of both J_c and J'_c to eq. (6.3), shown in figure 6.7, has χ^2/d.o.f ≈ 1.15 and yields the infinite volume critical coupling $J_c = 0.0396(6)$. It should be noted again that only the large-volume data show the characteristic behaviour of a first order phase transition. The definition of J'_c is less natural than the one of $J_c(L)$, because it ignores the spatial winding when configurations are associated with either of the two phases. This can be seen in the fact that $J'_c(L)$ approaches the infinite-volume critical point in a slower fashion than $J_c(L)$.

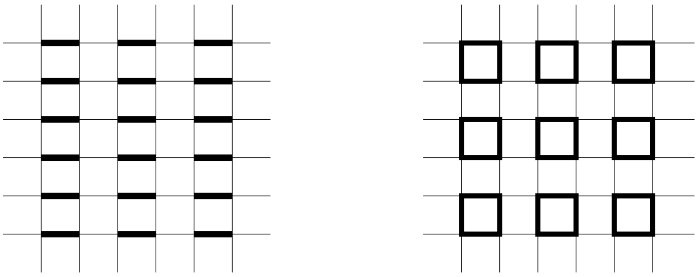

Figure 6.8: *Columnar (a) and plaquette (b) type of VBS order. The solid bonds indicate groups of spins that preferentially form singlets.*

Consequently, the ultimate large-volume physics is more easily visible using the pseudo-critical coupling $J_c(L)$. For example the linear increase of $\langle W^2\rangle(J_c(L))$ with L, as shown in figure 6.6, which sets in around $L \approx 50a$, is not yet present in $\langle W^2\rangle(J_c'(L))$, and is expected to set in only on larger volumes.

6.5 The Valence Bond Solid Phase

As we have seen, with increasing Q the antiferromagnet is ultimately destroyed at a weak first order phase transition. Because the transition is very weak, at small volumes it can hardly be distinguished from a second order transition which gives rise to an approximate $U(1)$ symmetry, dynamically emerging as an enhancement of the 90 degrees rotation symmetry of the square lattice. This emergent $U(1)$ symmetry makes it difficult to identify the nature of the valence bond solid, as described below.

We speak of a valence bond solid (VBS) phase when the $SU(2)_s$ spin symmetry is restored and instead certain lattice symmetries are broken (i.e. translational invariance, rotation symmetry). In the VBS phase spins form singlets with one of their neighbours and are ordered in a certain way. There are two types of VBS order: columnar and plaquette order as shown in figure 6.8.

A natural order parameter that signals a VBS state is

$$D_i = \sum_x (-1)^{x_i/a} \vec{S}_x \cdot \vec{S}_{x+\hat{i}}. \tag{6.4}$$

If either D_1 or D_2 has a non-vanishing expectation value we have evidence for the columnar order. When a linear combination $D_1 \pm D_2$ has a non-zero expectation value we observe plaquette-type VBS order.

In our numerical simulations it is easier to consider an alternative pair of order parameters. We count the number of transitions — i.e. whenever two antiparallel neighbouring spins exchange their position, which we call a flip — in the configurations contributing to

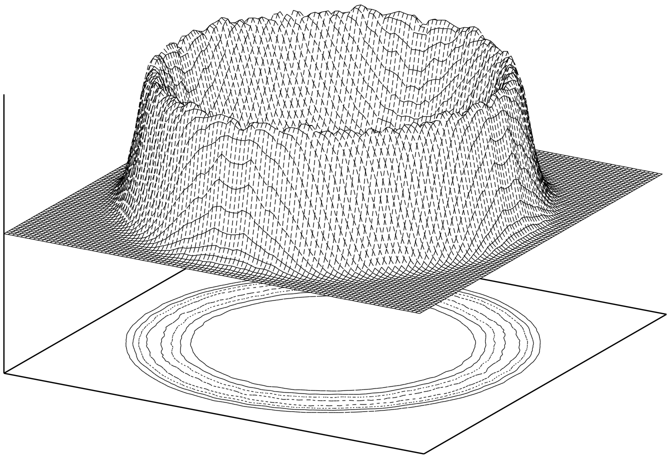

Figure 6.9: *Probability distribution* $p(\widetilde{D}_1, \widetilde{D}_2)$ *obtained on a* 96^2 *lattice at* $\beta Q = 30$ *and* $Q/J = \infty$*. The observed* $U(1)$ *rotation symmetry implies that we cannot identify the nature of the VBS phase as either columnar or plaquette order.*

the path integral. We define the order parameter $\widetilde{D}_i$ as the difference between the number of spin flips on nearest-neighbour bonds in the i-direction with an even and an odd value of x_i/a. It should be noted that such flips can be due to both the standard two-spin coupling of strength J and the four-spin coupling of strength Q. The corresponding probability distribution $p(\widetilde{D}_1, \widetilde{D}_2)$ is thus useful for investigating the nature of the VBS state.

6.6 Probability Distribution of the VBS Order Parameter

In order to investigate the VBS order in the best possible manner, we go as far into the VBS phase as possible. Assuming that no further phase transition takes place we work at $Q/J = \infty$, i.e. we put $J = 0$.

The probability distribution $p(D_1, D_2)$ has been determined by Sandvik on a 32^2 lattice at very low temperature and it shows a perfect $U(1)$ symmetry [35]. Using the loop-cluster algorithm described in appendix A we were able to go to larger lattices, calculating the non-standard VBS order parameter $p(\widetilde{D}_1, \widetilde{D}_2)$ on lattices up to 96^2 at $\beta Q = 30$. We do not see any deviation from the $U(1)$ symmetry and can thus not identify the nature of the VBS order as shown in figure 6.9.

In a recent work, where the interaction is extended with six-spin interactions and the symmetry is extended to $SU(3)$ and $SU(4)$, the transition from the emergent $U(1)$ symmetry at the phase transition to the expected Z_4 symmetry is observed [76].

The loop-cluster algorithm described above is very efficient at small Q/J with very short auto-correlation times, because it is designed to efficiently update long-range spin

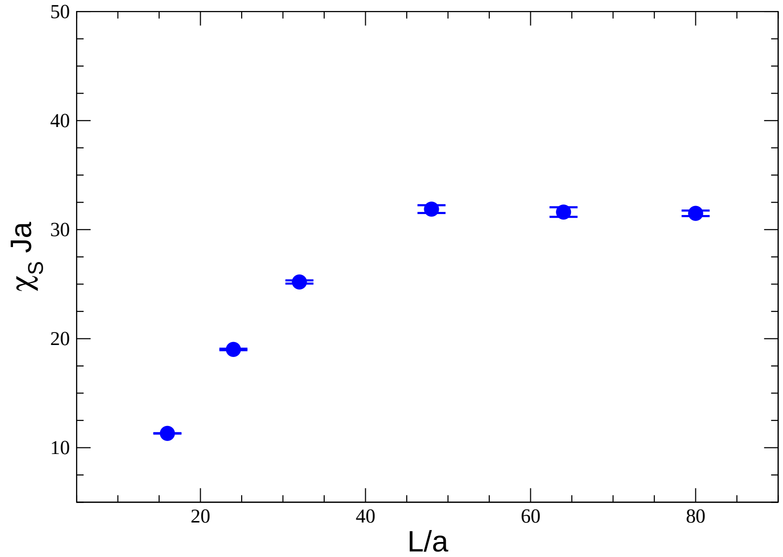

Figure 6.10: *The staggered susceptibility χ_s in the VBS phase increases with increasing space-time volume until it levels off around $L/a \approx 50$ for $\beta Q = 50$.*

correlations, which means that it is ideally fitted to calculate antiferromagnetic physics. However, it is not efficient in shuffling transitions from even to odd bonds and thus it is not perfectly suited for a simulation in the VBS phase.

6.7 Antiferromagnetic Correlations in the VBS phase

In order to show that antiferromagnetism is indeed completely gone in the VBS phase we again set $Q/J = \infty$. As shown in figure 6.10, at $\beta Q = 50$ the staggered susceptibility increases with increasing volume until it levels off at around $L \approx 50a$. This shows that long-, but not infinite-range antiferromagnetic order survives deep in the VBS phase, but that antiferromagnetism is indeed destroyed. Again, our calculation shows that it would be desirable to go to even bigger lattices to unambiguously identify the ultimate infinite-volume behaviour.

Part I

Numerical Simulations of the Heisenberg Model on Frustrated Lattices

Chapter 7

Candidate Ground States on Frustrated Lattices

The ground states of multi-particle quantum systems ground states are often not known analytically. For example, in order to extract the ground state of a Heisenberg antiferromagnet on a large lattice, one would have to diagonalise a matrix of size $2^N \times 2^N$, where N is the number of sites. This is practically impossible. Thus making reliable statements about the ground state is a rather non-trivial task.

7.1 Antiferromagnet on a Square Lattice

As the square lattice is a bipartite lattice, the classical ground state is the classical Néel order as already mentioned in chapter 1. The classical Néel state is realised when all spins on sublattice A point in one direction and all spins on sublattice B point exactly in the opposite direction. In the case of the classical Heisenberg antiferromagnet the spins on the sublattice A point in the direction $\vec{e}$ and all spins on the sublattice B point in the direction $-\vec{e}$.

However, in the quantum Heisenberg antiferromagnet, the classical Néel state is no energy eigenstate. It is know from numerical simulations that even a spin $\frac{1}{2}$ Heisenberg antiferromagnet, where quantum fluctuations are strongest, has a second order phase transition at zero temperature, where the system shows long-range antiferromagnetic order [47].

7.2 Candidate Ground State on a Triangular Lattice

In contrast to bipartite lattices, the triangular lattice cannot be divided into two, but three sublattices A, B, and C as shown in figure 7.1.

On a triangular lattice antiferromagnetism is frustrated, because it is not possible to realise a state, where the spins on all pairs of neighbouring sites are antiparallel. For a classical antiferromagnet the ground state shows coplanar order, as it is illustrated in figure

7.1, where nearest-neighbour spins enclose an angle of 120 degrees also called 120 ° Néel order.

In the case of the quantum Heisenberg antiferromagnet one still expects coplanar ordering as there is some evidence for this from quantum Monte Carlo and exact diagonalisation [79].

7.2.1 Coplanar Order Parameter

In order to detect antiferromagnetic order on a bipartite lattice, we measure the staggered susceptibility χ_s which is proportional to the average of the square of the staggered magnetisation

$$\vec{M}_s = \sum_x \vec{S}_x (-1)^{l_x} = \sum_x \vec{S}_x e^{2\pi i \frac{l_x}{2}} \quad l_x = 0 \text{ for all } x \in A, \quad l_x = 1 \text{ for all } x \in B. \tag{7.1}$$

In the same way we define a coplanar magnetisation

$$\widetilde{\vec{M}}_c = \sum_x \vec{S}_x e^{2\pi i \frac{l_x}{3}}, \quad l_x = 0 \text{ for all } x \in A, \quad l_x = 1 \text{ for all } x \in B, \quad l_x = 2 \text{ for all } x \in C. \tag{7.2}$$

Because $\widetilde{\vec{M}}_c$ is complex we can individually look at the real part

$$\Re\left(\widetilde{M}_c^3\right) = M_A - \frac{1}{2} M_B - \frac{1}{2} M_C \tag{7.3}$$

and the imaginary part of the three-component of the coplanar magnetisation

$$\Im\left(\widetilde{M}_c^3\right) = \frac{\sqrt{3}}{2} M_B - \frac{\sqrt{3}}{2} M_C, \tag{7.4}$$

where M_A, M_B, and M_C are the three-components of the magnetisations of the sublattices A, B, and C. It is convenient to use the imaginary part of the coplanar magnetisation to redefine the coplanar magnetisation as

$$M_c \doteq M_B - M_C, \tag{7.5}$$

which is what we are going to measure in the simulations. Using the improved estimator of the cluster algorithm in the continuous-time path integral picture, we define the coplanar susceptibility as

$$\chi_c = \frac{1}{\beta \frac{2}{3} V} \left\langle \left(M_B^{\mathcal{C}} - M_C^{\mathcal{C}}\right)^2 \right\rangle, \tag{7.6}$$

where V is the number of spins. The factor of $\frac{2}{3}$ arises because we consider only two of the three sublattices. By symmetry considerations it is obvious that the sublattices can be exchanged and thus

$$\chi_c = \frac{1}{\beta \frac{2}{3} V} \left\langle \left(M_B^{\mathcal{C}} - M_C^{\mathcal{C}}\right)^2 \right\rangle = \frac{1}{\beta \frac{2}{3} V} \left\langle \left(M_A^{\mathcal{C}} - M_B^{\mathcal{C}}\right)^2 \right\rangle = \frac{1}{\beta \frac{2}{3} V} \left\langle \left(M_A^{\mathcal{C}} - M_C^{\mathcal{C}}\right)^2 . \right\rangle \tag{7.7}$$

7.3 Frustrated Square Lattice

By introducing a diagonal coupling J' to the usual coupling $J = J_{xy}$ (the coupling in the x- and y-directions) in the Hamiltonian

$$H = J_{xy} \sum_{x,\hat{\mu}} \vec{S}_x \cdot \vec{S}_{x+\hat{\mu}} + J' \sum_{x} \vec{S}_x \cdot \vec{S}_{x+\hat{1}+\hat{2}}, \tag{7.8}$$

antiferromagnetism is also frustrated. One can now continuously interpolate between a square lattice and a triangular lattice with $0 \leq J'/J_{xy} \leq 1$. In the limit $J' = 0$ it corresponds to the square lattice and antiferromagnetism is not frustrated. In the limit $J' = J_{xy}$ the system is fully frustrated and corresponds to the triangular lattice. These two limits with their corresponding sublattices are shown in figure 7.2. One can also consider the limit $J_{xy} = 0$ which corresponds to decoupled spin chains.

7.4 Candidate Ground State on a Kagomé Lattice

On the kagomé lattice it is also possible to identify three sublattices A, B, and C. However, other than in the case of the triangular lattice this is not unambiguous. On the hexagons or on any other closed curve containing only two of the three sublattices, as shown in figure 7.3, one can exchange the sublattice classification and one still has a valid choice of sublattices. If one now puts a coplanar state on these sublattices, it is obvious that such a classical ground state is highly degenerate. This is why some experts expect a spin liquid, i.e. no spontaneous symmetry breaking, on the kagomé lattice [37, 38].

A spin liquid is a system where no ordering takes place. There is no spontaneous symmetry breaking of either the internal $SU(2)_s$ spin symmetry of of a lattice symmetry, not even at zero temperature.

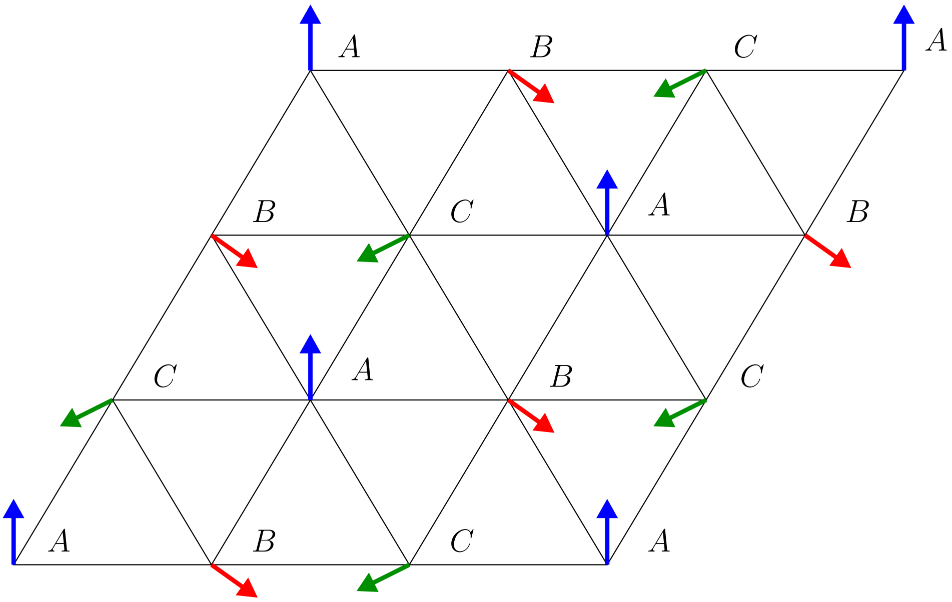
A
B
C
A
B
C
A
B
C
A
B
C
A
B
C
A

Figure 7.1: *Triangular lattice with coplanar order. The arrows show the coplanar order of the spins that enclose 120 degree angles with their neighbours in the internal spin space. Also the three sublattices are denoted with* A*,* B*, and* C*.*

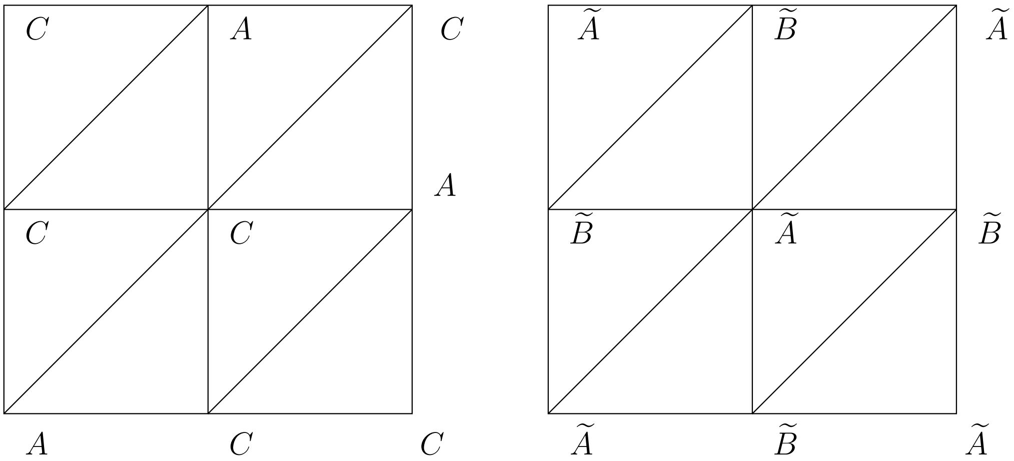
C
A
C
A
C
C
A
C
C
$\widetilde{A}$
$\widetilde{B}$
$\widetilde{A}$
$\widetilde{B}$
$\widetilde{A}$
$\widetilde{B}$
$\widetilde{A}$
$\widetilde{B}$
$\widetilde{A}$

Figure 7.2: *The frustrated square lattice It corresponds to a triangular lattice with* $J_{xy} = J'$ *and a square lattice with* $J' = 0$*. The different sublattices are used to define the corresponding susceptibilities* χ_s *and* χ_c *which are sensitive to antiferromagnetic and coplanar order.*

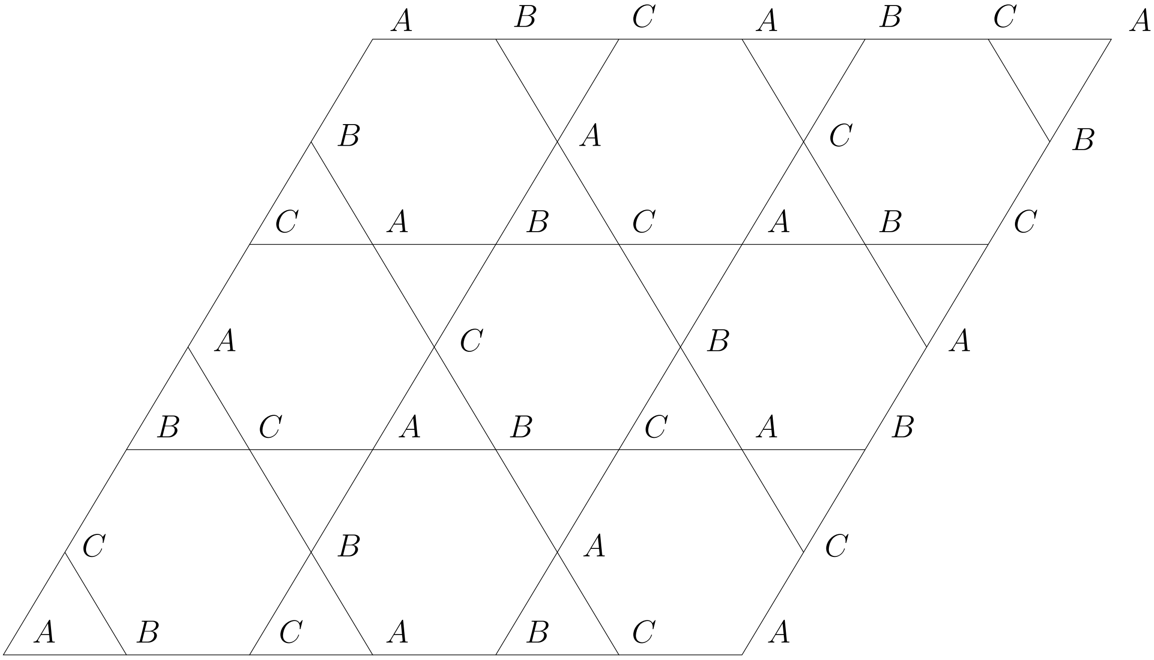
A
B
C
A
B
C
A
B
A
C
B
C
A
B
C
A
B
C
A
C
B
A
B
C
A
B
C
A
B
C
B
A
C
A
B
C
A
B
C
A

Figure 7.3: *Kagomé lattice with one choice of three sublattices A, B, C. In contrast to the triangular lattice there is a large ambiguity in the choice of the sublattices.*

Chapter 8

Nested Cluster Algorithm

First principles quantum Monte Carlo simulations on frustrated spin systems are very hard to perform and suffer especially from the sign problem which we will discuss below. In this chapter we present a new method, that does not solve the problem completely, but pushes the possible calculable system sizes quite a bit further and also gives us some insight into the nature of such systems and their computational challenges. The work presented in this chapter has been published in [40].

8.1 The Sign Problem

The Monte Carlo method is based on the idea of interpreting the Boltzmann weight $\exp(-S[s])$ of a configuration $[s]$ as a probability

$$p[s] = \frac{1}{Z}\exp(-S[s]). \tag{8.1}$$

With this idea in mind, one can generate a Markov chain, as discussed in chapter 2, i.e. a set of configurations $[s]$, sampled according to their probabilities $p[s]$

$$[s^{(1)}] \to [s^{(2)}] \to \cdots \to [s^{(N)}]. \tag{8.2}$$

With such a set of configurations, generated by a Monte Carlo algorithm one can calculate observables as

$$\langle \mathcal{O} \rangle = \frac{1}{Z}\sum_{[s]} \mathcal{O}[s]\exp(-S[s]) = \lim_{N\to\infty}\frac{1}{N}\sum_{i=1}^{N}\mathcal{O}[s^{(i)}], \tag{8.3}$$

where the configuration $[s]$ appears in the mean according to its Boltzmann weight. In this way most of the time one generates the important configurations, i.e. those with large Boltzmann weight. Hence, this method is known as importance sampling.

The whole scheme, of course, only works for positive $\exp(-S[s])$. In a classical model this is always the case. However, in a quantum system there can be negative or even complex contributions to the partition function (which is still positive), because we now sample a path integral which may have contributions from in general complex transition amplitudes. Of course, if one was in an energy eigenstate basis, the Boltzmann weights $\exp(-\beta E_i)$ would be positive. However, if we knew the energy eigenstates, then we would not need to sample a path integral in the first place. Thus for quantum systems interpreting Boltzmann weights as probabilities often fails.

This problem can be circumvented by interpreting the sign as an observable in a modified partition function

$$Z_+ = \sum_{[s]} |\exp(-S[s])|. \tag{8.4}$$

Observables with respect to Z_+ are related to the observables in the original partition function Z as

$$\langle \mathcal{O} \rangle = \frac{\langle \mathcal{O}\mathrm{Sign}\rangle_+}{\langle \mathrm{Sign}\rangle_+}, \tag{8.5}$$

with

$$\langle \mathrm{Sign}\rangle_+ = \frac{1}{Z_+}\sum_{[s]} \mathrm{Sign}[s]|\exp(-S[s])| = \frac{Z}{Z_+} \sim \exp(-\Delta f \beta V) \tag{8.6}$$

and $\mathrm{Sign}[s] = \mathrm{sign}(\exp(-S[s]))$. Here V is the spatial volume and Δf is the difference of the free energy densities of the original ensemble Z and the simulated ensemble Z_+. The expectation value of the sign is exponentially small in the space-time volume βV. We can estimate the statistical error of the average sign in an ideal simulation which generates N statistically independent configurations as

$$\frac{\sigma_{\mathrm{Sign}}}{\langle \mathrm{Sign}\rangle} = \frac{\sqrt{\langle \mathrm{Sign}^2\rangle - \langle \mathrm{Sign}\rangle^2}}{\sqrt{N-1}\langle \mathrm{Sign}\rangle} \cong \frac{\exp(\Delta f \beta V)}{\sqrt{N-1}}. \tag{8.7}$$

Here we have used $\mathrm{Sign}^2 = 1$. In order to estimate the average $\langle \mathrm{Sign}\rangle$ with sufficient accuracy, one needs on the order of $N = \exp(2\Delta f \beta V)$ measurements [80]. For large space-time volumes this is practically impossible.

8.1.1 NP-Completeness

The advantage of Monte Carlo simulations is that thermal averages can be computed in a time that scales polynomially with the particle number N, although the configuration space grows exponentially with N (of course, this is only valid if the autocorrelation time also only grows polynomially with N). However, as soon as a sign problem arises, i.e. when negative Boltzmann weights are present, the statistical error grows exponentially with N and thus defeats the advantage of the Monte Carlo method.

In [27] it was shown, that the calculation of thermal averages of particular quantum statistical system with Monte Carlo is **NP**-hard. Thus discussing the theory of the **NP** (non-deterministic polynomial) complexity class provides us with with some insight on the chances of solving the sign problem.

A non-deterministic polynomial (**NP**)-complete decision problem could be solved in polynomial time on a hypothetical non-deterministic Turing machine for which no polynomial algorithm is known on a classical deterministic Turing machine (i.e. a common computer). In contrast to a deterministic Turing machine, the hypothetical non-deterministic computer has a set of rules that prescribes more than one action for a given situation, e.g. in case of an if-statement it could follow both branches, but without merging them again. This is equivalent to having exponentially many deterministic Turing machines without any communication in between.

When a problem is **NP**-hard, any problem in **NP** can be mapped onto it with polynomial complexity. Thus, if one can solve a **NP**-hard problem in polynomial time then any problem in **NP** could be solved in polynomial time, which would imply **NP**=**P**. As there has not been found any polynomial time solution for any **NP**-complete problem, it is generally believed that **NP**≠**P**. However, since there is no theoretical proof yet this remains an open question and is one of the millennium problems of mathematics for which the Clay Mathematics Institute has offered a one million dollar prize [81].

Thus, if **NP**≠**P** as it is generally believed, there cannot exist a general polynomial time solution to the sign problem. Still there are solutions to the sign problem for specific systems, but this must be due to the physics of these specific quantum systems which can be described in an essentially bosonic way [27]. One such solution is the meron-cluster algorithm.

8.2 Meron-Cluster Algorithm

The meron-cluster algorithms solves the sign problem e.g. for spinless fermions, a modified Hubbard model, as well as the the 2d $O(3)$ model at non-zero Θ-vacuum angle or chemical potential [39, 80, 82, 83].

In a nutshell, using the meron-concept one rewrites the partition function in terms of clusters in a way that the sign factorises to the clusters. The clusters then are either merons, i.e. they change the sign under a spin flip, or non-merons, i.e. they leave the sign unchanged. By ensuring that only non-merons are generated and are always positive one can sample the partition function without any negative contribution to the partition function. Thus if the meron-concept is applicable, the sign problem for such a system is solved.

This approach solves the problem in two steps. The first step consists of analytically rewriting the partition function, using new variables such that it is possible to exactly cancel all negative weight configurations with configurations of positive weights. This group of configurations then does not contribute to the partition function. The remaining configurations are guaranteed to be positive.

Thus, with the new variables, one effectively obtains Boltzmann weights with $\text{Sign} = 0, 1$. At this stage, despite the fact that all negative signs have been eliminated, only one half of the sign problem has been solved since an algorithm that naively generates configurations with $\text{Sign} = 0$ or 1 generates an exponentially large number of zero weight configurations.

Thus, it is important to introduce a second step in which one avoids configurations that have been cancelled analytically. In practice it is often useful to allow these zero-weight configurations to occur in a controlled manner since these configurations may contribute to some observables such as n-point functions. In a numerical algorithm a local Metropolis decision ensures that contributions of 0 and 1 occur with similar probabilities.

In practice it is not possible to construct a meron-cluster algorithm unless two conditions are satisfied. First, it was never possible to construct such an algorithm — or at least not one that is efficient — without a reference configuration as discussed in chapter 2, which can always be reached from any configuration within one step. Second, it must be possible to factorise the sign to the clusters which will either have a positive sign or change it under cluster flip. Thus the clusters have to be independent.

These are rather strong conditions which could be satisfied for some specific models as mentioned above, but the meron-concept cannot be generally applied.

8.2.1 Fermionic Sign Problem

The fermion sign problem arises from the interchange of indistinguishable fermions in the path integral which gives rise to a negative sign. This sign can be calculated by examining the world-lines of the fermions in the path integral and calculating the permutation sign of the configuration. The fermion permutation sign is a global feature of a configuration. This is in general a problem, because sign-changes cannot be calculated locally. In some cases the sign can be associated to clusters using the meron-cluster algorithm [82].

8.2.2 Sign Problem for Frustrated Lattice Geometries

In a ferromagnetic system, the classical ground state is an eigenstate of the quantum system no matter on what geometry it is applied. For antiferromagnets, the classical ground state is no energy eigenstate of the quantum spin systems. However, on bipartite systems such as the square or the honeycomb lattice, there is still long-range antiferromagnetic order, that can be used as a reference configuration on which a cluster algorithm can be based upon. This reference configuration can be reached from any configuration within one cluster update. Furthermore, the bipartite geometry guarantees that no sign problem arises.

On a non-bipartite lattice, i.e. for frustrated antiferromagnets, even the classical ground state is often not known analytically, or at least provides serious algorithmic problems already at the classical level.

A triangular lattice can be divided into three separate sublattices as shown in chapter 7. Ignoring one of the three sublattices, the spins on the other other two can align antiparallely, but it is never possible to antiparallely align all neighbouring spins with an antiferromagnetic coupling between all three sublattices.

In case of an antiferromagnet, where the transfer matrix takes the form shown in eq. (2.6), the off-diagonal entries are negative. On a bipartite lattice there can only be an even number of such transitions, i.e. neighbouring up- and down-spins that exchange their position. However, on frustrated geometries, there can be an odd number of spin flips, resulting in a configuration with a negative sign. This is shown in figure 8.1, where a single up-spin hops around a triangle in a background of down-spins.

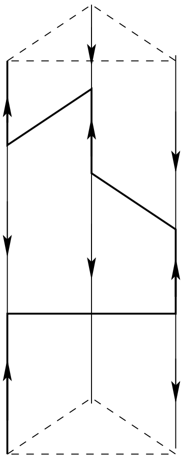

Figure 8.1: *An up-spin on a triangular lattice hops around an elementary triangle in a background of down-spins, generating three transitions which gives rise to a negative sign.*

8.3 Nested Cluster Algorithm

The idea behind the nested cluster algorithm is to perform inner Monte Carlo simulations within outer Monte Carlo simulation. In the algorithm discussed below, the clusters are independent, but we cannot use a meron-cluster algorithm. The clusters do not change sign under cluster flip and non-meron clusters can be negative because there is no reference configuration. Thus we perform in one step a global Monte Carlo update on a configuration and in a second step independently perform Monte Carlo updates on each cluster in a configuration which we call inner Monte Carlo. Why this is possible and how it improves the measurements will be discussed in this section.

The nested cluster algorithm does not completely solve the sign problem for frustrated antiferromagnets, but it improves the numerical estimates of the sign and thus the calculation of observables in such systems. Especially for large volumes at moderate temperatures, simulations can now be performed that were previously impossible. The algorithm is generally applicable to frustrated quantum spin systems irrespective of the specific underlying geometry.

While previously the number of updates should be proportional to $\exp(2\Delta f \beta V)$, now only a number of updates proportional to $\exp(2\Delta f |\mathcal{C}_{\text{max}}|)$ is sufficient. In other words, the sign problem, previously exponentially bad in the space-time volume, is brought down to the size of the largest cluster $|\mathcal{C}_{\text{max}}|$ in the system. The cluster size $|\mathcal{C}|$ can be interpreted as some correlation length. The usual spin-spin correlation length is smaller than these clusters. We think that the cluster size has a physical meaning which is probably a measure of quantum entanglement. The above mentioned improvement of the measurement of the sign makes sense, because the sign problem in a system larger than the correlation length should not get worse. However, as suspected, as the correlation length increases with the inverse temperature β the algorithm becomes less efficient and ultimately the improvement of the nested algorithm is lost with growing cluster size.

8.3.1 Making the Cluster Algorithm Ergodic

Using the standard antiferromagnetic loop-cluster algorithm described in chapter 2, one faces the problem that the algorithm is no longer ergodic. The system is either in a positive or negative configuration and the standard loop algorithm does not move between them. This problem could be solved by using the worm or directed loop algorithm [84–86]. However, the worm or directed loop algorithm, unlike the nested algorithm, does not improve the measurement of the sign.

When we developed the nested cluster algorithm, we first performed an analytic calculation, using a basis change and some further steps explained in detail in appendix B. These steps involve interesting thoughts, worth considering, but are not necessary to explain how the algorithm works.

The first step towards the nested cluster algorithm is to integrate out the spins on a given cluster configuration. There is a second approach to this problem discussed in 8.3.4. Every cluster has two orientations and thus a cluster configuration $[\mathcal{C}]$ represents $2^{N[\mathcal{C}]}$ configurations. Considering all these possibilities at once, one can assign a factor of 2 to each cluster and one then obtains a representation of the partition function, completely expressed in terms of clusters instead of spins

$$Z = \sum_{[\mathcal{C}]} 2^{N[\mathcal{C}]} A^{N_A} B^{N_B}. \tag{8.8}$$

Here A and B are the weights of the two break-ups from figure 2.2 and $[\mathcal{C}]$ are the cluster configurations. Because there is no concrete spin-configuration any more, the break-ups A and B can now always be proposed. Going from a configuration $[\mathcal{C}]$ to $[\mathcal{C}]'$, the Metropolis accept-reject probabilities are given by

$$p_{[\mathcal{C}]\to[\mathcal{C}']} = \min\left\{1, \frac{2^{N[\mathcal{C}']} A^{N'_A} B^{N'_B}}{2^{N[\mathcal{C}]} A^{N_A} B^{N_B}}\right\}. \tag{8.9}$$

These updates can now change the sign and efficiently update the whole partition function. Such updates are shown in figure 8.2.

These changes of plaquettes and thus the cluster configuration are of three types, as can be seen in figure 8.2:

1. The two bonds belong to different clusters $\mathcal{C}_1$ and $\mathcal{C}_2$ and will belong to the same cluster $\mathcal{C}$ afterwards (figure 8.2a).

2. The two bonds belong to the same cluster $\mathcal{C}$ and will be in two different clusters $\mathcal{C}_1$ and $\mathcal{C}_2$ afterwards (figure 8.2b).

3. The two bonds belong to the same cluster $\mathcal{C}$ and will remain in the same cluster (figure 8.2c). This only happens when the two bonds of the cluster have a parallel orientation as shown with the arrow in the picture below. We call such rewirings of clusters internal updates, which we will explore further below.

Only the third type of change of the configuration will change the sign as shown further below.

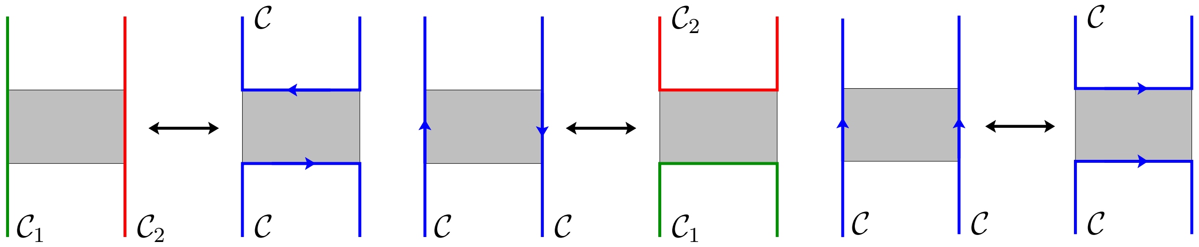

Figure 8.2: *Three types of rewiring clusters, where* $\mathcal{C}_1$ *and* $\mathcal{C}_2$ *are two independent clusters and* $\mathcal{C}$ *is one single cluster. In case of two lines within the same cluster, they have a certain orientation (which could also be inverted) denoted by the arrows.*

8.3.2 Factorisation of the Sign

Transition plaquettes carry a negative sign. This sign can be distributed onto the two bonds of the break-up in the following independent way. We assign to a cluster an orientation by following it one way around. This is equivalent to decorating the cluster with spins. Of course, the clusters can have two orientations. However, as the sign does not change under cluster-flip, one of the two orientations can be chosen arbitrarily. Transition plaquettes are those where both bonds point in the same direction. We then assign a factor of i to sideways bonds travelling in one direction, and we assign a factor of -1 to bonds travelling in the opposite direction as shown in figure 8.3. In this way the correct factors of $+1$ and -1 are reproduced. Under cluster-flip, the orientations change and thus i-factors turn into factors of $-i$ and vice versa. In this way the sign of a configuration factorises over the clusters

$$\text{Sign} = \prod_i \text{Sign}[\mathcal{C}_i]. \tag{8.10}$$

Now it is obvious that the clusters do not change sign under cluster flip, because they must contain an even number of sideways bonds in order to close and thus their sign is ±1. Now the cluster flip turns i into $-i$ and vice versa and thus the overall sign of the cluster remains.

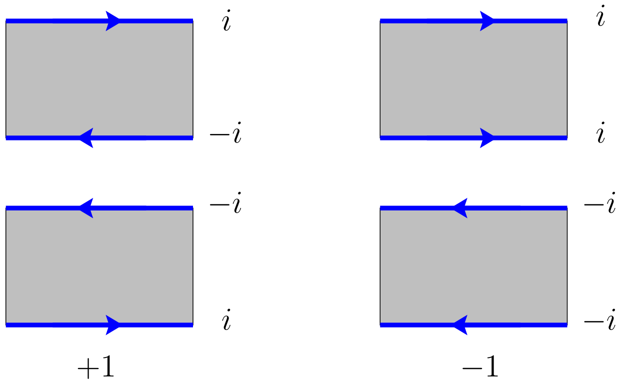

Figure 8.3: *Factorisation of the sign into two i-factors. When bonds are antiparallel, the resulting factor is* $+1$ *and otherwise* -1.

The internal update shown in figure 8.2c changes the sign of a cluster from $+1$ to -1 and the other way around. By this update, half of the cluster changes its orientation. Because each half must contain an even number of sideways bonds on such internal plaquettes that rewiring does not change the sign. However, the introduction or removal of a new transition plaquette changes the sign of the cluster.

The assigned orientations discussed above are there whether we explicitly assign them or not. However, as they help us to determine whether an internal update can be performed, we can either store and update them or measure them within the algorithm.

8.3.3 Improved Measurement of the Sign and the Staggered Susceptibility

After the updates shown in figure 8.2 have been performed we perform an inner Monte Carlo sampling by updating only cluster-internal plaquettes, i.e. internal plaquettes where the bonds travel in the same direction. Each cluster $\mathcal{C}$ defines a set $\Lambda_{\mathcal{C}}$ of sites in space-time contained in the cluster. The inner Monte Carlo procedure generates different realisations of clusters, that visit all sites in $\Lambda_{\mathcal{C}}$ in different orders with different orientations of the bonds. These different realisations contribute different values of $\mathrm{Sign}_{\mathcal{C}}$. In this process, break-up proposals that lead to a decomposition of $\Lambda_{\mathcal{C}}$ into separate clusters must be rejected. Thus only rewirings of type 3, as described in subsection 8.3.1, can be applied. The inner Monte Carlo procedure estimates an average $\langle \mathrm{Sign}_{\mathcal{C}} \rangle_i$ for each set of sites $\Lambda_{\mathcal{C}}$. Here, i denotes the improved estimates performed using the inner Monte Carlo updates. Since the different sets are independent, the improved estimator of the sign is given by

$$\langle \mathrm{Sign} \rangle_i = \prod_{\Lambda_{\mathcal{C}}} \langle \mathrm{Sign}_{\mathcal{C}} \rangle_i. \tag{8.11}$$

The nesting of such an inner Monte Carlo procedure in the outer Monte Carlo update described in subsection 8.3.1 achieves exponential error reduction at polynomial cost.

The number of internal updates has to be fixed for a certain $\Lambda_{\mathcal{C}}$. For example one can choose a function of the cluster size $|\mathcal{C}|$ to determine the number of internal updates. This requires some fine-tuning in order to get maximum efficiency which we will further discuss in section 8.5.

A similar strategy was very successfully applied to the measurement of exponentially suppressed Wilson loops in lattice gauge theory [87] as well as to quantum impurity models [88].

Correlation functions and susceptibilities can also be measured with improved estimators. The staggered susceptibility

$$\chi_s = \frac{\langle M_s^2 \mathrm{Sign}\rangle_+}{\beta V \langle \mathrm{Sign}\rangle_+} = \frac{\langle\langle M_s^2 \mathrm{Sign}\rangle_i\rangle_+}{\beta V \langle\langle \mathrm{Sign}\rangle_i\rangle_+}. \tag{8.12}$$

is obtained from an improved estimator which is given in terms of the clusters

$$M_s = \sum_{\mathcal{C}} M_{s\mathcal{C}} \tag{8.13}$$

as

$$\langle M_s^2 \mathrm{Sign}\rangle_i = \sum_{\Lambda_{\mathcal{C}}} \langle M_{s\mathcal{C}}^2 \mathrm{Sign}_{\mathcal{C}}\rangle_i \prod_{\Lambda_{\mathcal{C}'} \neq \Lambda_{\mathcal{C}}} \langle \mathrm{Sign}_{\mathcal{C}'}\rangle_i. \tag{8.14}$$

8.3.4 Nested Cluster Algorithm in the SSE Representation

In SSE representation the nested cluster algorithm can be implemented in the same way as explained above. However, in practice it is easier to treat some details in a slightly different fashion.

Once the spins are integrated out, as described in subsection 8.3.1, one has to keep track of the number of clusters $N[\mathcal{C}]$ in the system. Every time a new break-up is proposed it has to be checked whether $N[\mathcal{C}]$ changes. This is an additional effort which can be omitted. The global updates, i.e. the insertion and removal of operators, can not update the sign as it is the case when the spins are integrated out. However, this is not a problem because the internal updates take care of it. So one can keep the spins and still propose internal updates for operators on bonds, where both spins are parallel, or where there is a transition. The internal update is now performed by flipping half of the cluster in order to maintain an allowed configuration, i.e. a configuration with non-zero Boltzmann weight.

8.3.5 Additional Energy Shift

In the SSE representation there are usually only transition operators that connect spins spatially. Thus we introduce an operator that connects spins forward in time with a higher energy shift than the usual shift of $E_s = \frac{J}{4}$

$$-H' = -H + E_s = \begin{pmatrix} -\frac{J}{4} + E_s & 0 & 0 & 0 \\ 0 & \frac{J}{4} + E_s & -\frac{J}{2} & 0 \\ 0 & -\frac{J}{2} & \frac{J}{4} + E_s & 0 \\ 0 & 0 & 0 & -\frac{J}{4} + E_s \end{pmatrix}. \tag{8.15}$$

Hence E_s is the weight of a new diagonal operator, which can be interchanged with off-diagonal operators via internal updates. If $E_s = \frac{3}{4}J$ is chosen, then internal updates can always be accepted and do not longer need a Metropolis accept-reject step because both operators have exactly the same weight. By further increasing E_s the probability to have cluster-internal operators also increases and thus the distribution of the sign (as will be presented in the below) can be made narrower. However, one has to pay for this by an additional computational effort, because the operator string will also grow. It is a rather tricky business to keep the right balance. This fine-tuning will be discussed in section 8.5.

8.4 Results

We considered the Heisenberg antiferromagnet with uniform nearest-neighbour coupling $J_{xy} = J$ on the frustrated square lattices illustrated in figure 8.4b. This geometry is further discussed in chapter 7. The frustrated square lattice has an additional coupling J' along the diagonals as described in chapter 7. We have simulated kagomé lattices, as illustrated in figure 8.4, with up to $V \approx 1000$ spins at moderate temperatures with $\beta J \approx 1$. Figure 8.5 shows the probability distribution of the improved estimator $\langle \text{Sign} \rangle_i$. Although sometimes it is negative, it still leads to an accurate determination of the average sign. We considered M_c and χ_c as defined in eqs. (7.5) and (7.6), which may signal coplanar spin order, as in the classical ground state on the triangular lattice described in the previous chapter. As shown in figure 8.6, with increasing volume V both $\langle \text{Sign} \rangle_+$ and $\langle M_c^2 \text{Sign} \rangle_+$ decrease dramatically over numerous orders of magnitude, but are still accurately accounted for by the nested cluster algorithm. For example, with $V = 882$ spins $\langle \text{Sign} \rangle_+ = 2.09(8) \times 10^{-14}$. A brute force approach would require an astronomical statistics of about 10^{30} sweeps in order to achieve a similar precision. Figure 8.7 shows the coplanar susceptibility χ_c compared to

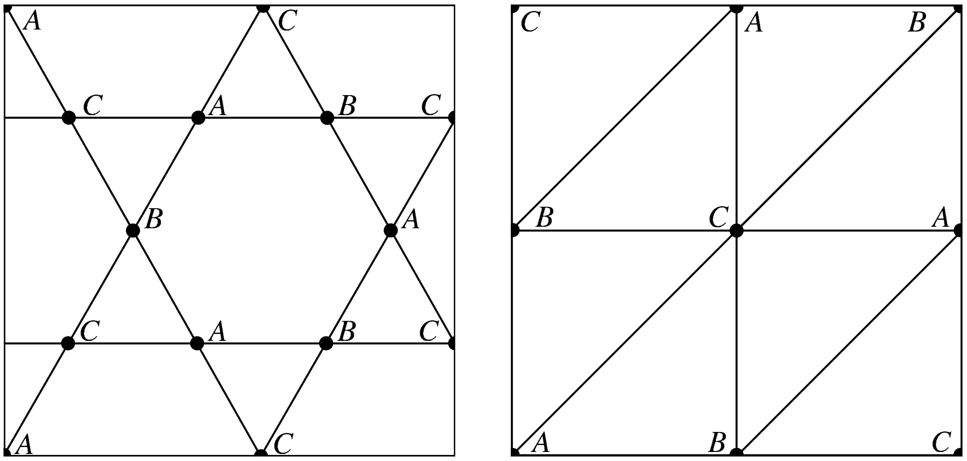

Figure 8.4: *Kagomé lattice (left) and frustrated square (or anisotropic triangular) lattice (right) consisting of three sublattices A, B, C.*

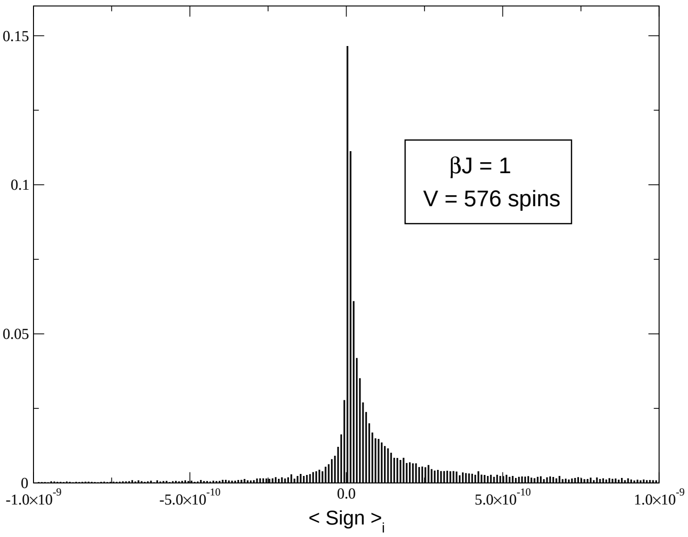

Figure 8.5: *Probability distribution of* $\langle Sign \rangle_i$ *for the kagomé lattice with* $V = 576$ *spins and* $\beta J = 1$.

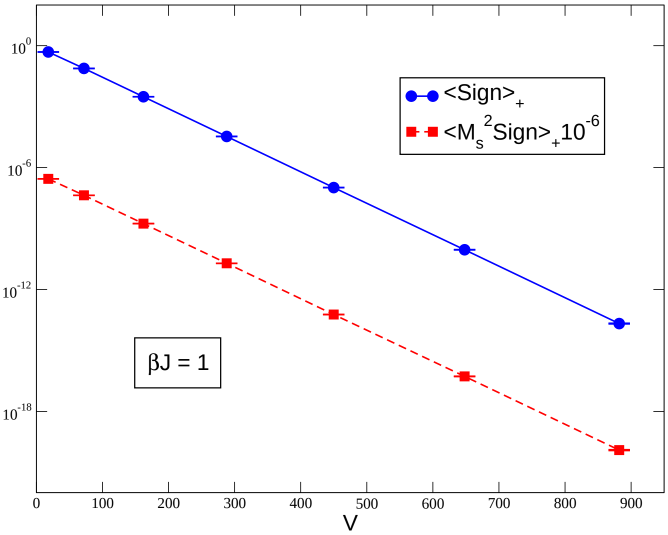

Figure 8.6: *Volume-dependence of* $\langle Sign \rangle_+$ *and* $\langle M_s^2 Sign \rangle_+$ *(rescaled by* 10^{-6}*) for the kagomé lattice with* $\beta J = 1$.

the collinear Néel susceptibility χ_s. On the square lattice, frustration reduces the Néel order, while (at least for $J' = J/4$) the coplanar order is as weak as on the kagomé lattice (and practically indistinguishable from it in figure 8.7).

To conclude, in contrast to other Monte Carlo methods, the nested cluster algorithm is capable of eliminating very severe sign problems for large systems, at least at moderate temperatures. As we have demonstrated, by studying appropriate susceptibilities one may obtain valuable insights concerning possible types of order.

8.5 Fine-Tuning of the Nested Cluster-Algorithm

The average sign of cluster $\langle \mathrm{Sign}_{\mathcal{C}} \rangle_i$ calculated by the internal Monte Carlo updates hugely varies from cluster to cluster. Thus it is important to find a rule that determines the number of internal updates performed on each cluster. In order to get an error of the order of $\langle \mathrm{Sign}_{\mathcal{C}} \rangle_i$ one should perform about $\langle \mathrm{Sign}_{\mathcal{C}} \rangle_i^{-2}$ internal updates. However, in order to maintain a correct algorithm, the rule should always be the same for a certain set of spins $\Lambda_{\mathcal{C}}$ defined by the cluster. A good method is to plot the sign of a cluster as a function of the number of internal plaquettes of a cluster $\#\mathrm{int}_{\mathcal{C}}$. The sign scales roughly exponentially with the number of internal plaquettes. This can be fitted with

$$f(\#\mathrm{int}_{\mathcal{C}}) = \exp(-b\#\mathrm{int}_{\mathcal{C}}) \tag{8.16}$$

to determine the slope b of the exponential. An example for the triangular lattice is shown in figure 8.8. The number of internal updates $u(\#\mathrm{int}_{\mathcal{C}})$ as a function of the number of internal plaquettes can thus be chosen as

$$u(\#\mathrm{int}_{\mathcal{C}}) = a + \exp(2b\#\mathrm{int}_{\mathcal{C}}), \tag{8.17}$$

where a is a constant chosen to make sure that a minimal internal sampling takes place. In practice it is also good to choose a maximum of internal updates, because the algorithm might otherwise be stuck forever in the update of a single cluster. Also the factor of 2 which is necessary to get an error of the order of the average sign was in practice too large because also it would quickly get the algorithm stuck in the update of a single cluster. We would rather use

$$u(\#\mathrm{int}_{\mathcal{C}}) = a + \exp(b\#\mathrm{int}_{\mathcal{C}}). \tag{8.18}$$

In practice we usually chose $a \approx 10, \ldots, 100$ and $u_{\max} \approx 10^6, \ldots, 10^7$.

Obviously not only the number of internal plaquettes, but also the internal structure matters whether the average sign is very small. A possibility is thus to measure on which sublattices the sites on the internal plaquettes lie, i.e. $\#\mathrm{int}_{\mathcal{C}}^A$, $\#\mathrm{int}_{\mathcal{C}}^B$, and $\#\mathrm{int}_{\mathcal{C}}^C$ with

$$\#\mathrm{int}_{\mathcal{C}}^A + \#\mathrm{int}_{\mathcal{C}}^B + \#\mathrm{int}_{\mathcal{C}}^C = 2\#\mathrm{int}_{\mathcal{C}}. \tag{8.19}$$

If the internal plaquettes are mainly on two sublattices, then not many internal updates can be performed. We can thus take the geometrical mean of the contribution to the three

Energy shift $c[J]$	$\langle$Sign$\rangle$	Computer time[min]
0.75	$1.63(2) \times 10^{-2}$	11
1.75	$1.64(1) \times 10^{-2}$	24
2.75	$1.635(6) \times 10^{-2}$	56
3.75	$1.638(5) \times 10^{-2}$	230

Table 8.1: *Average sign and error, as well as time used to generate of the simulations shown in figure 8.10. In each simulation* 10^6 *outer Monte Carlo updates were performed. The error estimate of the average sign decreases with increasing energy shift, but also the computer time needed rapidly increases. Also there is no big difference in the error estimate between an energy shift of* $2.75J$ *and* 3.75 *although the computer time needed is about 4 times longer.*

sublattices of the internal plaquettes and redefine $\#\widetilde{\mathrm{int}}_{\mathcal{C}}$ as

$$\#\widetilde{\mathrm{int}}_{\mathcal{C}} = \left(\#\mathrm{int}_{\mathcal{C}}^{A} \#\mathrm{int}_{\mathcal{C}}^{B} \#\mathrm{int}_{\mathcal{C}}^{C}\right)^{\frac{1}{3}} . \tag{8.20}$$

Furthermore, when we run the algorithm using SSE, the energy shift E_s is another fine-tuning parameter. By increasing E_s the probability of internal operators in a cluster and with it the probability to achieve a good average of the sign increases. This can be seen in figure 8.9, where at $E_s = \frac{3}{4}J$ there are a lot of small clusters with a very small average sign that do not fit the exponential scaling. With an energy shift $E_s = \frac{7}{4}J$ this fits much better with an exponential scaling rule.

As a result the histograms become narrower, but also require much more time to generate. In figure 8.10 histograms for energy-shifts of $E_s = \frac{3}{4}J$, $E_s = \frac{7}{4}J$, $E_s = \frac{11}{4}J$, and $E_s = \frac{15}{4}J$ are shown. While the error of the sign decreases with an increasing energy shift, also the time used to generate these histograms increased substantially as shown in table 8.5 There is obviously a gain in the precision of the error estimate, once the energy shift is further increased. But with a very large energy shift this is beaten by the increasing system size and thus much more computer time is needed. A good choice of the energy shift on the triangular lattice is $E_s = 2.75J$ as it can be seen in table 8.5.

On different lattices, the optimal fine-tuning parameters have to be determined individually. This is a rather tedious task, but it saves a lot of computer time in productive simulation.

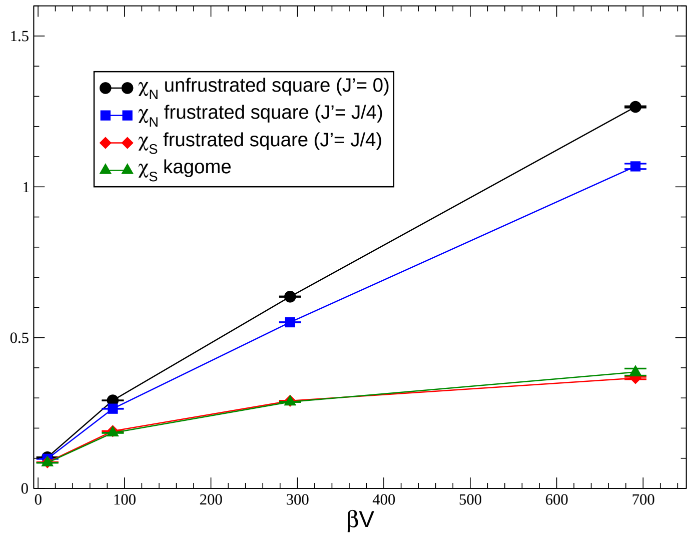

Figure 8.7: *Coplanar staggered susceptibility* χ_c *and collinear Néel susceptibility* χ_s *as functions of the space-time volume* βV *for the kagomé as well as the frustrated* $(J' = J/4)$ *and unfrustrated* $(J' = 0)$ *square lattice at fixed space/time aspect ratio* $\sqrt{V}/\beta J = 20$.

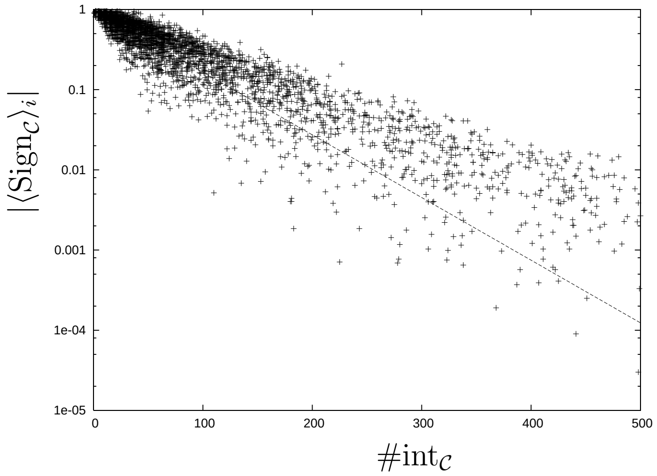

Figure 8.8: *The sign as a function of the number of internal plaquettes per cluster. The solid line is a fit of* $f(\#\mathrm{int}_{\mathcal{C}})$ *with* $b = 0.018$ *to the set of data points. This was done on a* 6×6 *triangular lattice at* $\beta = 1.0$. *There are 4000 data points. For this measurement a fixed number of* 10^5 *updates was performed on each cluster. This was done in order to get a good fit for b which could afterwards be used to define the number of internal updates as a function of the number of internal plaquettes.*

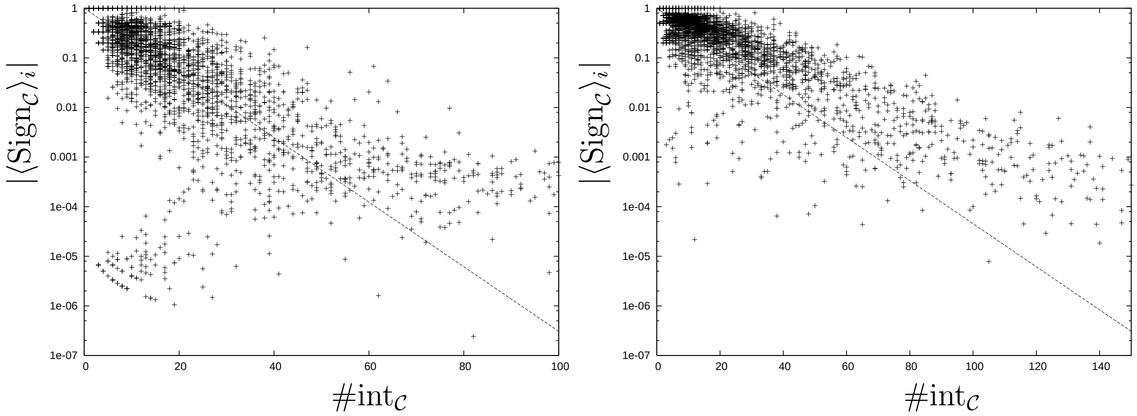

Figure 8.9: *The sign as a function of the number of internal operators* $\#int_{\mathcal{C}}$ *in the nested cluster-algorithm in SSE. Here the cluster size is twice the number of internal operators. The solid line is a fit of* $f(\#int_{\mathcal{C}})$. *In each figure* 10^4 *data points are generated on a* 12×12 *triangular lattice at* $\beta = 1.0$. *a) SSE simulation with an energy shift of* $E_s = \frac{3}{4}J$ *and a fit with* $b = 0.15$. *b) SSE simulation with an energy shift of* $E_s = \frac{7}{4}J$ *and a fit with* $b = 0.1$.

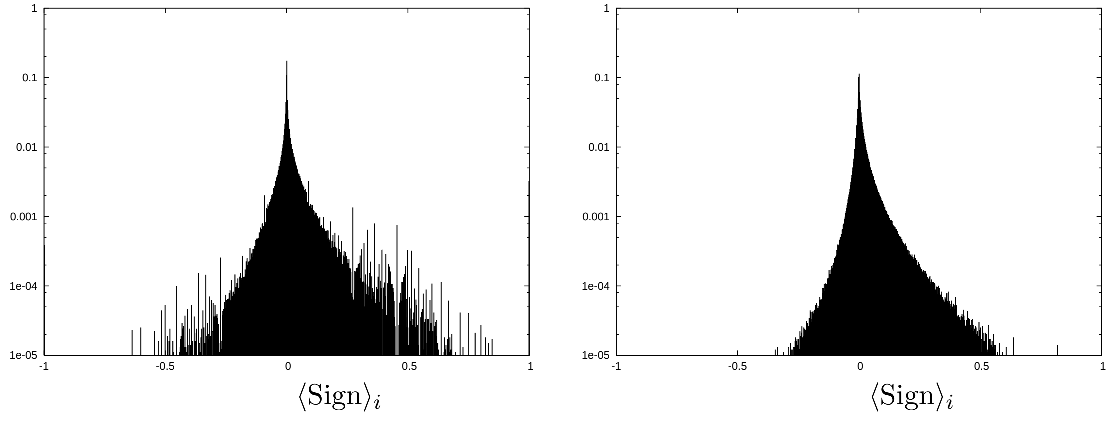

Figure 8.10: *Distribution of the sign on a* 6×6 *lattice at* $\beta = 1.0$ *generated with the nested cluster algorithm in SSE using an energy shift of a)* $E_s = 0.75J$, *b)* $E_s = 3.75J$. *It is clearly visible that the distribution of the simulation with a higher energy shift is narrower.*

Chapter 9

Nested Cluster Algorithm for Real-Time Evolution of a Quantum Spin System

The real-time evolution of a physical system is of central importance in non-equilibrium physics. For a quantum system one can observe how it equilibrates after a quench. Theoretically, this is very challenging, because for large systems it is impossible to perform such calculations analytically. Also it is an interesting computational problem, because even numerically this is hard to solve.

As seen above, the simulation of a quantum spin system in thermal equilibrium can be performed by setting up a path integral, which describes the evolution in an additional Euclidean time direction of extent β. We have seen that this can lead to a sign problem for antiferromagnets on frustrated lattices. If one now wants to calculate the real-time evolution

$$|\Psi(t)\rangle = \exp(-iHt)|\Psi(0)\rangle \tag{9.1}$$

of a many-body wave function, such as a quantum Heisenberg antiferromagnet with an initial state $|\Psi(0)\rangle$, one can also set up a path integral in Minkowski time

$$Z = \langle\Psi(0)|\exp(-iHt)\exp(iHt)|\Psi(0)\rangle = 1 = \sum_{[s]} \mathrm{Phase}[s]|\exp(-S[s])|. \tag{9.2}$$

Observables at a certain time t can then be measured as

$$\langle\mathcal{O}(t)\rangle = \langle\Psi(0)|\exp(-iHt)\mathcal{O}\exp(iHt)|\Psi(0)\rangle. \tag{9.3}$$

One can also couple such a system to a heat-bath with inverse temperature β

$$Z_\beta = \mathrm{Tr}\left[\exp(-\beta H)\exp(-iHt)\exp(iHt)\right] = \sum_{[s]} \mathrm{Phase}[s]|\exp(-S[s])|. \tag{9.4}$$

Observables such as e.g. two-point functions in real-time are thus calculated as

$$\langle c_x(0)c_y(t)\rangle_\beta = \frac{1}{Z_\beta}\mathrm{Tr}\left[\exp(-\beta H)c_x\exp(-iHt)c_y\exp(iHt)\right]. \tag{9.5}$$

The contributions to this path integral are neither guaranteed to be positive nor real. One way to deal with this is to do the same as one does with a sign problem, by simulating the absolute values of the Boltzmann weights and treating the phase Phase$[s]$ as an observable

$$\langle \mathcal{O}(t) \rangle = \frac{\langle \mathcal{O}(t) \mathrm{Phase} \rangle_+}{\langle \mathrm{Phase} \rangle_+} \tag{9.6}$$

The averages $\langle\rangle_+$ are measured using a modified partition function

$$Z_+ = \sum_{[s]} |\exp(-S[s])|. \tag{9.7}$$

Thus we are not really sampling a partition function as we do in normal equilibrium physics simulations. This already gives us a hint that importance sampling might not be the best method to perform high accuracy calculations. Nevertheless, it is a method that works and is better than brute force Monte Carlo.

9.1 Factorisation of the Phase

In this section we will explain the method for a spin $\frac{1}{2}$ Heisenberg antiferromagnet in the framework of SSE. The lattice geometry does not matter here.

The path integral now takes the form

$$\begin{aligned} Z &= \langle \Psi(0) | \exp(-iHt) \exp(iHt) | \Psi(0) \rangle \\ &= \langle \Psi(0) | \sum_{n=0}^{\infty} \frac{t^n}{n!} (-iH)^n \sum_{n=0}^{\infty} \frac{t^n}{n!} (iH)^n | \Psi(0) \rangle. \end{aligned} \tag{9.8}$$

There are two path integrals after each other, one forward and one backward in time. Forward in time we consider

$$-iH = \frac{iJ}{4} \begin{pmatrix} -1 & 0 & 0 & 0 \\ 0 & 1 & -2 & 0 \\ 0 & -2 & 1 & 0 \\ 0 & 0 & 0 & -1 \end{pmatrix}. \tag{9.9}$$

We cannot remove the sign of the diagonal elements by an energy shift, because they are complex. However, it is possible to distribute the phase over the individual bonds of some operators B and C as shown in figure 9.1 and 9.2. As it is in the case for frustrated antiferromagnets. Where we have a sign problem in the case of the frustrated antiferromagnets, we now have a complex action problem. This problem can also not be solved with the meron-cluster algorithm. The clusters do not change their complex phase under cluster-flip, because only the B-type bonds change the phase and because in every cluster there is an even number of such bonds. Thus, the overall complex phase of a cluster does not change.

In the pure time-evolution without a heat-bath, the initial state $\Psi(0)$ is kept by not allowing flips of clusters that go through or touch the time-slice at time 0.

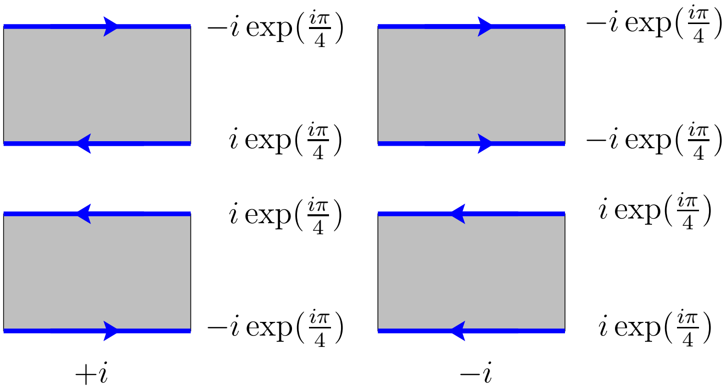

Figure 9.1: *Factorisation of the phase of the B-type operators into two phase-factors. The factors are assigned to the cluster bonds. These bonds change by a factor of -1 under cluster-flip.*

9.2 Internal Cluster Updates

Again internal Monte Carlo updates on the individual clusters can be performed. Here, for every internal operator, an internal rewiring can be performed as it is illustrated in figure 9.3.

If the system is coupled to a heat-bath, due to the C-type operators shown in figure 9.2, also in the thermal part of the path integral internal updates can be performed as it is done on the frustrated lattices.

It is not advisable to use an energy shift as we did for SSE in the previous chapter. By doing so one would not generate unit-matrix operators, but rather operators with a phase of i or $-i$. It is best to just interchange them. Thus only the third type of rewiring in figure 9.3 makes sense in SSE.

9.3 Results for Real-Time Evolution with a Fixed Initial State

For a Heisenberg antiferromagnet with very few spins we could reproduce the analytically calculable real-time evolution of an initial classical Néel state. For a 2×2 square, where states are denoted by $|s_1 s_2 s_3 s_4\rangle = |s_1 s_{1+\hat{1}} s_{1+\hat{2}} s_{1+\hat{1}+\hat{2}}\rangle$, the Néel state $|\uparrow\downarrow\downarrow\uparrow\rangle$ can evolve into a combination of $|\uparrow\uparrow\downarrow\downarrow\rangle$, $|\uparrow\downarrow\uparrow\downarrow\rangle$, $\uparrow\downarrow\downarrow\uparrow\rangle$, $|\downarrow\uparrow\uparrow\downarrow\rangle$, $|\downarrow\uparrow\downarrow\uparrow\rangle$ and $|\downarrow\downarrow\uparrow\uparrow\rangle$. It is straightforward to calculate the probabilities

$$p_{s_1 s_2 s_3 s_4} = |\langle \text{Néel}| \exp(-iHt) |s_1 s_2 s_3 s_4\rangle|^2. \tag{9.10}$$

which are illustrated in figure 9.4. By using our algorithm we can reproduce the analytically calculated probabilities in figure 9.4 up to $t = 1.0/J$ within a few hours on a single workstation. This is shown in figure 9.5.

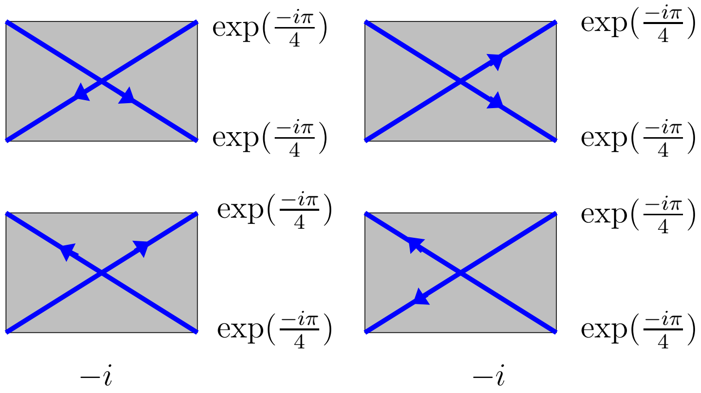

Figure 9.2: *Factorisation of the phase of the C-type operators into two phase-factors. The factors are assigned to the cluster bonds. These bonds carry the same phase independent of their orientation and does do not change phase under cluster-flip.*

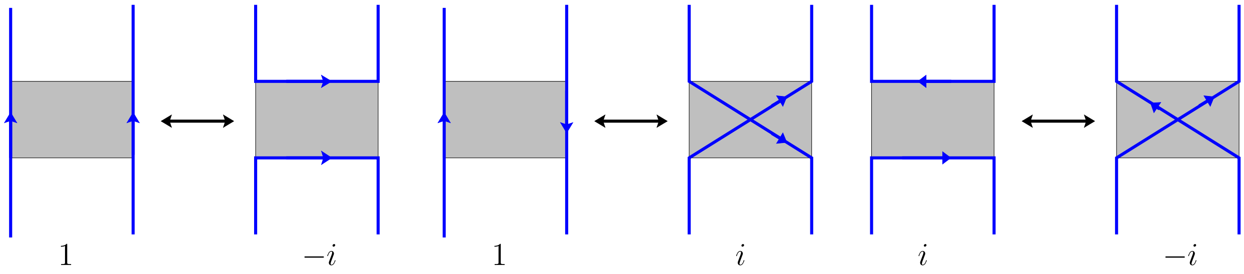

Figure 9.3: *Three possible internal updates and their resulting phase. The second rewiring goes from 1 to i, because the off-diagonal -1 is cancelled by an other phase, resulting from flipping half the cluster. Only the third type is used in SSE.*

For such a system a histogram of the average ⟨Phase⟩, which is real and thus rather an average sign, is illustrated for a 2×2 lattice with evolution in time of $t = 3.0/J$ in figure 9.6a. Because we work with a fixed initial state, there are a lot of clusters in the system that cannot be flipped and thus internal updates are often rejected. Because of that there are two additional peaks in the histogram at 1 and -1. This is very bad and one of the reasons why the nested algorithm does not perform as well as in the case of thermal averages of frustrated antiferromagnets. Furthermore, there are clusters contributing a phase of exactly zero and thus quite a lot of generated contributions do not contribute to the path integral.

One may have expected that our method is not very efficient and the sign problem is much harder than that of frustrated antiferromagnets. This is due to the fact that importance sampling of a system which does not have a thermal distribution that can be interpreted probabilistically, seems not to be the appropriate method.

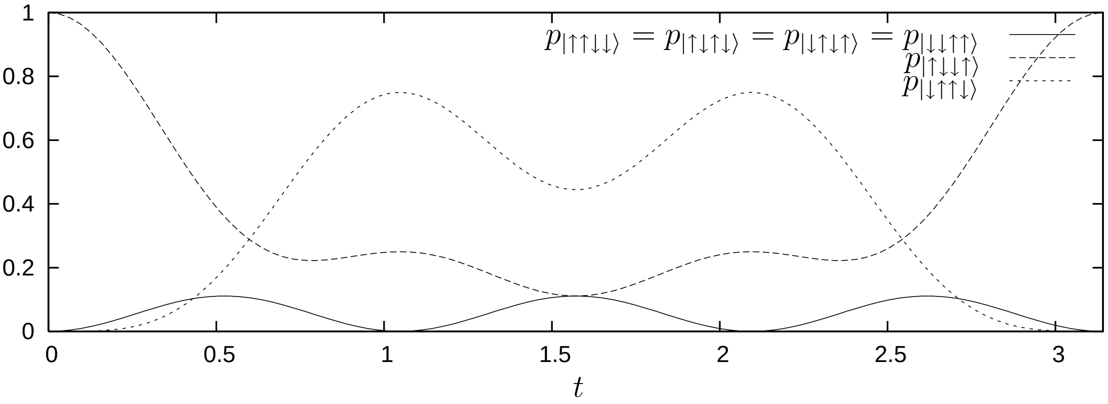

Figure 9.4: *Probability of states after time t of an initially Néel ordered 2×2 square antiferromagnet from time 0 to π.*

9.4 Results for the Real-Time Evolution Coupled to a Heat-Bath

Similar calculations can be performed for the real-time evolution coupled to a heat-bath. First of all as shown in figure 9.7 in the distribution of the complex phase the peaks at ±1 start to disappear because the clusters can now be always flipped. But the distribution is very broad.

Because the initial state is now sampled with a Boltzmann distribution, instead of only measuring observables at time t we rather measure the correlation of an observable $\mathcal{O}$ with itself in time

$$\langle \mathcal{O}(0)\mathcal{O}(t) \rangle = \frac{\mathrm{Tr}[\exp(-\beta H)\mathcal{O}\exp(-iHt)\mathcal{O}\exp(iHt)}{\mathrm{Tr}[\exp(-\beta H)]}. \tag{9.11}$$

We thus measured the correlation in time of the staggered susceptibility $\langle M_s^3(0) M_s^3(t) \rangle$. We tested this on a spin chain with two spins where this observable is easily analytically calculable. Our simulation reproduces the correct result as shown in figure 9.8. On larger lattices this observable is much harder to calculate. Due to limited computer resources and the very severe complex action problem we did not further pursue such measurements. Thus we have not measured anything that cannot be measured otherwise. Still we were able to show that with the nested algorithm we can in principle perform measurements of the real-time evolution of quantum spin systems. The complex phases that occur can be factorised to the clusters and inner Monte Carlo updates can be performed in a very similar way as in the last chapter.

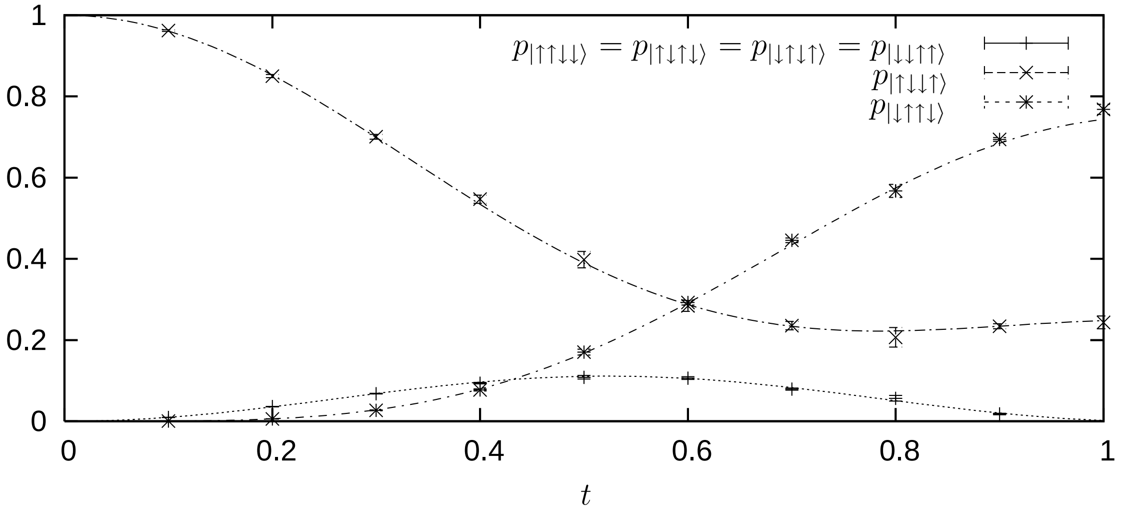

Figure 9.5: *Measurements of the probabilities of states after time t of an initially Néel ordered 2×2 square antiferromagnet. The lines are the analytical results, whereas the crosses and bars are the Monte Carlo measurements.*

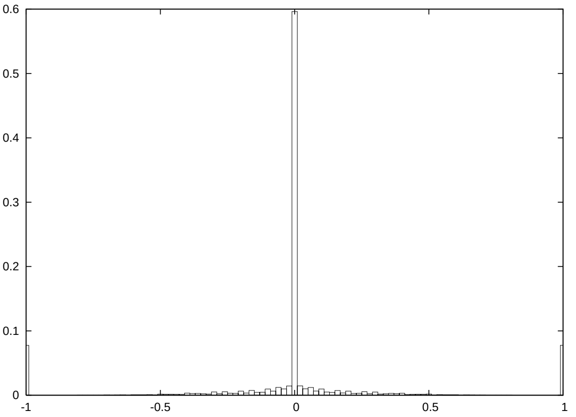

Figure 9.6: *Distribution of the sign in the simulation of an initially Néel ordered 2×2 square antiferromagnet evolving in time from $t = 0$ to $t = 3.0/J$. Here, it is only a sign, because in real-time evolution with a fixed initial state the complex contributions cancel. The distribution is very narrow around 0, but there are also two peaks at ±1 which are one of the reasons why the method is not very efficient.*

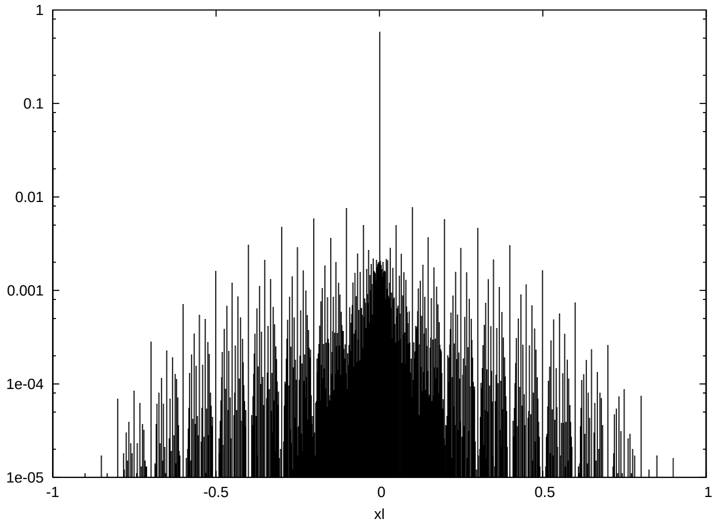

Figure 9.7: *Distribution of the real part of the complex phase* $\Re\langle Phase\rangle$ *in the simulation of the real-time evolution evolving in time from* $t = 0$ *to* $t = 1.0/J$ *coupled to a heat-bath with inverse temperature* $\beta = 10.0/J$ *on a* 6×6 *lattice on a logarithmic scale from* 10^6 *cluster updates.*

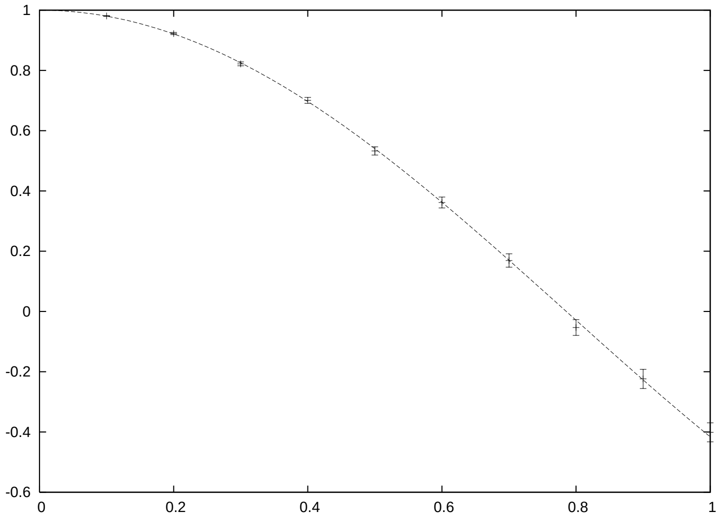

Figure 9.8: *Correlation in time of the real part of the staggered susceptibility* $\Re\langle M_s^3(0)M_s^3(t)\rangle$ *on an* $L = 2$ *spin chain coupled to a heat-bath at* $\beta = 10.0/J$. *The line is the analytical result.*

Part II

Simulations of Single Electrons and Holes in the t-J Model

Chapter 10

The t-t'-J Model on the Square Lattice and its Three Low-Energy Effective Field Theories

The t-t'-J model is a microscopic model describing holes or electrons with at most one particle per site. At half-filling, i.e. with one electron on every site, this corresponds to a spin $\frac{1}{2}$ Heisenberg antiferromagnet. At sufficiently large doping, the model is expected to become superconducting. However, because of the fermion sign problem this is currently not possible to realise in a computer simulation. Simulations of the single-hole sector can be performed and used to calculate the single-hole dispersion relation, which is what we will do in the following chapters.

In the dispersion relation of the t-J model on the square lattice, the shape of the minima — the so-called pockets — are qualitatively remarkably similar to the hole-pockets observed with angle resolved photo-emission spectroscopy (ARPES) measurements [89–92]. However, quantitatively the experimentally observed pockets are more elliptical than the pockets observed in the Monte Carlo simulations of the t-J model. By adding a diagonal hopping term of strength t' to the t-J model Hamiltonian, which is thus the t-t'-J model Hamiltonian, the shape of the pockets can be influenced. By doing so the location of the minima can be changed.

10.1 Microscopic Formulation

The t-$'t$-J model is defined by the Hamilton operator

$$\begin{aligned} H &= P\Big\{ -t \sum_{x,i} (c_x^\dagger c_{x+\hat{i}} + c_{x+\hat{i}}^\dagger c_x) - t' \sum_{x,s\in\{\pm 1\}} (c_x^\dagger c_{x+\hat{1}+s\hat{2}} + c_{x+\hat{1}+s\hat{2}}^\dagger c_x) \\ &\quad + J \sum_{x,i} \vec{S}_x \cdot \vec{S}_{x+\hat{i}} - \mu \sum_x Q_x \Big\} P, \end{aligned} \tag{10.1}$$

with

$$c_x = \begin{pmatrix} c_{x\uparrow} \\ c_{x\downarrow} \end{pmatrix}, \quad S_x = c_x^\dagger \frac{\vec{\sigma}}{2} c_x, \quad Q_x = (c_x^\dagger c_x - 1). \tag{10.2}$$

There are two hopping terms: The one with strength t describes hopping along the x- and y-axis and the other with strength t' describes hopping along the diagonals. The operator P projects out the configurations with doubly occupied sites. In contrast to the Hubbard model, the t-t'-J model only allows empty or at most singly occupied sites.

10.2 The Location of the Pockets in the t-t'-J Model

By tuning the parameters t and t', three distinct locations of the minima — the so-called pockets — in the dispersion relation of one single charge carrier in t-t'-J model can be realised. These three locations in the parameter space of t, t', and J are:

- **I**: For $|t'| \ll t$, pockets at $(\pm\frac{\pi}{2a}, \pm\frac{\pi}{2a})$ are realised. This corresponds to hole-doped antiferromagnets.
- **II**: For $t'/t \ll 0$, circular pockets located at $(\frac{\pi}{a}, 0)$ and $(0, \frac{\pi}{a})$ are realised, which correspond to the location of the pockets in electron-doped antiferromagnets, and are thus called electron-pockets.
- **III**: For $t'/t \gg 0$, it is even possible to observe pockets at $(0, 0)$ and $(\frac{\pi}{a}, \frac{\pi}{a})$, which seem not to correspond to any known real material.

These three possible shapes of the dispersion relation are shown in figure 10.1,

The technique to measure two-point correlation functions described in section 10.6 can be modified to analytically summing up terms and only afterwards filling in the parameters t and t'. Thus the whole parameter-space of t and t' can be simultaneously calculated. The only disadvantage is that this costs a lot more computer-time and thus one cannot go as far in Euclidean time as is otherwise possible. It is thus not always completely sure whether we have yet reached the lowest energy level. The result of this calculation is shown in figure 10.2, where there is quite a large uncertainty concerning the transition lines. Nevertheless, although the exact transition line is not determined here, there is a clear division of the parameter space of t, t', and J into three distinct regions.

If one was able perform calculations of the systems with a finite density of charge carriers, distinct phases in the t-t'-J model should emerge. The figure presented in 10.2 gives us a first hint how it could look like.

These three regions with their distinct location of the pockets in the dispersion relation described above lead to three different low-energy effective field theories. The low-energy effective field theory for the magnons is the same for all three cases in 10.1, but low-energy behaviour of the fermions is different as discussed below in section 10.4.

10.3 Magnon Field Transformation Rules

This section is a brief review of the effective theory for magnons and holes in an antiferromagnet on the square lattice. We list the symmetry transformation rules for magnon and hole fields under the various symmetries of the underlying t-J model needed for the construction of the effective Lagrangian.

As discussed in chapter 3, the staggered magnetisation $\vec{e}(x)$ takes values in the coset space $SU(2)_s/U(1)_s = S^2$, with $x = (x_1, x_2, t)$ denoting a point in $(2+1)$-dimensional space-time. Using the nonlinear realisation of the global $SU(2)_s$ spin symmetry, which is spontaneously broken to its $U(1)_s$ subgroup, this leads to an Abelian “gauge” field $v_\mu^3(x)$ and to two vector fields $v_\mu^\pm(x)$ which are “charged” under $U(1)_s$ spin transformations. The coupling of magnons to holes is realised through a matrix-valued anti-Hermitian field.

For this construction it is convenient to use a $\mathbb{C}P(1)$ representation of the magnon fields $\vec{e}$ in terms of 2×2 Hermitean projection matrices $P(x)$ with

$$P(x) = \frac{1}{2}(\mathbb{1} + \vec{e}(x) \cdot \vec{\sigma}) \quad P(x)^\dagger = P(x), \quad \mathrm{Tr}P(x) = 1, \quad P(x)^2 = P(x). \tag{10.3}$$

The spontaneously broken $SU(2)_s$ symmetry is nonlinearly realised on the hole fields. The global $SU(2)_s$ symmetry then manifests itself as a local $U(1)_s$ symmetry in the unbroken subgroup and the hole fields couple to the magnon fields via composite vector fields. In order to construct these vector fields one has to diagonalise $P(x)$ by a unitary transformation $u(x) \in SU(2)$ as

$$u(x)P(x)u(x)^\dagger = \frac{1}{2}(\mathbb{1} + \sigma_3) = \begin{pmatrix} 1 & 0 \\ 0 & 0 \end{pmatrix}, \qquad u_{11}(x) \geq 0. \tag{10.4}$$

In order to make $u(x)$ uniquely defined, we demand that the element $u_{11}(x)$ is real and non-negative. Under a global $SU(2)_s$ transformation g, the diagonalising field $u(x)$ transforms as

$$u(x)' = h(x)u(x)g^\dagger, \tag{10.5}$$

which implicitly and uniquely defines the nonlinear symmetry transformation

$$h(x) = \exp(i\alpha(x)\sigma_3) = \begin{pmatrix} \exp(i\alpha(x)) & 0 \\ 0 & \exp(-i\alpha(x)) \end{pmatrix} \in \ U(1)_s. \tag{10.6}$$

Under the displacement symmetry D_i the staggered magnetisation changes sign, i.e ${}^{D_i}\vec{e}(x) = -\vec{e}(x)$, such that one obtains

$${}^{D_i}u(x) = \tau(x)u(x) \tag{10.7}$$

with

$$\tau(x) = \begin{pmatrix} 0 & -\exp(-i\phi(x)) \\ \exp(i\phi(x)) & 0 \end{pmatrix}. \tag{10.8}$$

In order to couple the magnons and charge carriers, one constructs the traceless anti-Hermitean field

$$v_\mu(x) = u(x)\partial_\mu u(x)^\dagger, \tag{10.9}$$

which transforms under the symmetries inherited from the underlying t-J model as

$$\begin{aligned}
SU(2)_s: &\quad v_\mu(x)' = h(x)[v_\mu(x) + \partial_\mu]h(x)^\dagger,\\
D_i: &\quad {}^{D_i}v_\mu(x) = \tau(x)[v_\mu(x) + \partial_\mu]\tau(x)^\dagger,\\
D_i': &\quad {}^{D_i'}v_\mu(x) = v_\mu(x)^*,\\
O: &\quad {}^{O}v_i(x) = \varepsilon_{ij}v_j(Ox), \quad {}^{O}v_t(x) = v_t(Ox),\\
R: &\quad {}^{R}v_1(x) = v_1(Rx), \qquad {}^{R}v_2(x) = -v_2(Rx), \quad {}^{R}v_t(x) = v_t(Rx),\\
T: &\quad {}^{T}v_j(x) = {}^{D_i}v_j(Tx), \quad {}^{T}v_t(x) = -{}^{D_i}v_t(Tx),\\
T': &\quad {}^{T'}v_j(x) = {}^{D_i'}v_j(Tx), \quad {}^{T'}v_t(x) = -{}^{D_i'}v_t(Tx).
\end{aligned} \tag{10.10}$$

The various symmetries are the $SU(2)_s$ spin rotations, the displacement symmetry by one lattice spacing in the i-direction D_i, the symmetry D_i combined with the spin rotation $i\sigma_2$ resulting in D_i', as well as the 90 degrees rotation O, the reflection at the x_1-axis R, time reversal T, and T combined with the spin rotation $i\sigma_2$ resulting in T' [26] which are given by

$$Ox = (-x2, x1, t), \quad Rx = (x1, -x2, t), \quad Tx = (x1, x2, -t). \tag{10.11}$$

Finally, the field $v_\mu(x)$ decomposes into the Abelian "gauge" field $v_\mu^3(x)$ and two "charged" vector fields $v_\mu^\pm(x)$, i.e.

$$v_\mu(x) = iv_\mu^a(x)\sigma_a, \quad v_\mu^\pm = v_\mu^1(x) \mp iv_\mu^2(x), \tag{10.12}$$

where $\vec{\sigma}$ are the Pauli matrices.

The construction presented here is discussed in more detail in [24–26].

10.4 Low-Energy Fermion Field Transformation Rules

For the construction of the fermion fields, it is important to know where the minima of the fermion dispersion relations are located in the Brillouin zone. There are three known locations as already discussed in section 10.2 which are displayed in figure 10.1.

10.4.1 Fermion Fields for Hole-doped Systems

Angle resolved photo-emission spectroscopy (ARPES) experiments [89–92] as well as theoretical investigations [93–100] show that hole-doped systems have their pockets centered at $(\pm\frac{\pi}{2a}, \pm\frac{\pi}{2a})$. First principles microscopic simulations, discussed later in this thesis, do confirm this. By identifying the proper fields with these positions in momentum space, one can construct fermion fields that transform under the various symmetries [24] as

$$\begin{aligned}
SU(2)_s: &\quad \psi^f_\pm(x)' = \exp(\pm i\alpha(x))\psi^f_\pm(x), \\
U(1)_Q: &\quad {}^Q\psi^f_\pm(x) = \exp(i\omega)\psi^f_\pm(x), \\
D_i: &\quad {}^{D_i}\psi^f_\pm(x) = \mp\exp(ik^f_i a)\exp(\mp i\varphi(x))\psi^f_\mp(x), \\
D'_i: &\quad {}^{D'_i}\psi^f_\pm(x) = \pm\exp(ik^f_i a)\psi^f_\mp(x), \\
O: &\quad {}^O\psi^\alpha_\pm(x) = \mp\psi^\beta_\pm(Ox), \quad {}^O\psi^\beta_\pm(x) = \psi^\alpha_\pm(Ox), \\
R: &\quad {}^R\psi^\alpha_\pm(x) = \psi^\beta_\pm(Rx), \qquad {}^R\psi^\beta_\pm(x) = \psi^\alpha_\pm(Rx), \\
T: &\quad {}^T\psi^f_\pm(x) = \pm\exp(\mp i\varphi(Tx))\psi^{f\dagger}_\pm(Tx), \\
&\quad {}^T\psi^{f\dagger}_\pm(x) = \mp\exp(\pm i\varphi(Tx))\psi^f_\pm(Tx), \\
T': &\quad {}^{T'}\psi^f_\pm(x) = \mp\psi^{f\dagger}_\pm(Tx), \\
&\quad {}^{T'}\psi^{f\dagger}_\pm(x) = \pm\psi^f_\pm(Tx).
\end{aligned} \tag{10.13}$$

Here $f \in \{\alpha, \beta\}$ are two flavour indices identified with the pockets $\alpha = \{(\frac{\pi}{2a}, \frac{\pi}{2a}), (-\frac{\pi}{2a}, -\frac{\pi}{2a})\}$ and $\beta = \{(\frac{\pi}{2a}, -\frac{\pi}{2a}), (-\frac{\pi}{2a}, \frac{\pi}{2a})\}$ and the spin-index is $s \in \{+, -\}$. The vectors k^f define the location of the pockets as

$$k^\alpha = \left(\frac{\pi}{2a}, \frac{\pi}{2a}\right), \quad k^\beta = \left(\frac{\pi}{2a}, -\frac{\pi}{2a}\right). \tag{10.14}$$

Here $U(1)_Q$ is the fermion number symmetry of the holes. The action of magnons and holes must be invariant under these symmetries.

10.4.2 Low-Energy Fermion Fields for Electron-Doped Systems

By using electron-hole duality, we transform the electrons into holes and use the t-t'-J model to describe those. However, in contrast to holes, electron-doped systems have their pockets at $(\frac{\pi}{a}, 0)$ and $(0, \frac{\pi}{a})$, which is again indicated by ARPES measurements and theoretical investigations [101–107]. After identifying the pockets, under the various symmetries the fermion fields transform as [26]

$$
\begin{aligned}
SU(2)_s: &\quad \psi_\pm(x)' = \exp(\pm i\alpha(x))\psi_\pm(x),\\
U(1)_Q: &\quad {}^Q\psi_\pm(x) = \exp(i\omega)\psi_\pm(x),\\
D_i: &\quad {}^{D_i}\psi_\pm(x) = \mp\exp(ik_ia)\exp(\mp i\varphi(x))\psi_\mp(x),\\
D_i': &\quad {}^{D_i'}\psi_\pm(x) = \pm\exp(ik_ia)\psi_\mp(x),\\
O: &\quad {}^O\psi_\pm(x) = \pm\psi_\pm(Ox),\\
R: &\quad {}^R\psi_\pm(x) = \psi_\pm(Rx),\\
T: &\quad {}^T\psi_\pm(x) = \exp(\mp i\varphi(Tx))\psi^\dagger_\pm(Tx),\\
&\quad {}^T\psi^\dagger_\pm(x) = -\exp(\pm i\varphi(Tx))\psi_\pm(Tx),\\
T': &\quad {}^{T'}\psi_\pm(x) = -\psi^\dagger_\pm(Tx),\\
&\quad {}^{T'}\psi^\dagger_\pm(x) = \psi_\pm(Tx),
\end{aligned}
\tag{10.15}
$$

where the vector k is defined as

$$
k = \left(\frac{\pi}{a}, 0\right). \tag{10.16}
$$

The action of magnons and electrons must be invariant under these symmetries. In this case, there is no flavour index because the pocket at $(\frac{\pi}{a}, 0)$ can be identified with the pocket at $(\frac{\pi}{a}, 0)$ by the $(\frac{\pi}{a}, \frac{\pi}{a})$ displacement symmetry.

10.4.3 Transformation Rules for Fermion Fields Located at $(0, 0)$ and $(\frac{\pi}{a}, \frac{\pi}{a})$

By tuning the parameters of the t-t'-J model it is possible to realise pockets in momentum space centered at $(0, 0)$ and $(\frac{\pi}{a}, \frac{\pi}{a})$ in a Monte Carlo simulation of the microscopic model. They do not correspond to any known material, but still it is interesting to consider this case. Indeed, the first fully systematic low-energy effective field theory for magnons and charge carriers was constructed for this case [25]. One can show that the charge carrier field $\psi_\pm(x)$ transforms as follows under the various symmetry operations

$$
\begin{aligned}
SU(2)_s: &\quad \psi_\pm(x)' = \exp(\pm i\alpha(x))\psi_\pm(x),\\
U(1)_Q: &\quad {}^Q\psi_\pm(x) = \exp(i\omega)\psi_\pm(x),\\
D: &\quad {}^D\psi_\pm(x) = \mp\exp(\mp i\varphi(x))\psi_\mp(x),\\
D': &\quad {}^{D'}\psi_\pm(x) = \pm\psi_\mp(x),\\
O: &\quad {}^O\psi_\pm(x) = \psi_\pm(Ox),\\
R: &\quad {}^R\psi_\pm(x) = \psi_\pm(Rx),\\
T: &\quad {}^T\psi_\pm(x) = \exp(\mp i\varphi(Tx))\psi^\dagger_\pm(Tx),\\
&\quad {}^T\psi^\dagger_\pm(x) = -\exp(\pm i\varphi(Tx))\psi_\pm(Tx),\\
T': &\quad {}^{T'}\psi_\pm(x) = -\psi^\dagger_\pm(Tx),\\
&\quad {}^{T'}\psi^\dagger_\pm(x) = \psi_\pm(Tx).
\end{aligned}
\tag{10.17}
$$

Again the Lagrangian has to be invariant under these symmetry transformations [25].

10.5 Low-Energy Effective Lagrangian

For all three locations of the pockets, low-energy effective field theories have been constructed. It is important to note that the low-energy physics described by the effective Lagrangians is quite different in each phase. To leading order, the Lagrangian in the pure magnon sector is the same in all three cases as described in chapter 3, because the pure magnon sector is the simply the undoped Heisenberg antiferromagnet and thus the parameters t and t' do not affect the system. However, the fermion fields are different. We will briefly describe the leading terms with two fermion fields $\mathcal{L}_2$ (containing at most one temporal or two spatial derivatives) describing the propagation of holes or electrons as well as their coupling to magnons.

10.5.1 Hole-Doped Antiferromagnet

The dispersion relation of hole-doped antiferromagnets shown in figure 10.2 has its minima at $(\pm\frac{\pi}{2a}, \pm\frac{\pi}{2a})$. By constructing an effective field theory one expands around these minima and must respect their symmetries. For the hole-doped antiferromagnets we obtain

$$
\begin{aligned}
\mathcal{L}_2 \;=\; & \sum_{f=\alpha,\beta}\,\sum_{s=+,-} \Big[M \psi_s^{f\dagger} \psi_s^f D_t \psi_s^f + \frac{1}{2M'} D_i \psi_s^{f\dagger} D_i \psi_s^f \\
+ \; & \sigma_f \frac{1}{2M''} \left(D_1 \psi_s^{f\dagger} D_2 \psi_s^f + D_2 \psi_s^{f\dagger} D_1 \psi_s^f \right) + \Lambda \left(\psi_s^{f\dagger} v_1^s \psi_{-s}^f + \sigma_f \psi_s^{f\dagger} v_2^s \psi_{-s}^f \right) \\
+ \; & N_1 \psi_s^{f\dagger} v_i^s v_i^{-s} \psi_s^f + \sigma_f N_2 \left(\psi_s^{f\dagger} v_1^s v_2^{-s} + \psi_s^{f\dagger} v_2^s v_1^{-s} \psi_s^f \right) \Big].
\end{aligned}
\tag{10.18}
$$

Here the fermion-fields carry spin $s \in \{+,-\}$ and flavour $f \in \{\alpha, \beta\}$, which corresponds to two types of hole-pockets α corresponding to $\{(\frac{\pi}{2a}, \frac{\pi}{2a}), (-\frac{\pi}{2a}, -\frac{\pi}{2a})\}$ and β corresponding to $\{(\frac{\pi}{2a}, -\frac{\pi}{2a}), (-\frac{\pi}{2a}, \frac{\pi}{2a})\}$. The two effective masses M' and M'' are due to the elliptical pocket-shapes. The constants M, M', and M'' have been measured with the method presented in the next chapter in [108]. Furthermore, Λ is a hole-one-magnon and N_1 and N_2 are hole-two-magnon couplings, which all take real values. With the linear coupling Λ of magnons to the holes it is possible for spiral phases to emerge as discussed in [109]. The determination of Λ is more complicated and a matter of current research. The sign σ_f is $+$ for $f = \alpha$ and $-$ for $f = \beta$. The full construction is discussed in [24].

10.5.2 Electron-Doped Antiferromagnet

Because upon electron doping the pockets are located in different positions, the low-energy effective Lagrangian now takes the form [26]

$$\begin{aligned}\mathcal{L}_2 &= \sum_{s=+,-}\Big[M\psi_s^\dagger\psi_s + \psi_s^\dagger D_t\psi_s + \frac{1}{2M'}D_i\psi_s^\dagger D_i\psi_s + N\psi_s^\dagger v_i^s v_i^{-s}\psi_s \\ &+ iK\left(D_1\psi_s^\dagger v_1^s\psi_{-s} - \psi_s^\dagger v_1^s D_1\psi_{-s} - D_2\psi_s^\dagger v_2\psi_{-s} + \psi_s^\dagger v_2^s D_2\psi_{-s}\right)\Big]. \end{aligned} \tag{10.19}$$

Here, due to the circular pocket shape there is no M''-term. Also there is no Λ-term, i.e. a weaker magnon-electron coupling, and thus no spiral phases emerge.

10.5.3 Charge Carriers at $(0,0)$ and $(\frac{\pi}{a},\frac{\pi}{a})$

The first fully systematic effective field theory for magnons and charge carriers was of this type [25]. It seems not to correspond to a real material but is still of theoretical interest

$$\begin{aligned}\mathcal{L}_2 &= \sum_{s=+,-}\Big[M\psi_s^\dagger\psi_s + \psi_s^\dagger D_t\psi_s + \frac{1}{2M'}D_i\psi_s^\dagger D_i\psi_s + N\psi_s^\dagger v_i^s v_i^{-s}\psi_s + \Lambda\psi_s^\dagger v_t^s\psi_{-s} \\ &+ iK\left(D_i\psi_s^\dagger v_i^s\psi_{-s} - \psi_s^\dagger v_i^s D_i\psi_{-s}\right) + \frac{G}{2}\psi_s^\dagger\psi_s\psi_{-s}^\dagger\psi_{-s}\Big]. \end{aligned} \tag{10.20}$$

Again there is no linear magnon-charge-carrier coupling. Thus again the coupling of the magnons to the charge carriers is weaker than in the case of the hole-doped antiferromagnets. The construction is discussed in detail in [25].

10.6 The Two-Point Correlation Function

If we want to calculate the dispersion relation, we have to measure the two-point correlation function

$$G(x,t) = \langle c_{0,0}^\dagger c_{x,t}\rangle = \frac{1}{Z_{Q=0}}\mathrm{Tr}_{Q=0}\left[c_{0,0}^\dagger\exp(-tH)c_{x,t}\exp\left(-(\beta-t)H\right)\right]. \tag{10.21}$$

Here $Q=0$ denotes measurements at half-filling. We can express this two-point correlation function as a reweighting of the Boltzmann weights in the $Q=0$ sector with the paths of the created and annihilated charge carrier

$$\begin{aligned}G(x,t) &= \frac{1}{Z_{Q=0}}\mathrm{Tr}_{Q=0}\left[\frac{c_{0,0}^\dagger\exp(-tH)c_{x,t}\exp\left(-(\beta-t)H\right)}{\exp(-\beta H)}\exp(-\beta H)\right] \\ &= \left\langle\frac{c_{0,0}^\dagger\exp(-tH)c_{x,t}\exp\left(-(\beta-t)H\right)}{\exp(-\beta H)}\right\rangle_{Q=0}. \end{aligned} \tag{10.22}$$

Thus we do not have to directly simulate a hole-doped antiferromagnet, but can run a simulation of a Heisenberg antiferromagnet and measure the propagation of doped holes by calculating a reweighing of the hole-paths inserted into the the configurations of the undoped Heisenberg antiferromagnet.

This can be done by choosing a hole path according to its weight and by calculating the ratio to the undoped background. However, this is not very efficient. Rather we simultaneously measure all possible hole paths extending from $(0,0)$ to (x,t). This procedure is described in detail in [108].

10.7 Fitting Energies in Momentum-Space

The measured correlation functions are then transformed to momentum space using

$$c_p^\dagger = \sum_x c_x^\dagger \exp(ipx), \quad c_p = \sum_x c_x \exp(-ipx). \tag{10.23}$$

As the Hamiltonian H is translation invariant, every energy eigenstate can be chosen as a momentum eigenstate. As $c_p^\dagger$ raises the momentum k_m of the energy eigenstate $|m\rangle$ by p, the energy eigenstate $|n\rangle$ needs to have the momentum $k_m + p$ in order to receive a non-vanishing contribution from $\langle m|c_p|n\rangle$

$$\begin{aligned}\widetilde{G}(p,t) &= \frac{1}{Z_{Q=0}} \sum_{n,m} \left|\langle n|c_p^\dagger|m\rangle\right|^2 \exp\left(-tE_m\right) \exp\left(-(\beta - t)E_n\right) \\ &= \frac{\sum_{n,m} \left|\langle n|c_p^\dagger|m\rangle\right|^2 \exp\left(-tE_m\right) \exp\left(-(\beta - t)E_n\right)}{\sum_k \exp\left(-\beta E_k\right)} \qquad (10.24) \\ \lim_{\beta\to\infty} \widetilde{G}(p,t) &= \sum_m \left|\langle 0|c_p^\dagger|m\rangle\right|^2 \exp\left(-t(E_m - E_0)\right). \qquad (10.25)\end{aligned}$$

By taking the limit $\beta \to \infty$, only the contribution from $E_1 - E_0$ is left. Thus the energy spectrum can be extracted from the two-point correlation function in momentum space.

In practice one has to be very careful how to fit these correlation functions. Either one fits $\widetilde{G}(p,t)$ only at sufficiently large t where all energies except E_1 are suppressed with just one exponential or one fits it to two or more exponentials. Because the errors usually increase with increasing t the fitting range has to be carefully chosen and affects the result with a systematic error.

10.8 Fitting Mass Parameters

The mass parameters of the hole-doped system M, M', M'' in eq. (10.18) can be extracted, by fitting the dispersion relation around the centers of the pockets to

$$E(p_1,p_2) = M + \frac{p_1^2 + p_2^2}{2M'} + \frac{p_1 p_2}{M''}. \tag{10.26}$$

The determination of the mass parameters M, M', and M'' has been performed in [108]. To obtain the mass parameters of the electron-doped system, as well as the mass parameters in the case where the pockets are centered at $(0,0)$ and $(\frac{\pi}{a},\frac{\pi}{a})$ — M and M' in eqs. (10.19) and (10.20) — it is sufficient to fit the dispersion relation around the center of the pockets to

$$E(p_1,p_2) = M + \frac{p_1^2+p_2^2}{2M'} = M + \frac{|\vec{p}|^2}{2M'}. \tag{10.27}$$

We will discuss this calculation specifically for the honeycomb lattice in the next chapter.

The fitting of the mass parameters is a somewhat tricky business, because we fit the results of a fit. The energies in the dispersion relation are the result of the fits of the two-point correlation functions. Thus the choice of fitting range of the fit of the exponentials in section 10.7 also affects the shape of the dispersion relation. Furthermore, also a fitting range around the center of the pocket has to be chosen and systematically affects the fit.

We thus usually fit both the exponentials and the resulting dispersion relations with different fitting ranges in order to get a good error estimate that includes the systematics.

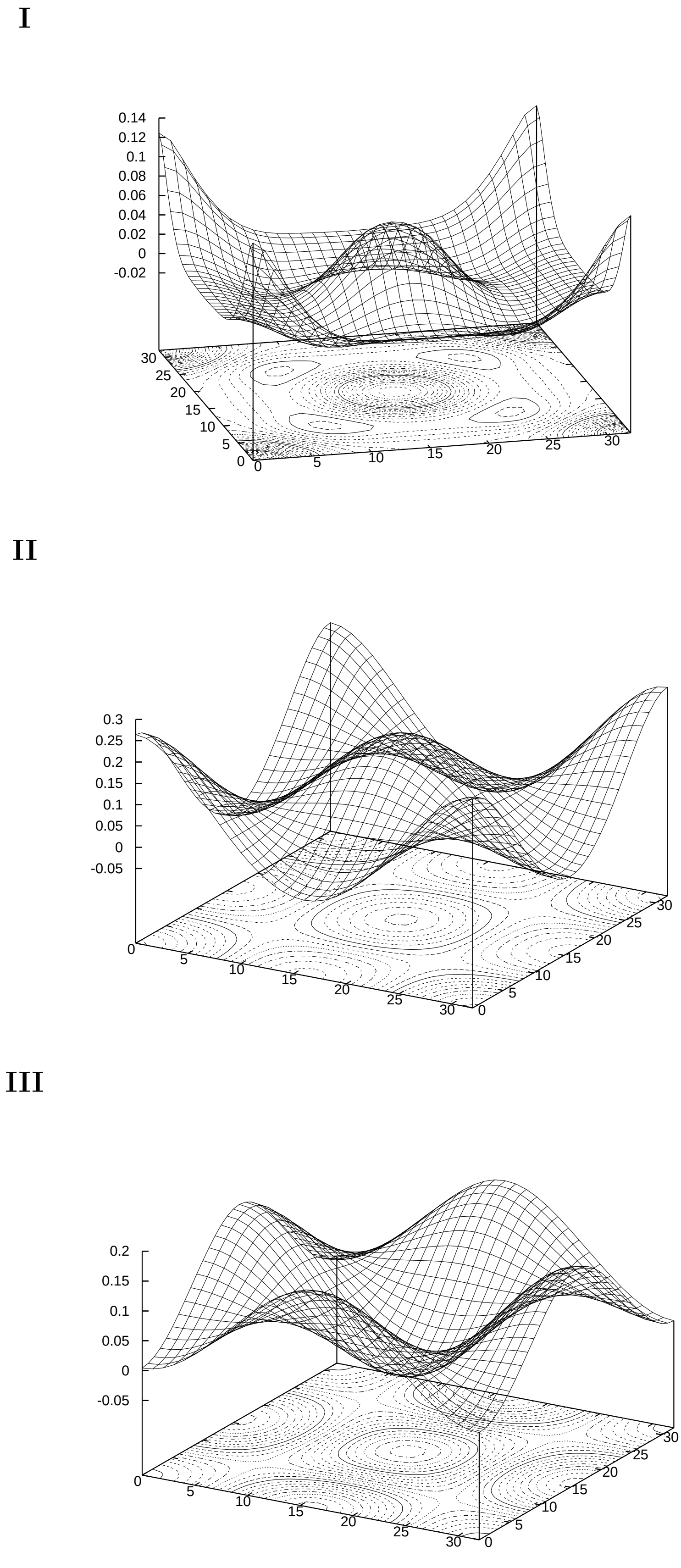

Figure 10.1: *The three different dispersion relations measured on a* 32^2 *lattice.*

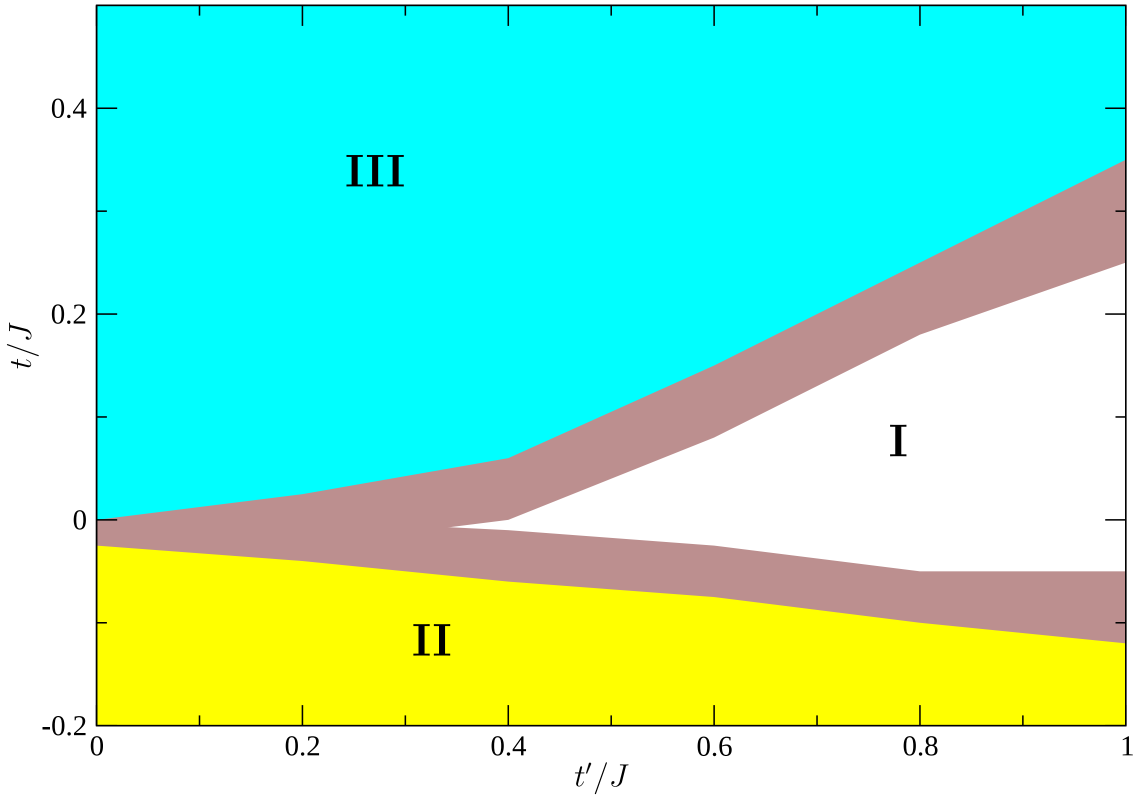

Figure 10.2: *The three different dispersion relations in 10.1 in the* t/J-t'/J *parameter space. This calculation was performed at low temperature* ($\beta J = 80$)*. The dark area marks the uncertainty of the region where the transition between the qualitatively different dispersion relations occur.*

Chapter 11

The t-J Model on the Honeycomb Lattice and its Low-Energy Effective Field Theory

After simulating the pure magnon sector of a Heisenberg model on the honeycomb lattice in chapter 4, we are also interested in the single-hole dispersion relation of such a system, i.e. in the t-J model on the honeycomb lattice.

As we have shown in the last chapter, the single-hole dispersion relation can be calculated by simulating the one-hole sector of the t-J model and by calculating the relevant correlation functions. Of course, we can also do this on the honeycomb lattice. The work presented in this chapter has been published in [7].

11.1 Brillouin Zone of a Honeycomb Lattice

The honeycomb lattice consists of two triangular Bravais sublattices A and B. The Brillouin zone of the honeycomb lattice is doubly-covered with two covers A and B. The two covers correspond to the two triangular Bravais sublattices A and B as shown in figure 4.1a in chapter 4. The Brillouin zone then takes the form shown in figure 11.1.

11.2 Fermion Dispersion Relation for the t-J Model on the Honeycomb Lattice

It is necessary to distinguish the correlation functions between the sublattices, i.e. AA, AB, BA, BB. The correlation function between AA sublattices with momentum k takes

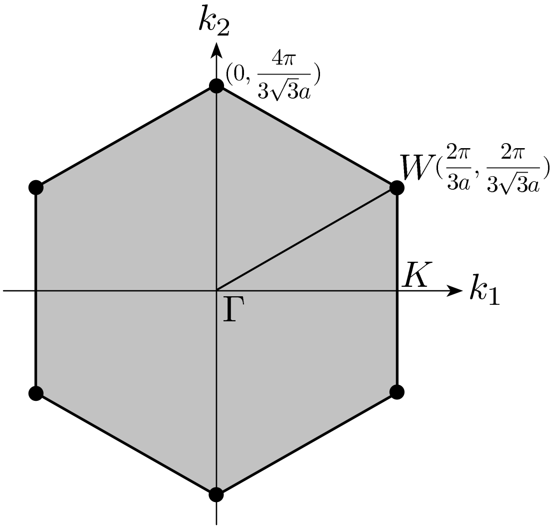
k_2
$(0, \frac{4\pi}{3\sqrt{3}a})$
$W(\frac{2\pi}{3a}, \frac{2\pi}{3\sqrt{3}a})$
K
k_1
Γ

Figure 11.1: *The momentum space of a honeycomb lattice, which is a doubly-covered Brillouin zone dual to the two triangular sublattices A and B.*

the form

$$\begin{aligned} G^{AA}(k,t) &= \frac{1}{Z}\sum_{x,y\in A} \mathrm{Tr}\left[c_x^\dagger(0)c_y(t)\exp(-\beta H)\right]\exp(-ik(x-y)) \\ &\sim \sum_{n=1}^{\infty} Z_n(k)\exp\left(-(E_n(k)-E_0)t\right), \end{aligned} \tag{11.1}$$

where E_0 is the ground state energy of the half-filled system, and

$$Z_n(k) = |\langle 0|\sum_{x\in A} c_x \exp(ikx)|n\rangle|^2. \tag{11.2}$$

The factor $Z_1(k)$ is known as the quasiparticle weight. In deriving eq. (11.1), we have inserted a complete set of energy eigenstates $\mathbb{1} = \sum_n |n\rangle\langle n|$ in the single-hole sector and taken the limit $\beta \to \infty$ in the final step. The fermion energy

$$E_h(k) = E_1(k) - E_0 \tag{11.3}$$

corresponding to the momentum k can be extracted by fitting the data to a single- or a double-exponential. The correlation function between AA sublattices with momentum $k = (\frac{2\pi}{3a}, \frac{2\pi}{3\sqrt{3}a})$ depicted in figure 11.2 has been obtained on a honeycomb lattice with 3456 spins and $J/t = 2.0$. A single-exponential fit yields $E_h(k) = 0.207(9)t$ while a double-exponential fit results in $E_h(k) = 0.201(5)t$. The two fits yield consistent results. In the same way, we determine the one-hole dispersion relation from the AA correlator for all momenta k. The single-hole dispersion relation in figure 11.3 has been obtained with the

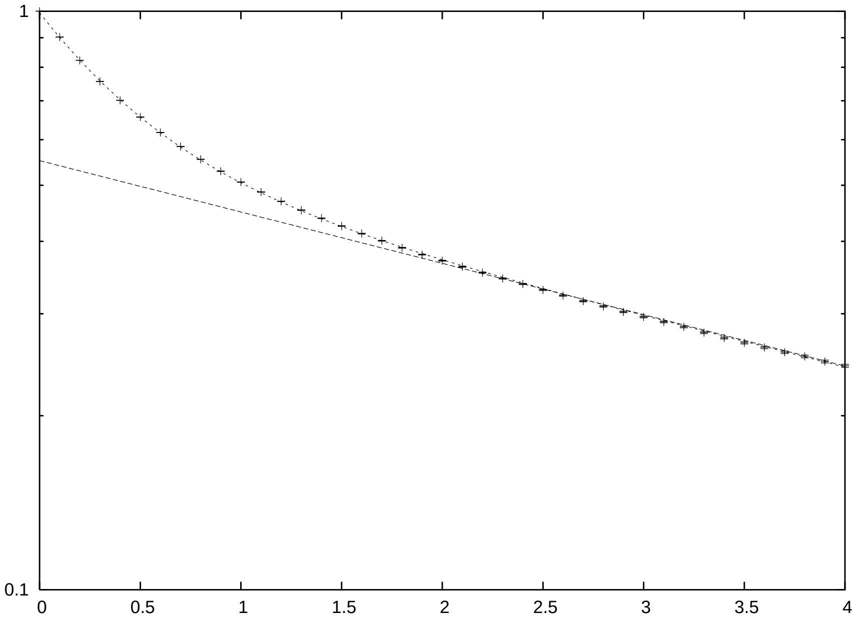

Figure 11.2: *Correlation function $G^{AA}(k,t)$ between AA sublattices with Fourier momentum $k=(\frac{2\pi}{3a},\frac{2\pi}{3\sqrt{3}a})$. The bottom line is the result of a single-exponential fit while the top line is obtained from a double-exponential fit.*

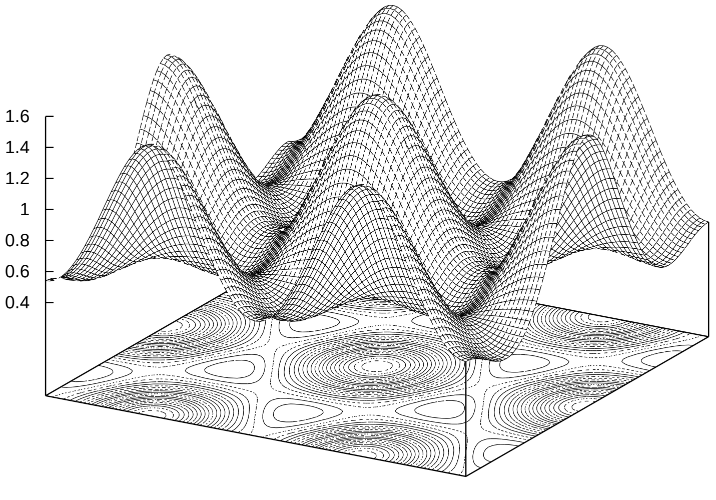

Figure 11.3: *The dispersion relation $E_h(k)/t$ for a single hole in an antiferromagnet on the honeycomb lattice.*

same parameters as in figure 11.2. The figure shows that the hole pockets are located at $(\pm\frac{2\pi}{3a}, \pm\frac{2\pi}{3\sqrt{3}a})$ and $(0, \pm\frac{4\pi}{3\sqrt{3}a})$ in the Brillouin zone. The position of the hole pockets agrees with the position of the Dirac cones obtained from the free fermion theory on the honeycomb lattice which is relevant for graphene.

11.3 Effective Field Theory for Holes and Magnons

The effective Lagrangian on the honeycomb lattice in [110] was constructed in the same manner as for the square lattice in [24]. Using the information about the location of the pockets and based on the symmetry properties of the underlying microscopic theory, a systematic low-energy effective theory for the t-J model on the honeycomb lattice was constructed. Here we briefly sketch the principles behind this construction. In the effective theory, the holes reside in momentum space pockets centred at

$$k^{\alpha} = (0, \frac{4\pi}{3\sqrt{3}a}),\ k^{\beta} = (0, -\frac{4\pi}{3\sqrt{3}a}). \tag{11.4}$$

Here the "flavour" index $f = \alpha, \beta$ characterises the corresponding hole pocket and the index $s = \pm$ denotes spin parallel $(+)$ or anti-parallel $(-)$ to the local staggered magnetisation. The magnons are coupled to the holes through a nonlinear realisation of the spontaneously broken $SU(2)_s$ symmetry. The global $SU(2)_s$ symmetry then manifests itself as a local $U(1)_s$ symmetry in the unbroken subgroup. This construction again leads to an Abelian "gauge" field $v_\mu^3(x)$ and to two vector fields $v_\mu^\pm(x)$ which are "charged" under $U(1)_s$ spin transformations. The coupling of magnons and holes is realised through $v_\mu^3(x)$ and $v_\mu^\pm(x)$. These fields have a well-defined transformation behaviour under the symmetries which the effective theory inherits from the underlying microscopic models.

11.3.1 Magnon- and Hole-Field Symmetry-Transformations on a Honeycomb Lattice

In the same way as shown in chapter 10 these magnon fields v_μ have a well-defined transformation behaviour under the symmetries which the effective theory inherits from the underlying microscopic t-J model on the honeycomb lattice [110]

$$
\begin{aligned}
SU(2)_s: \quad & v_\mu(x)' = h(x)(v_\mu(x) + \partial_\mu)h(x)^\dagger, \\
D_i: \quad & {}^{D_i}v_\mu(x) = v_\mu(x), \\
O: \quad & {}^{O}v_1(x) = \tau(Ox)\big(\tfrac{1}{2}v_1(Ox) + \tfrac{\sqrt{3}}{2}v_2(Ox) \\
& \qquad + \tfrac{1}{2}\partial_1 + \tfrac{\sqrt{3}}{2}\partial_2\big)\tau(Ox)^\dagger, \\
& {}^{O}v_2(x) = \tau(Ox)\big(- \tfrac{\sqrt{3}}{2}v_1(Ox) + \tfrac{1}{2}v_2(Ox) \\
& \qquad - \tfrac{\sqrt{3}}{2}\partial_1 + \tfrac{1}{2}\partial_2\big)\tau(Ox)^\dagger, \\
& {}^{O}v_t(x) = \tau(Ox)(v_t(Ox) + \partial_t)\tau(Ox)^\dagger, \\
R: \quad & {}^{R}v_1(x) = v_1(Rx), \quad {}^{R}v_2(x) = -v_2(Rx), \\
& {}^{R}v_t(x) = v_t(Rx), \\
T: \quad & {}^{T}v_i(x) = \tau(Tx)(v_i(Tx) + \partial_i)\tau(Tx)^\dagger, \\
& {}^{T}v_t(x) = -\tau(Tx)(v_t(Tx) + \partial_t)\tau(Tx)^\dagger,
\end{aligned} \tag{11.5}
$$

where D_i, with $i \in \{1, 2\}$, are the displacements along primitive translation vectors which are chosen to be $a_1 = (\frac{3}{2}a, \frac{\sqrt{3}}{2}a)$ and $a_2 = (0, \sqrt{3}a)$, respectively. Here a is the lattice spacing. Further, O, R, and T in eq. (11.5) represent a 60 degrees spatial rotation around the center of a hexagon, a spatial reflection with respect to the x-axis, and time reversal, which are given by

$$
\begin{aligned}
Ox &= O(x_1, x_2, t) = (\tfrac{1}{2}x_1 - \tfrac{\sqrt{3}}{2}x_2, \tfrac{\sqrt{3}}{2}x_1 + \tfrac{1}{2}x_2, t), \\
Rx &= R(x_1, x_2, t) = (x_1, -x_2, t), \\
Tx &= T(x_1, x_2, t) = (x_1, x_2, -t),
\end{aligned} \tag{11.6}
$$

respectively.

The hole fields are represented by Grassmann fields $\psi^f_s(x)$. Under the various symmetry operations the hole fields transform as [110]

$$
\begin{aligned}
SU(2)_s: \quad & \psi^f_\pm(x)' = \exp(\pm i\alpha(x))\psi^f_\pm(x), \\
U(1)_Q: \quad & {}^{Q}\psi^f_\pm(x) = \exp(i\omega)\psi^f_\pm(x), \\
D_i: \quad & {}^{D_i}\psi^f_\pm(x) = \exp(ik^f_i a_i)\psi^f_\pm(x), \\
O: \quad & {}^{O}\psi^\alpha_\pm(x) = \mp\exp(\mp i\varphi(Ox) \pm i\tfrac{2\pi}{3})\psi^\beta_\mp(Ox), \\
& {}^{O}\psi^\beta_\pm(x) = \mp\exp(\mp i\varphi(Ox) \mp i\tfrac{2\pi}{3})\psi^\alpha_\mp(Ox), \\
R: \quad & {}^{R}\psi^\alpha_\pm(x) = \psi^\beta_\pm(Rx), \qquad {}^{R}\psi^\beta_\pm(x) = \psi^\alpha_\pm(Rx), \\
T: \quad & {}^{T}\psi^\alpha_\pm(x) = \exp(\mp i\varphi(Tx))\psi^{\beta\dagger}_\pm(Tx), \\
& {}^{T}\psi^\beta_\pm(x) = \exp(\mp i\varphi(Tx))\psi^{\alpha\dagger}_\pm(Tx), \\
& {}^{T}\psi^{\alpha\dagger}_\pm(x) = -\exp(\pm i\varphi(Tx))\psi^\beta_\pm(Tx), \\
& {}^{T}\psi^{\beta\dagger}_\pm(x) = -\exp(\pm i\varphi(Tx))\psi^\alpha_\pm(Tx).
\end{aligned} \tag{11.7}
$$

Here $U(1)_Q$ is the fermion number symmetry of the holes. Interestingly, in the effective continuum theory the location of holes in lattice momentum space manifests itself as a "charge" k_i^f under the displacement symmetry D_i.

11.3.2 Effective Lagrangian

Based on symmetry considerations, the leading order terms of the effective Lagrangian were constructed for magnons and holes on the honeycomb lattice in [110]. In analogy to the Lagrangians in chapter 10, the leading terms with two fermion fields (containing at most one temporal or two spatial derivatives) are given by

$$\begin{aligned}\mathcal{L}_2 \;=\; \sum_{\substack{f=\alpha,\beta \\ s=+,-}} \Big[& M\psi_s^{f\dagger}\psi_s^f + \psi_s^{f\dagger}D_t\psi_s^f + \frac{1}{2M'}D_i\psi_s^{f\dagger}D_i\psi_s^f + \Lambda\psi_s^{f\dagger}(isv_1^s + \sigma_f v_2^s)\psi_{-s}^f \\ & +iK\big[(D_1 + is\sigma_f D_2)\psi_s^{f\dagger}(v_1^s + is\sigma_f v_2^s)\psi_{-s}^f - (v_1^s + is\sigma_f v_2^s)\psi_s^{f\dagger}(D_1 + is\sigma_f D_2)\psi_{-s}^f\big] \\ & \sigma_f L\psi_s^{f\dagger}\epsilon_{ij}f_{ij}^3\psi_s^f + N_1\psi_s^{f\dagger}v_i^s v_i^{-s}\psi_s^f + is\sigma_f N_2\big(\psi_s^{f\dagger}v_1^s v_2^{-s}\psi_s^f - \psi_s^{f\dagger}v_2^s v_1^{-s}\psi_s^f\big)\Big]. \end{aligned} \tag{11.8}$$

Here M is the rest mass and M' is the kinetic mass of a hole, while D_μ is a covariant derivative given by

$$D_\mu\psi_\pm^f(x) \;=\; [\partial_\mu \pm iv_\mu^3(x)]\;\psi_\pm^f(x)\,. \tag{11.9}$$

Eq. (11.8) yields circular hole pockets for small momenta which is indeed confirmed in figure 11.4.

The low-energy constant M' in eq. (11.8) is obtained from the curvature of the dispersion $E_h(k)$ near a minimum by fitting the dispersion relation around the circular centers of the hole-pockets

$$E(p_1, p_2) = M + \frac{p_1^2 + p_2^2}{2M'} = M + \frac{|\vec{p}|^2}{2M'}. \tag{11.10}$$

. For example, on a honeycomb lattice with 3456 spins and $J/t = 2.0$, we find $M' = 4.1(1)/(ta^2)$.

In figures 11.5 and 11.6, we have plotted the single-hole dispersion as well as the quasiparticle weight $Z_1(k)$ over the irreducible wedge Γ-K-W-Γ of the Brillouin zone for $J/t = 1.0$. The resulting bandwidth

$$\Delta = E_h(\Gamma) - E_h(W) \tag{11.11}$$

is in qualitative agreement with exact diagonalisation and series expansion in [111]. While exact diagonalisation of small systems may suffer from finite size effects, and series expansions may not converge in all regions of parameter space, the Monte Carlo data obtained with the efficient loop-cluster algorithm do not suffer from systematic uncertainties. In table 2 we list the kinetic mass M' as well as the bandwidth Δ for a few values of J/t.

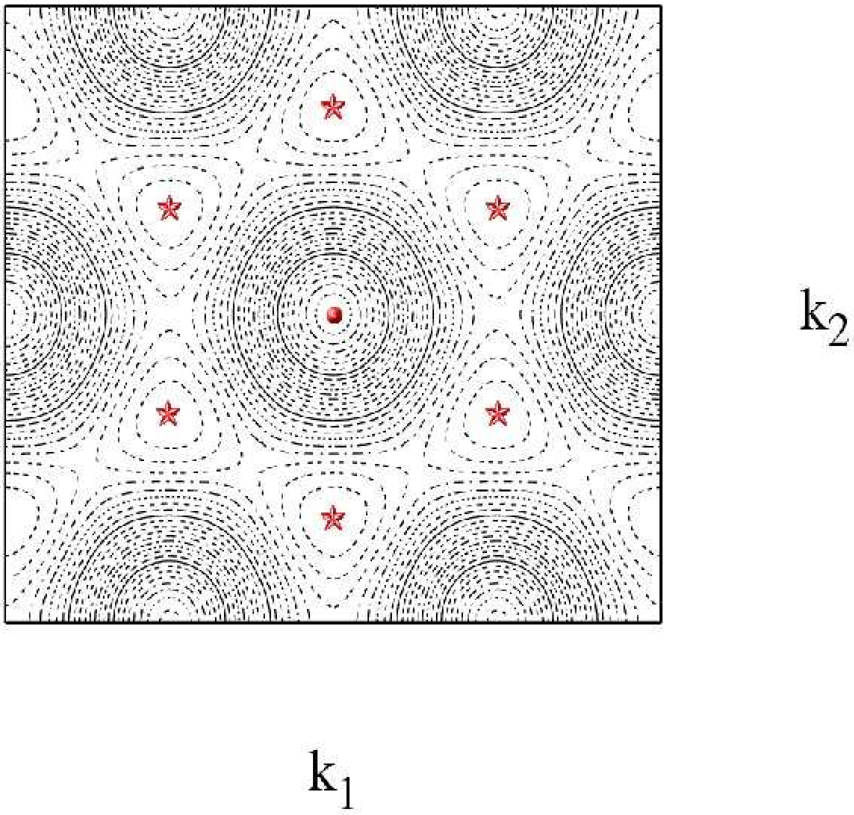

Figure 11.4: *Circular hole pockets on the honeycomb lattice. The dot corresponds to the point* Γ *and the stars mark the centres of the hole pockets (corresponding to the point* W *and its symmetry partners). The parameters are the same as in figure 11.3.*

J/t	$M'ta^2$	Δ/t
2.0	4.1(1)	1.15(3)
1.5	2.9(1)	1.25(3)
1.0	1.9(1)	1.24(4)
0.9	1.8(1)	1.15(6)
0.6	1.5(2)	0.9(1)

Table 11.1: *Kinetic mass M' as well as the bandwidth Δ for some values of J/t.*

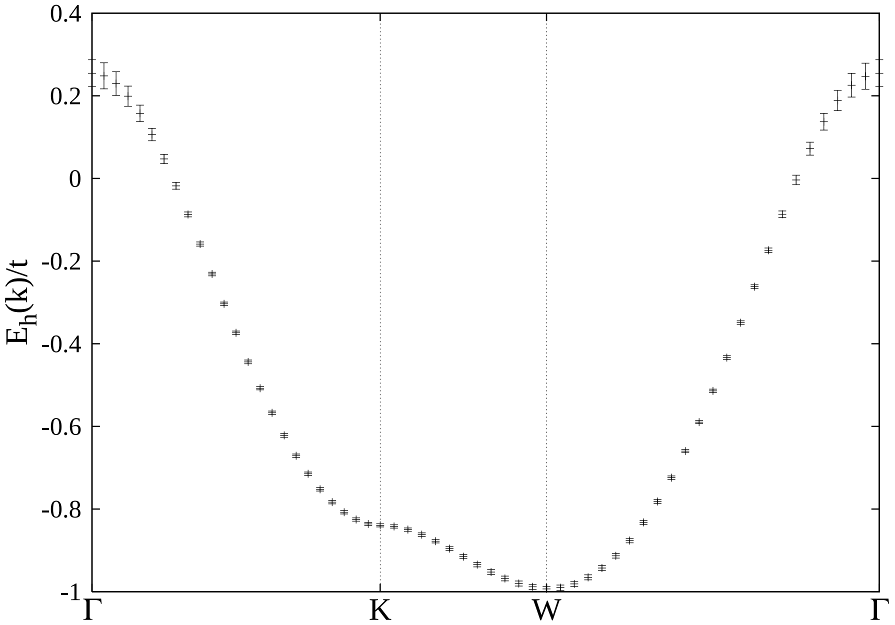

Figure 11.5: *Dispersion relation $E_h(k)/t$ of a single hole for $J/t = 1.0$ along the irreducible wedge Γ-W-K-Γ in the first Brillouin zone (see figure 2).*

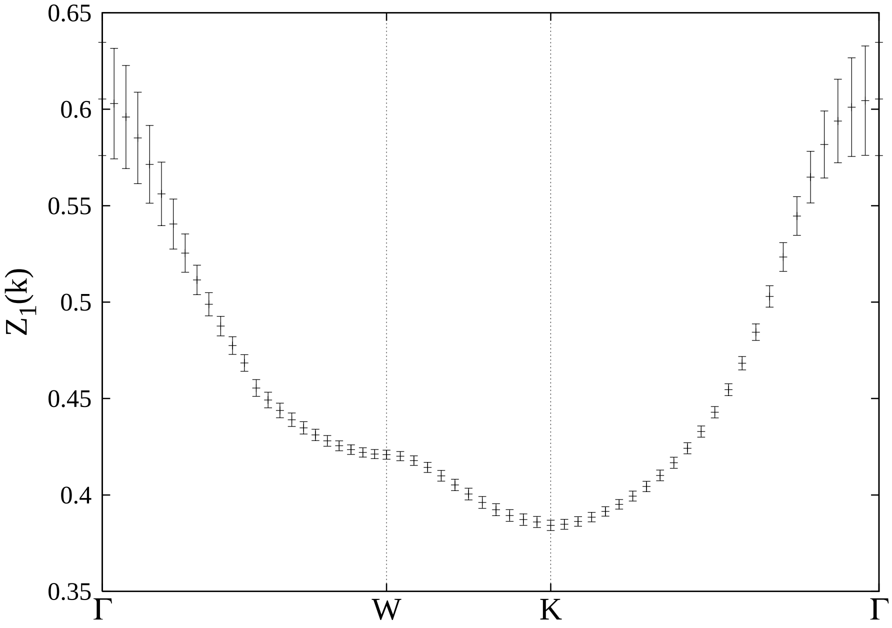

Figure 11.6: *The quasiparticle weight* $Z_1(k)$ *of a single hole for* $J/t = 1.0$ *along the irreducible wedge* Γ-W-K-Γ *in the first Brillouin zone (see figure 2).*

Conclusions and Outlook

In this thesis we have approached the quantum Heisenberg model and some of its extensions with quantum Monte Carlo calculations. In the first part of the thesis we investigated lattice structures, for which spontaneous symmetry breaking occurs. In these cases a low-energy effective field theory approach is applicable.

We have simulated on the honeycomb lattice and numerically calculated the low-energy parameters in the magnon-sector to high precision. This was done by fitting low-energy effective field theory calculations at finite volume and temperature to Monte Carlo data.

The same kind of calculations were performed for a Heisenberg model with spatially anisotropic couplings using the loop-cluster algorithm. The corresponding low-energy constants are determined with high precision. Further, the J_2/J_1-dependence of ρ_{s1} and ρ_{s2} is investigated in detail and our results agree quantitatively with those obtained by series expansion in the weakly anisotropic regime. In the extreme anisotropic limit, the two-dimensional system decomposes into decoupled spin chains. Thus, dimensional cross-over is observed which gives rise to a fascinating phase transition. By fitting our (not unbiased) data we get a universal scaling behaviour distinct from the $O(3)$ university class. Hence, this transition could possibly belong to a new university class. Further investigations on the physics of this phase transition are highly desirable which should give us more insight on the exact values of the universal scaling parameters and the physics of dimensional cross-over.

Furthermore, we used these techniques to investigate a spin $\frac{1}{2}$ quantum Heisenberg antiferromagnet with an additional four-spin interaction, the J-Q model using the loop-cluster algorithm. We quantitatively observed the expected weakening of antiferromagnetism as the coupling of the four-spin interaction Q is increased. Using finite-size scaling and the flowgram method we investigated the phase transition between the antiferromagnetic and the valence bond solid (VBS) phase. Unlike previous studies we conclude that the transition is weakly first order, based on our numerical evidence, thus confirming the Ginzburg-Landau-Wilson paradigm. It is interesting to ask, why the phase transition separating antiferromagnetism and the valence bond solid is so weakly first order. There must be a reason for the long correlation length, around 50 lattice spacings, even if it does not go to infinity. Also we used quantum Monte Carlo methods to simulate deep in the VBS phase. As we observed an emerging $U(1)$ symmetry we could not make a clear statement about the nature of the VBS order. It would be desirable to extend these numerical investigations to even larger lattices in order to make the statement about the nature of the phase transition with more certainty and to see if the emergent $U(1)$ symmetry is due to finite size effects.

In the second part of the thesis we have investigated the antiferromagnetic Heisenberg model on frustrated lattices. We have introduced a new method for the simulation of frustrated spin systems — the nested cluster algorithm — which works for substantially larger systems than possible before, at least at moderate temperatures. We can measure the expectation value of the sign, which is exponentially suppressed, with a polynomial time effort at least down to a certain temperature range with a good error estimate. In contrast to other Monte Carlo methods, the nested cluster algorithm is capable of eliminating very severe sign problems for large systems, at least at moderate temperatures. As we have demonstrated, by studying appropriate susceptibilities one may obtain valuable insights concerning possible types of order.

In this method, there is a lot of fine-tuning involved. The parameters that tune the performance of the algorithm have to be determined for each frustrated system individually. This method has to be refined in order to proceed to lower temperatures. One could possibly further cut the clusters involved and apply a multi-level scheme. This should hopefully make the algorithm work at lower temperature than possible today. Also it would be interesting to use this method on other frustrated system, e.g. spin-glasses to see how the efficiency of the method depends on the underlying system.

Also we want to understand the physical meaning of the cluster size. We suspect that they are some measure of quantum entanglement which should be further investigated.

Also the method could be adapted to real-time evolution which, however, turned out not to be very efficient. Still, we were able to show that with the nested algorithm we can in principle perform measurements of the real-time evolution of quantum spin systems. The complex phases that occur can be factorised to the clusters and inner Monte Carlo updates can be performed in a very similar way as on the frustrated lattices.

In the third part of the thesis we finally considered the t-t'-J model on the square lattice in the single-hole sector. By tuning the hopping parameters t and t' the model corresponds to hole- or electron-doped materials or even to a dispersion relation which seems not to correspond to any existing material. The phase diagram in terms of these three distinct phases was determined, while there is some uncertainty in the location of the transition lines. Further numerical investigations would narrow the uncertainty of these transition lines. Also it would be interesting to investigate how a further hopping term would change the dispersion relation.

We also performed the same kind of simulations on the honeycomb lattice to calculate the single-hole dispersion and extracted the low-energy effective mass parameters. In particular, we have fitted more than hundred Monte Carlo data obtained at rather different volumes and temperatures with just four low-energy parameters — $\mathcal{M}_s$, ρ_s, c, and M' — of the effective theory for the t-J model. These parameters have been determined with percent and sometimes even with permille accuracy. This should demonstrate convincingly that the systematic low-energy effective field theory yields quantitatively correct results for the physics of magnons and holes.

In all three parts there is a lot of on-going research. The search for more numerical evidence to investigate and determine exotic phase transitions, the search for more efficient algorithms and the quest of dealing with sign problems, as well as the challenge of determining further low-energy parameters is a thrilling and challenging subject and we are looking forward to see and hopefully contribute to progress in this field of numerical work.

> Friendship is unnecessary, like philosophy, like art, like the universe itself. It has no survival value; rather it is one of those things which give value to survival.
>
> Clive Staples Lewis

Acknowledgments

First of all, I want to thank Uwe-Jens Wiese on whose red sofa I have spent many hours for his patience and support and all the important insight I learned from him. Also it was a pleasure to work with Florian Kämpfer, Fu-Jiun Jiang, Urs Gerber and Christoph Hofmann on various subjects where I was glad to be embeded in good teams.

Also many thanks to Esther Fiechter for her professional support. Of course I must not forget Ottilia Hänni who whose glorious wit made us enjoying academic life live at our institute.

I would like to thank Markus Moser on whose professional companionship I could always count on and Allessio Vaghi for the laughter he brought to our office.

In particular I am full of gratitude for the friendship, non-physical discussion, wonderful musical sessions, and joyful lunch breaks with Stefan Lanz, Lorenzo Mercolli, Christof Schüpbach, Vidushi Maillard and everybody else on the B-floor. You gave value to my survival.

Gratitude I also owe to Lorenz Hausser, Simon Zwygart, and René Schafroth my friends and neighbours and I am also deeply greatful to Manuel Jordi for all the discussions, music and time he shared with me during the last few years. You contributed a lot in between the lines.

And a last a big thankyou goes to my family, my brothers, Thomas and Andreas and his family — your kids are invaluable to me —, and my dear parents Gottfried and Ursula Nyfeler for their love and support.

Appendix A

Loop-Cluster Algorithm for the J-Q-Model

In this Appendix, we will briefly describe the loop cluster algorithm for the J-Q-Model, i.e. the Heisenberg Model with the additional four-spin interaction Q as described in chapter 6. It follows the same procedure as discussed in chapter 2. We will only discuss the method in discrete time, but as shown above it can easily be adapted to the continuous-time path integral formulation or to the stochastic series expansion (SSE).

A.1 12-Step Suzuki-Trotter Decomposition

The simplest possible decomposition of the Hamiltonian 6.1 is

$$\begin{aligned}
H_1 &= J \sum_{x\in(2m,n)} \vec{S}_x \cdot \vec{S}_{x+\hat{1}},\ H_2 = J \sum_{x\in(m,2n)} \vec{S}_x \cdot \vec{S}_{x+\hat{2}}, \\
H_3 &= J \sum_{x\in(2m+1,n)} \vec{S}_x \cdot \vec{S}_{x+\hat{1}},\ H_4 = J \sum_{x\in(m,2n+1)} \vec{S}_x \cdot \vec{S}_{x+\hat{2}}, \\
H_5 &= -Q \sum_{x\in(2m,2n)} (\vec{S}_x \cdot \vec{S}_{x+\hat{1}} - \frac{1}{4})(\vec{S}_{x+\hat{2}} \cdot \vec{S}_{x+\hat{1}+\hat{2}} - \frac{1}{4}), \\
H_6 &= -Q \sum_{x\in(2m+1,2n)} (\vec{S}_x \cdot \vec{S}_{x+\hat{1}} - \frac{1}{4})(\vec{S}_{x+\hat{2}} \cdot \vec{S}_{x+\hat{1}+\hat{2}} - \frac{1}{4}), \\
H_7 &= -Q \sum_{x\in(2m,2n+1)} (\vec{S}_x \cdot \vec{S}_{x+\hat{1}} - \frac{1}{4})(\vec{S}_{x+\hat{2}} \cdot \vec{S}_{x+\hat{1}+\hat{2}} - \frac{1}{4}), \\
H_8 &= -Q \sum_{x\in(2m+1,2n+1)} (\vec{S}_x \cdot \vec{S}_{x+\hat{1}} - \frac{1}{4})(\vec{S}_{x+\hat{2}} \cdot \vec{S}_{x+\hat{1}+\hat{2}} - \frac{1}{4}), \\
H_9 &= -Q \sum_{x\in(2m,2n)} (\vec{S}_x \cdot \vec{S}_{x+\hat{2}} - \frac{1}{4})(\vec{S}_{x+\hat{1}} \cdot \vec{S}_{x+\hat{1}+\hat{2}} - \frac{1}{4}),
\end{aligned}$$

$$\begin{aligned}
H_{10} &= -Q \sum_{x\in(2m+1,2n)} (\vec{S}_x \cdot \vec{S}_{x+\hat{2}} - \frac{1}{4})(\vec{S}_{x+\hat{1}} \cdot \vec{S}_{x+\hat{1}+\hat{2}} - \frac{1}{4}), \\
H_{11} &= -Q \sum_{x\in(2m,2n+1)} (\vec{S}_x \cdot \vec{S}_{x+\hat{2}} - \frac{1}{4})(\vec{S}_{x+\hat{1}} \cdot \vec{S}_{x+\hat{1}+\hat{2}} - \frac{1}{4}), \\
H_{12} &= -Q \sum_{x\in(2m+1,2n+1)} (\vec{S}_x \cdot \vec{S}_{x+\hat{2}} - \frac{1}{4})(\vec{S}_{x+\hat{1}} \cdot \vec{S}_{x+\hat{1}+\hat{2}} - \frac{1}{4}),
\end{aligned} \tag{A.1}$$

where the interactions J and Q are treated separately. Suzuki-Trotter decompositions can explicitly break lattice symmetries, i.e. reflection and 90 degrees rotation. They are restored in the continuous time limit, but by choosing an appropriate ordering of the Suzuki-Trotter decomposition time slices, even in discrete time the lattice symmetries remain intact when combined with a discrete time translation. A good choice is the order $H1$, H_5, H_9, H_2, H_{10}, H_6, H_3, H_8, H_{12}, H_4, H_{11}, H_7.

The cluster rules for $H_1, \ldots, H_4$ are the usual antiferromagnetic ones as shown in chapter 2. For the $H_5, \ldots, H_{12}$ contributions, bonds have to be set on two plaquettes simultaneously. Non-trivial bonds can only be chosen when the spins are antiparallel on both plaquettes. If that is the case and both spins stay constant in time on both plaquettes bond A or B is chosen on both plaquettes, with the probabilities

$$p_A = \frac{1}{1 + \frac{1}{2}\exp\left(\frac{\varepsilon Q}{2}\right)\sinh\left(\frac{\varepsilon Q}{2}\right)}, \qquad p_B = 1 - p_A. \tag{A.2}$$

The cluster update is the same as in the usual Heisenberg model. Clusters are collectively flipped, i.e. the orientation of the spins is inverted .

A.2 4-Step Suzuki-Trotter Decomposition

In order to save CPU time and memory space one can easily treat four spins at once and one then just needs four time-steps

$$\begin{aligned}
H_1 &= \sum_{x\in(2m,2n)} h_x, \; H_2 = \sum_{x\in(2m+1,2n)} h_x, \\
H_3 &= \sum_{x\in(2m,2n+1)} h_x, \; H_4 = \sum_{x\in(2m+1,2n+1)} h_x,
\end{aligned} \tag{A.3}$$

with

$$\begin{aligned}
h_x = J\sum_i \vec{S}_x \cdot \vec{S}_{x+\hat{i}} \quad &-Q\Big[(\vec{S}_x \cdot \vec{S}_{x+\hat{1}} - \frac{1}{4})(\vec{S}_{x+\hat{2}} \cdot \vec{S}_{x+\hat{1}+\hat{2}} - \frac{1}{4}) \\
&+(\vec{S}_x \cdot \vec{S}_{x+\hat{2}} - \frac{1}{4})(\vec{S}_{x+\hat{1}} \cdot \vec{S}_{x+\hat{1}+\hat{2}} - \frac{1}{4})\Big].
\end{aligned} \tag{A.4}$$

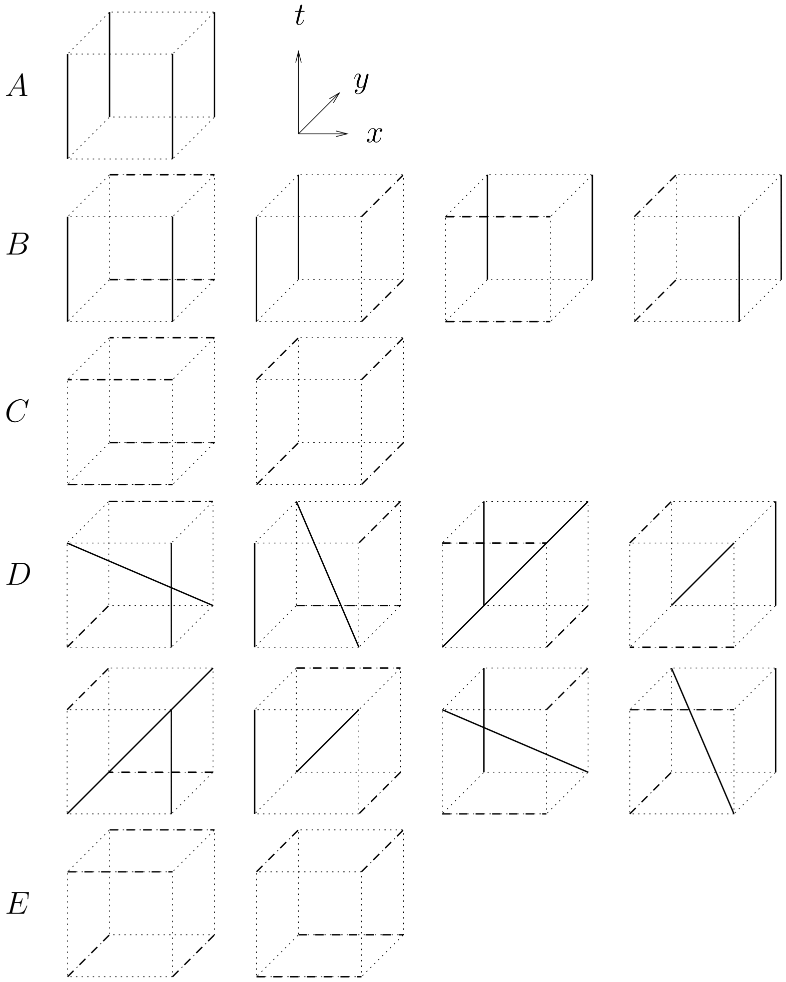

Figure A.1: *Break-ups for the JQ-Model in discrete time using a four-step Suzuki-Trotter decomposition. Straight lines are constraints that bind parallel spins whereas dashed lines bind antiparallel spins.*

One now obtains a 16×16 transfer-matrix which can be decomposed into the break-ups shown in figure A.1. These break-ups have Boltzmann weights

$$\begin{aligned}
A &= \exp\left(-\frac{\varepsilon J}{2}\right), \\
B &= \frac{1}{2}\left(1-\exp\left(-\frac{\varepsilon J}{2}\right)\right), \\
C &= \frac{1}{6}\exp\left(-\frac{\varepsilon J}{2}\right)+\frac{1}{4}\exp\left(\frac{\varepsilon Q}{2}\right)+\frac{1}{12}\exp\left(\frac{3\varepsilon Q}{2}+\varepsilon J\right)-\frac{1}{2}, \\
D &= \frac{1}{4}\left(\cosh\left(\frac{\varepsilon J}{2}\right)-1\right), \\
E &= -\frac{1}{12}\exp\left(-\frac{\varepsilon J}{2}\right)-\frac{1}{4}\exp\left(\frac{\varepsilon Q}{2}\right)+\frac{1}{12}\exp\left(\frac{3\varepsilon Q}{2}+\varepsilon J\right)+\frac{1}{2}.
\end{aligned} \tag{A.5}$$

Updating the configuration works as usual, i.e. on a given cube-configuration all possible break-ups that fit are chosen according to their Boltzmann weight. In a second step the usual loop-cluster updates are performed.

Appendix B

Antiferromagnet on a Triangular Lattice in the Classical Ground State Basis

Here we present a calculation we have done for an antiferromagnet on a triangular lattice. We will present it in the framework of SSE. Usually $SU(2)$ spins are quantised along the z-axis. Choosing different quantisation axes, i.e. setting the system up in a different basis, does not change the physics. There are many reasons to do that. In particular, the efficiency of an algorithm may depend on the chosen basis. For example, there could even be a sign problem in one basis, whereas in another basis there is none.

as discussed in chapter 7, in the case of a triangular lattice we expect coplanar order. It thus seems natural to quantise the spins on the three sublattices A, B, C separately along the expected coplanar directions. The system then has a reference configuration which guarantees an efficient cluster update, because from every configuration we can get to the reference configuration within one multi-cluster update with non-zero probability. Also the clusters can only grow within areas of coplanar order. Thus the clusters cannot grow too large.

B.1 Quantisation in a Coplanar Basis

Let us consider the Hamiltonian on a single bond with spins quantised along the z-axis, i.e. in the basis $\{|\uparrow\uparrow\rangle, |\uparrow\downarrow\rangle, |\downarrow\uparrow\rangle, \downarrow\downarrow\rangle\}$, including the energy-shift of $-\frac{J}{4}$ that is usual in the SSE representation of a spin $\frac{1}{2}$ Heisenberg antiferromagnet

$$H = \frac{J}{2} \begin{pmatrix} 0 & 0 & 0 & 0 \\ 0 & -1 & 1 & 0 \\ 0 & 1 & -1 & 0 \\ 0 & 0 & 0 & 0 \end{pmatrix}. \tag{B.1}$$

We now want to quantise the spins on the sublattice A along the z-axis and rotate the quantisation axis of the spins on sublattice B around the y-axis by 120 degrees and the quantisation axis on sublattice C by 240 degrees, following the coplanar order.

When we consider a single bond, connecting the A and B sublattice, we have to rotate the second spin (the rotation of the other sublattice works in the same way). We can do this with a unitary transformation

$$\begin{aligned} U &= \exp(\frac{2\pi i}{3} S_B^2) = \exp(\frac{\pi i}{3} \sigma_B^2) = \cos\frac{\pi}{3}\mathbb{1} + i \sin\frac{\pi}{3}\sigma_B^2 \\ &= \frac{1}{2}\begin{pmatrix} 1 & \sqrt{3} & 0 & 0 \\ -\sqrt{3} & 1 & 0 & 0 \\ 0 & 0 & 1 & \sqrt{3} \\ 0 & 0 & -\sqrt{3} & 1 \end{pmatrix}. \end{aligned} \tag{B.2}$$

The rotated Hamilton operator then takes the form

$$H' = \frac{J}{8}\begin{pmatrix} -3 & -\sqrt{3} & \sqrt{3} & -3 \\ -\sqrt{3} & -1 & 1 & -\sqrt{3} \\ \sqrt{3} & 1 & -1 & \sqrt{3} \\ -3 & -\sqrt{3} & \sqrt{3} & -3 \end{pmatrix}. \tag{B.3}$$

The system with this Hamiltonian can be simulated using four non-unit-matrix operators shown in figure B.1 with the weights $B_0 = \frac{J}{4}(2-\sqrt{3})$, $B_1 = B_2 = \frac{J}{8}(\sqrt{3}-1)$, $D = \frac{J}{8}$. This algorithm should run efficiently, because it has a reference configuration in which all spins are parallel. All clusters can be flipped into the reference configuration within one single multi-cluster update. However, there are off-diagonal non-negative elements that give rise to a sign problem.

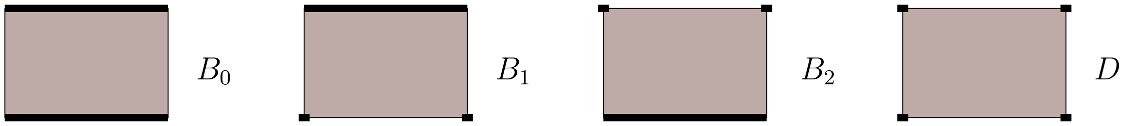

Figure B.1: *Break-ups of the antiferromagnet in the coplanar basis. Thick lines are constraints, that bind parallel spins.*

B.2 How to Deal with the Sign Problem

We can associate an orientation to all bonds on the lattice. We define the forward-orientation going from A to B to C and backwards as A to C to B. This is shown in figure B.2.

The negative signs in the path integral arise, when there is a down-spin next to an up-spin in the forward direction. This means that the signs do not factorise to the clusters.

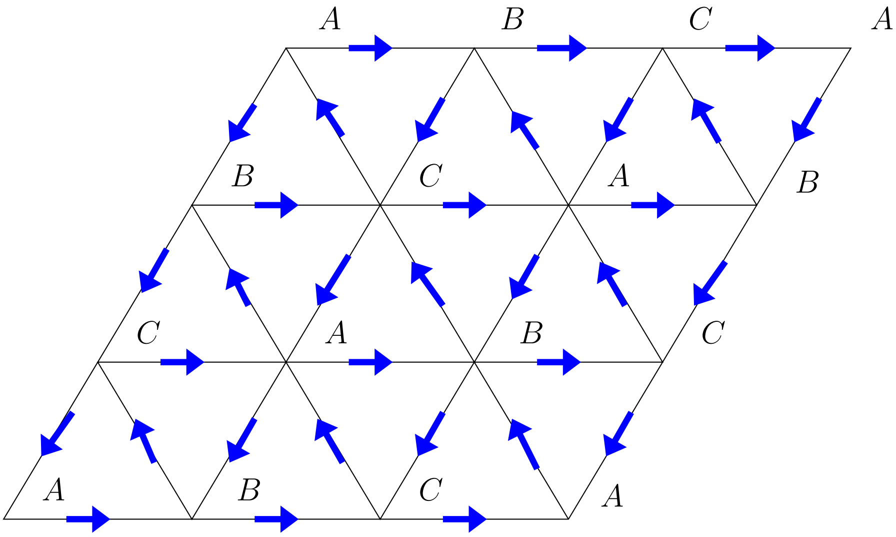

Figure B.2: *Positive orientation of the bonds on the triangular lattice going from A to B to C.*

It is natural to connect the clusters in these positions where the negative signs arise. In figure B.3 this reconnection is denoted by dotted lines. Now we integrate out all possible partitions and orientations of such closed loops. Each straight line contributes a factor of

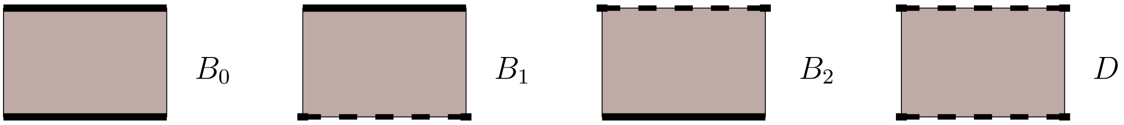

Figure B.3: *Reconnecting the partial clusters denoted by dotted lines.*

$\sqrt{\frac{J}{8}}(\sqrt{3}-1)$ and each dotted line contributes a factor $\sqrt{\frac{J}{8}}$. Each closed loop now contains n_1 dotted bonds in the forward direction and n_2 dotted bonds in the backwards direction. The resulting sign from integrating out all orientations of the clusters contained in a loop, that arises from connecting the open clusters, is

$$\operatorname{sign}(n_1, n_2) = \operatorname{Tr}[(1 + i\sigma_2)^{n_1}(1 - i\sigma_2)^{n_2}]. \tag{B.4}$$

To evaluate this expression we use

$$\begin{aligned} 1 - i\sigma_2 &= \frac{1}{2}\begin{pmatrix} 1 & -i \\ -i & 1 \end{pmatrix}\begin{pmatrix} 1+i & 0 \\ 0 & 1-i \end{pmatrix}\begin{pmatrix} 1 & i \\ i & 1 \end{pmatrix}, \\ 1 + i\sigma_2 &= \frac{1}{2}\begin{pmatrix} 1 & -i \\ -i & 1 \end{pmatrix}\begin{pmatrix} 1-i & 0 \\ 0 & 1+i \end{pmatrix}\begin{pmatrix} 1 & i \\ i & 1 \end{pmatrix}. \end{aligned} \tag{B.5}$$

We then obtain

$$\begin{aligned}
\mathrm{sign}(n_1,n_2) &= \mathrm{Tr}\left[\begin{pmatrix} 1-i & 0 \\ 0 & 1+i \end{pmatrix}^{n_1}\begin{pmatrix} 1+i & 0 \\ 0 & 1-i \end{pmatrix}^{n_2}\right] \\
&= (1-i)^{n_1}(1+i)^{n_2} + (1+i)^{n_1}(1-i)^{n_2} \\
&= 2\sqrt{2}^{n_1+n_2}\cos\left[\frac{\pi}{4}(n_1-n_2)\right]. \qquad \text{(B.6)}
\end{aligned}$$

Next we sum over all possible distributions of connected and disconnected cluster bonds that form closed loops with N_1 forward and N_2 backward oriented bonds. The weight of such a loop is

$$\begin{aligned}
&\sum_{n_1=0}^{N_1}\sum_{n_2=0}^{N_2}\sqrt{\frac{J}{8}}^{N_1+N_2}\left[\sqrt{3}-1\right]^{N_1+N_2-n_1-n_2}\begin{pmatrix} N_1 \\ n_1 \end{pmatrix}\begin{pmatrix} N_2 \\ n_2 \end{pmatrix}\mathrm{sign}(n_1,n_2) \\
= &\sqrt{\frac{J}{2}}^{N_1+N_2} 2\cos\left[\frac{\pi}{6}(N_1-N_2)\right]. \qquad \text{(B.7)}
\end{aligned}$$

Now each operator-bond carries a factor of $\sqrt{\frac{J}{2}}$, i.e. each operator has a weight of $\frac{J}{2}$ as it was the case in the original basis. Each loop carries a factor of 2 which is also the case when integrating out the spins in the original basis. The cosine factor is the sign of the loop. It can be easily seen, that $|N_1 - N_2|$ is always a multiple of six and thus the sign-factor is indeed ± 1.

B.3 Cluster Algorithm with the Spins Integrating out

The new cluster rules are exactly identical to those shown in chapter 8. This is not very surprising, because by integrating out spins, the information of the quantisation axis is lost and thus the result should be independent of the chosen basis. Thus the choice of a new basis did not lead to an improvement in this case. We are thus back to the nested algorithm where we can improve the error of the average sign, but where we cannot completely solve the sign problem.

One of the things we learned from this exercise is that a reference configuration is not enough to solve a sign-problem. In addition to the reference configuration the sign would have to factorise to the clusters. The spin-spin correlation is of the order of the cluster size in the coplanar basis. After integrating out the spins the clusters have become bigger. Thus we think that there is some correlation bigger than the spin-spin correlation which is probably a measure of quantum entanglement.

Bibliography

[1] J. C. Bednorz and K. A. Müller. *Z. Phys.*, B64:189, 1986.

[2] P. Dai, B. C. Chakoumakos, G. F. Sun, K. W. Wong, Y. Xin, and D. F. Lu. *Physica C*, 243(3-4):201 – 206, 1995.

[3] J. Bardeen, L. N. Cooper, and J. R. Schrieffer. *Phys. Rev.*, 106:162, 1957.

[4] O. I. Motrunich and P. A. Lee. *Phys. Rev. B*, 69(21):214516, Jun 2004.

[5] W. Zheng, J. Oitmaa, C J. Hamer, and R. R. P. Singh. *Phys. Rev. B*, 70(2):020504, Jul 2004.

[6] H. Watanabe and M. Ogata. *J. Phys. Soc. Jpn.*, 74(11):2901–2904, 2005.

[7] F.-J. Jiang, F. Kämpfer, M. Nyfeler, and U.-J. Wiese. *Phys. Rev. B*, 78(21):214406, 2008.

[8] F.-J. Jiang, F. Kämpfer, and M. Nyfeler. *Phys. Rev. B*, 80(3):033104, 2009.

[9] F.-J. Jiang, M. Nyfeler, S. Chandrasekharan, and U.-J. Wiese. *J. Stat. Mech.*, 2008(02):P02009 (19pp), 2008.

[10] S. Weinberg. *Physica A*, 96(1-2):327 – 340, 1979.

[11] J. Gasser and H. Leutwyler. *Nucl. Phys. B*, 250(1-4):539 – 560, 1985.

[12] J. Gasser, M. E. Sainio, and A. Svarc. *Nuclear Physics B*, 307(4):779 – 853, 1988.

[13] E. Jenkins and A. V. Manohar. *Physics Letters B*, 255(4):558 – 562, 1991.

[14] V. Bernard, N. Kaiser, J. Kambor, and U.-G. Meissner. *Nuclear Physics B*, 388(2):315 – 345, 1992.

[15] T. Becher and H. Leutwyler. *Eur. Phys. J.*, C(9):643, 1999.

[16] S. Chakravarty, B. I. Halperin, and D. R. Nelson. *Phys. Rev. B*, 39(4):2344–2371, Feb 1989.

[17] H. Neuberger and T. Ziman. *Phys. Rev. B*, 39(4):2608–2618, Feb 1989.

[18] D. S. Fisher. *Phys. Rev. B*, 39(16):11783–11792, Jun 1989.

[19] P. Hasenfratz and H. Leutwyler. *Nucl. Phys.*, B343:241–284, 1990.

[20] P. Hasenfratz and F. Niedermayer. *Phys. Lett.*, B268:231, 1991.

[21] P. Hasenfratz and F. Niedermayer. *Z. Phys.*, B92:91, 1993.

[22] A. V. Chubukov, T. Senthil, and S. Sachdev. *Phys. Rev. Lett.*, 72(13):2089–2092, Mar 1994.

[23] H. Leutwyler. *Phys. Rev. D*, 49(6):3033–3043, Mar 1994.

[24] C. Brügger, F. Kämpfer, M. Moser, M. Pepe, and U.-J. Wiese. *Phys. Rev.*, B74:224432, 2006.

[25] F. Kämpfer, M. Moser, and U.-J. Wiese. *Nucl. Phys.*, B729:317–360, 2005.

[26] C. Brügger, C. P. Hofmann, F. Kämpfer, M. Moser, M. Pepe, and U.-J. Wiese. *Phys. Rev. B*, 75(21):214405, 2007.

[27] M. Troyer and U.-J. Wiese. *Phys. Rev. Lett.*, 94:170201, 2005.

[28] C. Gottbrath, J. Bailin, C. Meakin, T. Thompson, and J. J. Charfman. arXiv:9912202, 1999.

[29] N. Metropolis, A. W. Rosenbluth, M. N. Rosenbluth, A. H. Teller, and E. Teller. *J. Chem. Phys.*, 21:1087–1092, 1953.

[30] R. H. Swendsen and J.-S. Wang. *Phys. Rev. Lett.*, 58:86–88, 1987.

[31] U. Wolff. *Phys. Rev. Lett.*, 62:361, 1989.

[32] H.-P. Ying and F. Chen. *Phys. Lett. A*, 208(4-6):356 – 360, 1995.

[33] H. G. Evertz, G. Lana, and M. Marcu. *Phys. Rev. Lett.*, 70(7):875–879, Feb 1993.

[34] U. J. Wiese and H. P. Ying. *Z. Phys. B.*, B93:147–150, 1994.

[35] A. W. Sandvik. *Phys. Rev. Lett.*, 98(22):227202, 2007.

[36] M. Levin and T. Senthil. *Phys. Rev. B*, 70(22):220403, Dec 2004.

[37] K. Yang, K. L. Warman, and S. M. Girvin. *Phys. Rev. Lett.*, 70:2641, 1993.

[38] S. H. Lee, H. Kikuchi, Y. Qiu, B. Lake, Q. Huang, K. Habicht, and K. Kiefer. *Nat. Mater.*, 6(11):853–857, Nov 2007.

[39] W. Bietenholz, A. Pochinsky, and U.-J. Wiese. *Phys. Rev. Lett.*, 75:4524–4527, 1995.

[40] M. Nyfeler, F.-J. Jiang, F. Kämpfer, and U.-J. Wiese. *Phys. Rev. Lett.*, 100:247206, 2008.

[41] N. D. Mermin and H. Wagner. *Phys. Rev. Lett.*, 17(22):1133–1136, Nov 1966.

[42] M. Troyer and P. Werner. In *LECTURES ON THE PHYSICS OF STRONGLY CORRELATED SYSTEMS XIII: Thirteenth Training Course in the Physics of Strongly Correlated Systems*, volume 1162, pages 98–173. AIP, 2009.

[43] H. G. Evertz. *Advances in Physics*, 52:1, 2003.

[44] M. Suzuki. *Physica A*, 194(1-4):432 – 449, 1993.

[45] H. G. Evertz and W. von der Linden. *Phys. Rev. Lett.*, 86(22):5164–5167, May 2001.

[46] A. W. Sandvik and H. G. Evertz. arXiv:0807.0682, 2008.

[47] U.-J. Wiese and H.-P. Ying. *Phys. Lett. A*, 168(2):143 – 150, 1992.

[48] B. B. Beard and U.-J. Wiese. *Phys. Rev. Lett.*, 77:5130–5133, 1996.

[49] N. V. Prokof'ev, B. V. Svistunov, and I. S. Tupitsyn. *JETP*, 87:310–321, 1998.

[50] A. W. Sandvik. *Phys. Rev.*, B59:14157, 1999.

[51] A. W. Sandvik, R. R. P. Singh, and D. K. Campbell. *Phys. Rev. B*, 56(22):14510–14528, Dec 1997.

[52] B. B. Beard, R. J. Birgeneau, M. Greven, and U.-J. Wiese. *Phys. Rev. Lett.*, 80(8):1742–1745, Feb 1998.

[53] U. Gerber, C. P. Hofmann, F.-J. Jiang, M. Nyfeler, and U.-J. Wiese. *J. Stat. Mech.*, 2009(03):P03021 (19pp), 2009.

[54] A. Mattsson, P. Fröjdh, and T. Einarsson. *Phys. Rev. B*, 49(6):3997–4002, Feb 1994.

[55] C. J. Hamer, Z. Weihong, and J. Oitmaa. *Phys. Rev. B*, 50(10):6877–6888, Sep 1994.

[56] J. Oitmaa, C. J. Hamer, and Zheng Weihong. *Phys. Rev. B*, 45(17):9834–9841, May 1992.

[57] Eduardo V. Castro, N. M. R. Peres, K. S. D. Beach, and A. W. Sandvik. *Physical Review B*, 73:054422, 2006.

[58] A. Parola, S. Sorella, and Q. F. Zhong. *Phys. Rev. Lett.*, 71(26):4393–4396, Dec 1993.

[59] I. Affleck and B. I. Halperin. *J. Phys.*, A29:2627–2632, 1996.

[60] A. W. Sandvik. *Phys. Rev. Lett.*, 83(15):3069–3072, Oct 1999.

[61] V. Yu. Irkhin and A. A. Katanin. *Phys. Rev. B*, 61(10):6757–6764, Mar 2000.

[62] Y. J. Kim and R. J. Birgeneau. *Phys. Rev. B*, 62(10):6378–6384, Sep 2000.

[63] T. Pardini, R. R. P. Singh, A. Katanin, and O. P. Sushkov. *Phys. Rev. B*, 78(2):024439, 2008.

[64] S. Eggert, I. Affleck, and M. Takahashi. *Phys. Rev. Lett.*, 73(2):332–335, Jul 1994.

[65] M. Azzouz. *Phys. Rev. B*, 48(9):6136–6140, Sep 1993.

[66] I. Affeck, M. P. Gelfand, and R. R. P. Singh. *J. Phys. A*, 27(22):7313–7325, 1994.

[67] T. Miyazaki, D. Yoshioka, and M. Ogata. *Phys. Rev. B*, 51(5):2966–2971, Feb 1995.

[68] M. Campostrini, M. Hasenbusch, A. Pelissetto, P. Rossi, and E. Vicari. *Physical Review B*, 65:144520, 2002.

[69] A. F. Albuquerque, F. Alet, P. Corboz, P. Dayal, A. Feiguin, S. Fuchs, L. Gamper, E. Gull, S. Guertler, A. Honecker, R. Igarashi, M. Koerner, A. Kozhevnikov, A. Laeuchli, S. R. Manmana, M. Matsumoto, I. P. McCulloch, F. Michel, R. M. Noack, G. Pawlowski, L. Pollet, T. Pruschke, U. Schollwock, S. Todo, S. Trebst, M. Troyer, P. Werner, and S. Wessel. *Journal of Magnetism and Magnetic Materials*, 310:1187, 2007.

[70] A. B. Kuklov, M. Matsumoto, N. V. Prokof'ev, B. V. Svistunov, and M. Troyer. *Phys. Rev. Lett.*, 101(5):050405, 2008.

[71] R. G. Melko, A. W. Sandvik, and D. J. Scalapino. *Phys. Rev. B*, 69(10):100408, Mar 2004.

[72] A. Kuklov, N. Prokof'ev, and B. Svistunov. *Phys. Rev. Lett.*, 93(23):230402, Nov 2004.

[73] Anatoly Kuklov, Nikolay Prokof'ev, Boris Svistunov, and Matthias Troyer. *Annals of Phys.*, 321:1602, 2006.

[74] Olexei I. Motrunich and Ashvin Vishwanath. arXiv:0805.1494, 2008.

[75] A. Kuklov, M. Matsumoto, N. Prokof'ev, B. Svistunov, and M. Troyer. arXiv:0805.2578, 2008.

[76] J. Lou, A. W. Sandvik, and N. Kawashima. arXiv:0908.0740, 2009.

[77] R. G. Melko and R. K. Kaul. *Phys. Rev. Lett.*, 100:017203, 2008.

[78] A. M. Ferrenberg and R. H. Swendsen. *Phys. Rev. Lett.*, 61(23):2635–2638, Dec 1988.

[79] B. Bernu, C. Lhuillier, and L. Pierre. *Phys. Rev. Lett.*, 69(17):2590–2593, Oct 1992.

[80] S. Chandrasekharan and U.-J. Wiese. *Phys. Rev. Lett.*, 83:3116, 1999.

[81] `http://www.claymath.org/millennium/`.

[82] S. Chandrasekharan, J. Cox, J. C. Osborn, and U.-J. Wiese. *Nucl. Phys.*, B673:405–436, 2003.

[83] S. Chandrasekharan, J. Cox, K. Holland, and U.-J. Wiese. *Nucl. Phys.*, B576:481–500, 2000.

[84] M. Boninsegni, N. V. Prokof'ev, and B. V. Svistunov. *Physical Review E*, 74:036701, 2006.

[85] N. Prokof'ev and B. Svistunov. *Phys. Rev. Lett.*, 87:160601, 2001.

[86] Olav F. Syljuåsen and Anders W. Sandvik. *Phys. Rev. E*, 66(4):046701, Oct 2002.

[87] M. Lüscher and P. Weisz. *JHEP*, 09:010, 2001.

[88] J. Yoo, S. Chandrasekharan, and H. U. Baranger. *Phys. Rev. E*, 71:036708, 2005.

[89] B. O. Wells, Z. X. Shen, A. Matsuura, D. M. King, M. A. Kastner, M. Greven, and R. J. Birgeneau. *Phys. Rev. Lett.*, 74(6):964–967, Feb 1995.

[90] S. LaRosa, I. Vobornik, F. Zwick, H. Berger, M. Grioni, G. Margaritondo, R. J. Kelley, M. Onellion, and A. Chubukov. *Phys. Rev. B*, 56(2):R525–R528, Jul 1997.

[91] C. Kim, P. J. White, Z.-X. Shen, T. Tohyama, Y. Shibata, S. Maekawa, B. O. Wells, Y. J. Kim, R. J. Birgeneau, and M. A. Kastner. *Phys. Rev. Lett.*, 80(19):4245–4248, May 1998.

[92] F. Ronning, C. Kim, D. L. Feng, D. S. Marshall, A. G. Loeser, L. L. Miller, J. N. Eckstein, I. Bozovic, and Z.-X. Shen. *Science*, 282:2067–+, December 1998.

[93] S. A. Trugman. *Phys. Rev. B*, 37(4):1597–1603, Feb 1988.

[94] B. I. Shraiman and E. D. Siggia. *Phys. Rev. Lett.*, 60(8):740–743, Feb 1988.

[95] B. I. Shraiman and E. D. Siggia. *Phys. Rev. Lett.*, 61(4):467–470, Jul 1988.

[96] B. I. Shraiman and E. D. Siggia. *Phys. Rev. Lett.*, 62(13):1564–1567, Mar 1989.

[97] B. I. Shraiman and E. D. Siggia. *Phys. Rev. B*, 46(13):8305–8311, Oct 1992.

[98] V. Elser, D. A. Huse, B. I. Shraiman, and E. D. Siggia. *Phys. Rev. B*, 41(10):6715–6723, Apr 1990.

[99] M. Brunner, F. F. Assaad, and A. Muramatsu. *Phys. Rev. B*, 62(23):15480–15492, Dec 2000.

[100] A. S. Mishchenko, N. V. Prokof'ev, and B. V. Svistunov. *Phys. Rev. B*, 64(3):033101, Jun 2001.

[101] C. Honerkamp and P. A. Lee. *Phys. Rev. Lett.*, 90(24):246402, Jun 2003.

[102] H. Kusunose and T. M. Rice. *Phys. Rev. Lett.*, 91(18):186407, Oct 2003.

[103] D. Sénéchal and A.-M. S. Tremblay. *Phys. Rev. Lett.*, 92(12):126401, Mar 2004.

[104] Q. Yuan, Y. Chen, T. K. Lee, and C. S. Ting. *Phys. Rev. B*, 69(21):214523, Jun 2004.

[105] T. Tohyama. *Phys. Rev. B*, 70(17):174517, Nov 2004.

[106] L. Cheng, H. Guo, and S. Feng. *Phys. Lett. A*, 366(1-2):137 – 144, 2007.

[107] M. Aichhorn, E. Arrigoni, M. Potthoff, and W. Hanke. *Phys. Rev. B*, 74(23):235117, 2006.

[108] C. Bolliger. *Diploma Thesis Bern*, 2007.

[109] C. Brügger, C. P. Hofmann, F. Kämpfer, M. Pepe, and U. J. Wiese. *Physical Review B*, 75:014421, 2007.

[110] F.-J. Jiang, F. Kämpfer, C. P. Hofmann, and U.-J. Wiese. *Europ. Phys. J. B*, 69(4):473–482, 2009.

[111] A. Lüscher, A. Läuchli, W. Zheng, and O. P. Sushkov. *Phys. Rev. B*, 73(15):155118, 2006.

Erklärung

gemäss Art. 28 Abs. 2 RSL 05

Name/Vorname:	Nyfeler Matthias
Matrikelnummer:	01-139-468
Studiengang:	Physik
	Bachelor ☐ Master ☐ Dissertation ☒
Titel der Arbeit:	Numerical Simulations of Strongly Correlated Electron Systems on Bipartite and on Frustrated Lattices
Leiter der Arbeit:	Prof. Dr. Uwe-Jens Wiese

Ich erkläre hiermit, dass ich diese Arbeit selbständig verfasst und keine anderen als die angegebenen Quellen benutzt habe. Alle Stellen, die wörtlich oder sinngemäss aus Quellen entnommen wurden, habe ich als solche gekennzeichnet. Mir ist bekannt, dass andernfalls der Senat gemäss Artikel 36 Absatz 1 Buchstabe o des Gesetzes vom 5. September 1996 über die Universität zum Entzug des auf Grund dieser Arbeit verliehenen Titels berechtigt ist.

Bern, den 6. Oktover 2009

CURRICULUM VITÆ

Personal Data

Name	**Nyfeler, Matthias**
Date of birth	July 17, 1980
Nationality	Swiss
Present address	Institute for theoretical Physics University of Bern Sidlerstrasse 5 3012 Bern, Switzerland tel: +41 31 631 86 82 email: `nyfeler@itp.unibe.ch`

Education

1987 - 1990	Schools in Aarwangen
1990 - 1995	Schools in Wolfwil
1995 - 2000	Kantonsschule Olten
2001 - 2006	University of Bern Studies in physics, mathematics, and computer science
January 2006	University of Bern Master of Science in Physics: *A new Cluster Algorithm for the Ising Model* supervised by Prof. Dr. U.-J. Wiese
2006 - 2009	University of Bern PhD student of Prof. Dr. U.-J. Wiese

Attended Training Courses

August 2008	MP2 Summer School 2008 on Algebraic and Computational Methods for Strongly Correlated Systems
October 2008	XIII Training Course in the Physics of Strongly Correlated Systems, Vietri sul Mare, Italy *Talk contributed*

July 2009	Boulder School for Condensed Matter and Materials Physics: Nonequilibrium Statistical Mechanics: Fundamental Problems and Applications, Boulder, Colorado, United States of America *Poster contributed*

Attended Conferences and Workshops

July 2005	Lattice 2005: XXIII International Symposium on Lattice Field Theory, Dublin, Ireland *Talk contributed*
November 2008	Workshop on Monte Carlo data evaluation, archiving and provenance, ETH Zürich, Switzerland
June 2009	Workshop on Open Systems: Non-Equilibrium Phenomena - Dissipation, Decoherence, Transport, ETH Zürich, Switzerland

Other

May/June 2008	Invited scientific visit with Professor Christoph Hofmann at the University of Colima, Colima, Mexico *Invited seminar talk held* *Two student seminar talks held*

Publications

Nested Cluster Algorithm for Frustrated Quantum Antiferromagnets, M. Nyfeler, F.-J. Jiang, F. Kampfer, U.-J. Wiese, Phys. Rev. Lett. 100, 247206 (2008)

Constraint Effective Potential of the Staggered Magnetization in an Antiferromagnet, U. Gerber, C. P. Hofmann, F.-J. Jiang, M. Nyfeler, U.-J. Wiese, J. Stat. Mech. (2009) P03021

Loop-Cluster Simulation of the t-J Model on the Honeycomb Lattice, F.-J. Jiang, F. Kämpfer, M. Nyfeler, U.-J. Wiese, Phys. Rev. B 78, 214406 (2008)

From an Antiferromagnet to a Valence Bond Solid: Evidence for a First Order Phase Transition, F.-J. Jiang, M. Nyfeler, S. Chandrasekharan, U.-J. Wiese, J. Stat. Mech. (2008) P02009

Monte Carlo Determination of the Low-Energy Constants of a Spin 1/2 Heisenberg Model with Spatial Anisotropy, F. J. Jiang, F. Kämpfer, Phys. Rev. B 80, 033104 (2009)

A new efficient cluster algorithm for the Ising model, M. Nyfeler, M. Pepe and U. J. Wiese, PoS **LAT2005** (2006) 112 [arXiv:hep-lat/0510040]

From an Antiferromagnet to a Valence Bond Solid: Evidence for a First Order Phase Transition, M. Nyfeler and F.-J. Jiang and U.-J. Wiese and S. Chandrasekharan, LECTURES ON THE PHYSICS OF STRONGLY CORRELATED SYSTEMS XIII: Thirteenth Training Course in the Physics of Strongly Correlated Systems, 1162, 202-209 (2009)

Languages

German	Mother-tongue
English	Fluent in both spoken and written language
French	Intermediate in both spoken and written language
Spanish	Basics